Fatigue and Wear in Rolling and Sliding Contacts

Janakiraman, Shravan

Publication date:
2014

Document Version
Publisher's PDF, also known as Version of record

Fatigue and Wear in Rolling and Sliding Contacts

PhD Thesis

$$(EIv'')'' = q - \rho A\ddot{v}$$

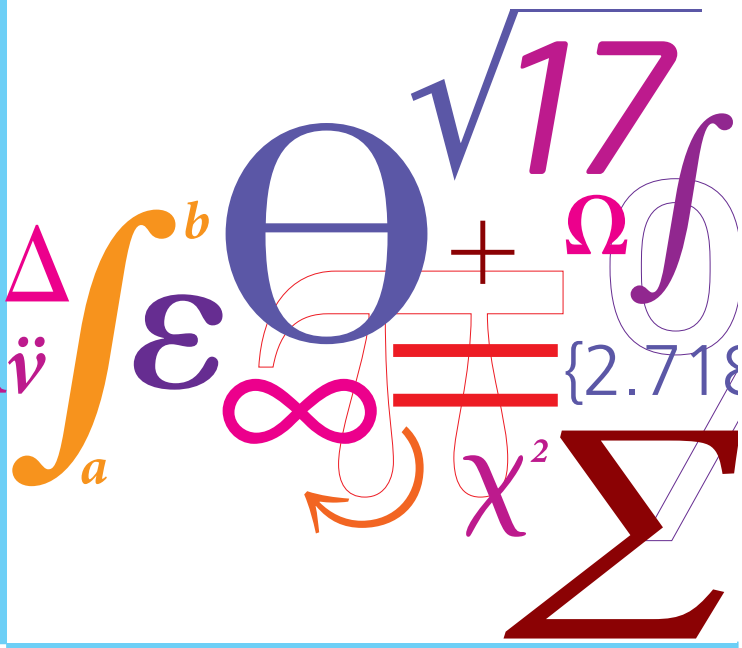

Shravan Janakiraman
DCAMM Special Report No. S181
November 2014

DTU Mechanical Engineering
Department of Mechanical Engineering

Fatigue and Wear in Rolling and Sliding Contacts

Contents

Abstract

The REWIND project was conceptualized to "perform strategic research at the highest level in the field of material-manufacturing-properties-performance of metallic components in the rotor and drive train in large wind turbines, with the ultimate aim of enhancing the reliability and arriving at an improved life expectancy prediction of such components."

One of the focus areas of the REWIND project is to study the failure of the main bearings in a wind turbine and suggest improvements to improve their lifetime.

This PhD project is focused on two areas : Lubrication and rolling contact fatigue.

The main bearing supports the main shaft, which connects the rotor to the gearbox. The main bearing is a rolling element bearing containing spherical rolling elements. The loads on a main bearings are very high, which leads to a lubrication regime called elastohydrodynamic lubrication (EHL). Under the EHL regime, the pressures in the lubricant are large enough to elastically deform contacting surfaces. EHL usually occurs between the inner ring and the rolling element because the non-conformal contact leads to a high interfacial pressure. The EHL film thickness is very small, usually less than 1 micrometer. It is intended to increase the film thickness, so as to ensure there is no contact between the roller and the raceway. Under lower loads (loads less than EHL loads) it has been observed that axial grooves help to increase the film thickness at certain optimum operating conditions. It is believed that these grooves act as reservoirs of lubricant and can emit excess lubricant to increase the film thickness. However the performance of these grooved surfaces have not been studied under EHL loads. So in this Ph.D. project, rolling-sliding, lubricated

tests are performed to study the tribologial behaviour of axially grooved rings under EHL loads. Multigrid models simulating the rolling of a single grooved surface against an infinite half-plane are coded. The results from this model are used to explain certain experimental results.The results show that under EHL loads, the grooves do not appear to prove beneficial in improving the film thickness. They might improve the film thickness at certain optimum running conditions, but it is tough to ascertain what those conditions are.

The main bearings also undergo rolling contact fatigue failure. The main bearings experience premature fatigue failure in both onshore and offshore wind turbines. Their failure is characterized by the formation of nanosized ferrite grains called white etching areas (WEAs). These grains surround the fatigue cracks and turn white when etched with Nital. Hence they are named White Etching Areas. It has also been proven in past studies that under high temperatures and pressures, lubricants can react with a fresh steel surface to decompose and generate hydrogen gas. So it is assumed that hydrogen is generated when the lubricant in a main bearing reacts with the steel surface. This hydrogen then enters the steel surface and causes embrittlement. To study the fatigue failure of these bearings, it was decided to replicate these failures in the lab. So a test rig was built to conduct lubricated RCF tests on 100Cr6 bearing steel rings. The loads applied were similar to those experienced by the main bearing in a wind turbine. Hydrogen is infused into the steel ring by immersing the ring in a solution of aqueous ammonium thiocyanate. The tests are then run until the ring cracks. Once the rings have cracked, they are etched and observed under a microscope. The results show that White Etching Cracks (WECs) can be simulated using the test rig.

The main bearings are usually press-fit onto the main shaft to ensure a tight fit between the inner ring and the shaft. This press-fit introduces a tensile Hoop stress and a compressive radial stress on the inner ring. To simulate this on the test rig, the steel ring specimens are press fit onto the shaft introducing tensile Hoop stresses. The effect of two values of tensile Hoop stress on the fatigue life of the bearing is studied. It is observed that the fatigue life decreases as the tensile Hoop stress is increased.

Preface

This thesis is submitted in partial fulfilment of the requirements for awarding the Danish Ph.D. degree. This work has been carried on from September 2011 to November 2014 at the Technical University of Denmark, Lyngby.

I wish to express my deepest gratitude to Prof. Peder Klit for his continuous guidance and unwavering support throughout the duration of this project. I would also like to express my gratitude to Prof. Viggo Tvergaard for his participation in regular technical discussions regarding modeling and structural mechanics.

I would like to extend a special thanks to my fellow colleagues Niels S. Jensen and Christian Kim Christensen. Niels has been especially instrumental in helping me design and execute the experiments. Christian introduced me to the world of preparing documents using LaTeX. He remains the 'go to' guy for all my LaTeX difficulties .

To my fellow REWIND collaborators, Michele Cerullo and Ole West, Thank You both.

I extend a very special Thank You to my family. I feel a profound sense of gratitude towards them, for helping me get an education. Their sacrifices have been innumerable and immense. I will be forever indebted. And a final Thank You to my mentors who taught me that being educated requires more than obtaining a degree.

Shravan Janakiraman

Chapter 1

Introduction

This study was funded by the REWIND project, a six year center established in January 2011. The center consists of 12 partners and employs 11 Ph.D.s and 5 post docs. The ultimate aim of the project is to "perform strategic research at the highest level in the field of material-manufacturing-properties-performance of metallic components in the rotor and drive train in large wind turbines, with the ultimate aim of enhancing the reliability and arriving at an improved life expectancy prediction of such components." The REWIND research center addresses the entire chain 'material-manufacturing-properties-performance' in a systematic way with emphasis in heavily loaded wind turbine components in order to be able to understand, describe and predict the components' performance during service better than what is possible today, thus paving the road for increased reliability and durability of the entire wind turbine.

A Wind turbine is a device that generates electricity from the wind flow. Wind mills are finding increasing acceptance because of their ability to provide clean, sustainable energy. Wind turbines are installed both onshore and offshore. Offshore sites generally provide a more steady supply of wind compared to onshore sites. Offshore wind turbines are however hampered by service and maintenance issues. It is very expensive to access the bearings on an offshore wind turbine, because special ships with cranes need to be arranged to access the components in the turbine. Hence it is imperative that main bearings last the entire lifetime of the turbine (usually around 20 years). Frequently failing bearings require frequent servicing and replacement. It is often observed that the main bearings last 10-15 % of the intended lifetime of the turbine. This

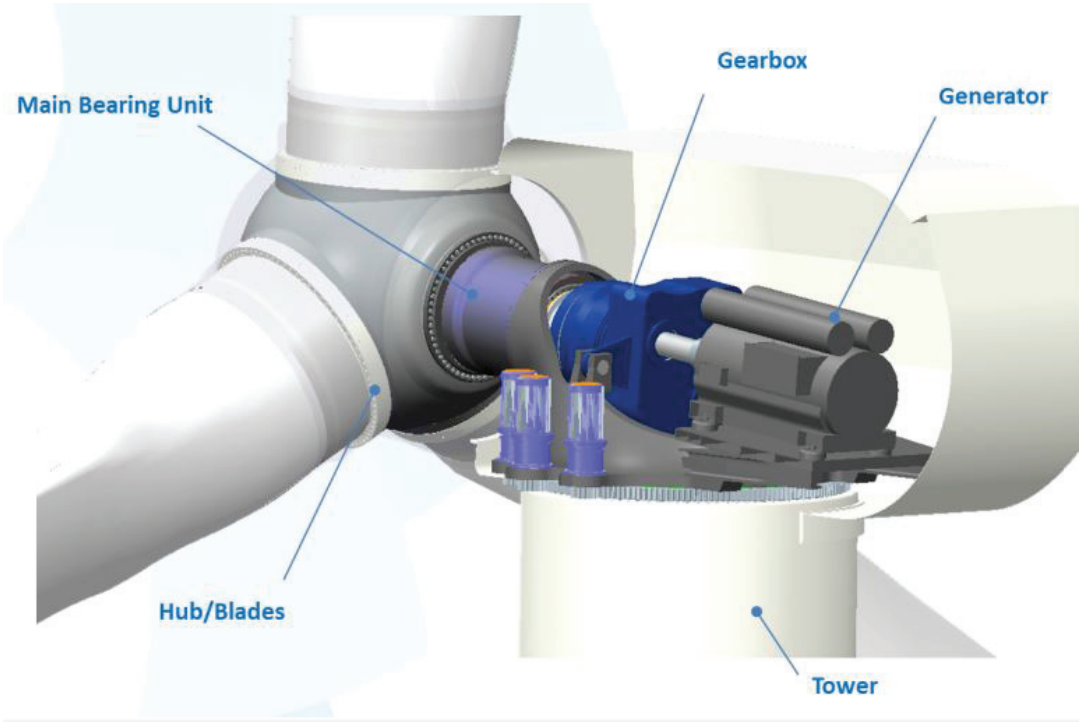

Figure 1.1: The main bearing unit in a wind turbine. Courtesy : EOLOTEC

places a huge financial burden on the turbine manufacturers. The main bearings connects the rotor to the main shaft (Fig. 1.1).

Spherical roller bearings are mainly used as the main shaft bearings. These bearings experience failure via rolling contact fatigue (RCF). These bearings carry the loads exerted by the blades, hub, the main shaft and the wind speed. Larger turbine capacities necessitate the use of bearings that can carry larger loads. Hence the main bearings are continuously increasing in size to be able to handle larger loads. A larger bearing involves material quality problems, machining problems and maintenance problems.

The Siemens 2.3 MW geared wind turbine uses two double row spherical bearings to support the rotor (Fig. 1.2). The Siemens 2.3 MW direct drive (DD) turbine uses a double row tapered bearing to support the rotor [1] (Fig. 1.3).

As the bearing size increases, the probability of material flaws and machin-

Figure 1.2: Double row spherical roller bearings. Courtesy : TIMKEN

ing errors increases as well. The large loads on shaft create conditions for elastohydrodynamic lubrication (EHL) between the raceway and the rolling elements. However, low lubricant film thickness during startup and stopping can create surface damage. When the bearings fail due to RCF, characteristic microstructural damages called White Etching Cracks (WECs) are observed. WECs can be surface or subsurface generated. The mechanisms and drivers for the formation of WECs in wind turbine gearboxes have not been fully understood. It is not yet fully understood as to which operating parameters need to be controlled to prevent the formation of these WECs. After gaining a better understanding of the mechanism of WEC formation, steps can be taken to minimize their formation and improve the lifetime of the main bearings. My module of the REWIND project dealt with studying the failure of the main bearings in a wind turbine.

Figure 1.3: Double row tapered roller bearing

The tasks related to my part of the project were twofold.

1. Study the fatigue failure of these bearings - This task was split into two parts - a modeling part and an experimental part.

For the modeling portion of studying the fatigue failure, I worked in conjunction with Ph.D. student Michele Cerullo, who modeled the fatigue failure of these bearings using a fatigue criterion known as the Dang Van model. I modeled the EHL stresses generated on the surface of the rolling contact using a multigrid, finite difference model. I also modeled the shear stress generated at low loads and slide-roll ratios using a finite difference model. These stresses were forwarded to Mr. Cerullo to be used as an input load in his fatigue model.

In the experimental part, a test rig was constructed to conduct lubricated RCF tests on the test specimens. I worked in conjunction with Ph.D. student Ole West, with a background in materials engineering, in this module. We started out by wanting to simulate the formation of White Etching Cracks (WECs) in failed test specimens. WECs are a characteristic fatigue failure phenomenon observed in the main bearings of a wind turbine. The bearings are usually

mounted on the shaft with a press fit, which leads to generation of a tensile Hoop stress in the bearing inner ring. After we were able to generate WECs in the lab, we then studied the effect of varying Hoop stress (2 different values of Hoop stress) on the fatigue life of the test specimens. While only 100Cr6 bearing steel was tested, it is intended to use other materials in the future to develop better alternatives. It was also studied by Mr. West if a residual compressive stress, developed by processes such as nitriding, could help improve the lifetime of these bearings by counteracting the tensile Hoop stresses.

2. Study the tribology aspects of the bearing contact. This part of the study consisted of a modeling and an experimental task too.

In the modeling portion, the multigrid model developed in the earlier study was extended to study the pressures generated around a single groove. These results were used to explain some experimental results.

In the experimental study, the test rig developed previously was used to measure the interfacial torque in rolling and sliding tests. The aim of this part of the project was to study if grooves on a bearing surface could prove beneficial in retaining lubricant and improve the film thickness under highly loaded conditions. So grooves were engraved on test specimens and lubricated rolling-sliding tests were run to study the interfacial torque between the contacting test surfaces.

At the time of writing this thesis, there are still more than 2 years left for the REWIND project to run it's course. So all aims of the project have not yet been realized. It is intended that the results generated from this study will be used as is or improved upon in the coming years, to help achieve the final goals of the project.

Chapter 2

Test Rig

A test-rig was constructed to conduct tribology tests and rolling contact fatigue (RCF) tests. While the test-rig has been explained in the publications attached to the later chapters, a chapter has been dedicated to it to explain it's use because of it's importance in generating the important experimental results in this thesis.

The test rig consists primarily of two drive shafts and a hydraulic cylinder (Fig. 2.1 and Fig. 2.6). One test ring (Fig. 2.7a) is mounted on each shaft respectively. The permanent module (Fig. 2.2) consists of drive shaft 1 and the hydraulic cylinder. The non-conformal contact module (Fig. 2.3) consists of drive shaft 2 and can be slid along the lathe (Fig. 2.4 and Fig. 2.5). The non-conformal module is allowed to slide along the lathe, so as to accommodate larger test ring diameters. The two ring surfaces are brought into contact against each other by applying a normal load, using the hydraulic cylinder. Each ring has a conical bore, fitted onto a corresponding cone on the shaft (Fig. 2.7b). The contact pressure between the ring and shaft is controlled by the axial positioning of the ring on the shaft. Each drive shaft is capable of rotating at frequencies between 0-50 Hz. There is a provision for relative slip between the two rings when the two shafts rotate at different frequencies respectively. Hence it is possible to create conditions of rolling and sliding. Drive shaft 2 is connected to the master motor and drive shaft 1 is connected to the slave motor.

An inlet resting above the contact between the two rings allows for the lubri-

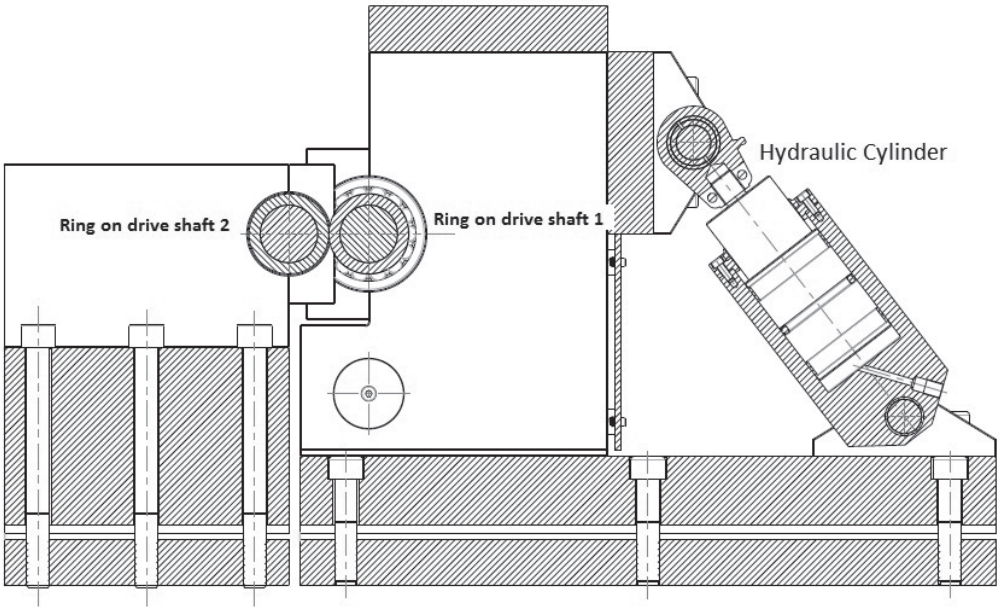

Figure 2.1: Schematic of the Test Rig

cant to flow into the contact. The lubricant used is Mobil Delvac synthetic gear oil 75W-140, which is a fully synthetic, heavy duty drivetrain lubricant. This lubricant has a viscosity 182 cSt at 40°C and 25 cSt at 100°C. The lubrication is not pressurised and the lubricant is allowed to fall freely, from a distance of approximately 2 cm, into the conjunction between the two rings.

A torque transducer is attached to drive shaft 2, so the interfacial torque generated between the two surfaces during slip can be measured. When one of the rings fails, the torque readings fluctuate wildly, setting off an internal alarm and automatically shutting down the test rig.

Each ring has an outer diameter of 70 mm. One ring has a chamfered surface with an axial width of 4 mm or 7 mm. The angle of chamfer is 10 degrees and 45 degrees respectively. Axial widths of 4 mm or 7 mm are chosen because it is assumed that with the applied load conditions, these lengths still lead to conditions line contact EHL. The ring opposing the chamfered ring is unchamfered and has an axial width of 10 mm. The inner diameter of each ring is tapered at (2.86°) so as to enable a conical fit on the shaft.

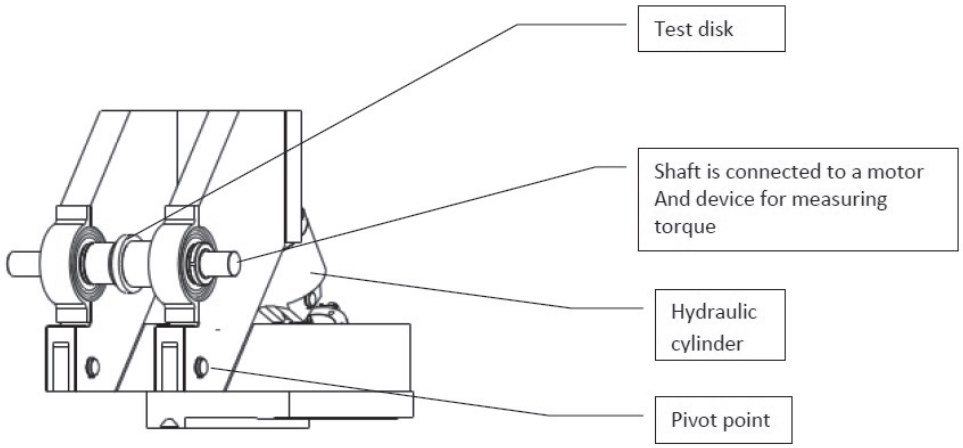

Figure 2.2: Permanent module of the test rig

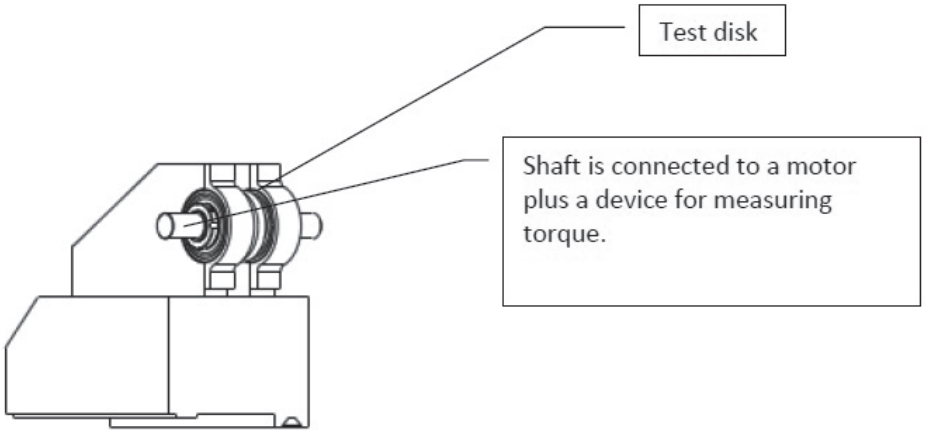

Figure 2.3: Non-conformal contact module of the test rig

The test-rig is used to conduct traction tests using grooved rings as well as RCF tests using hydrogen infused rings.

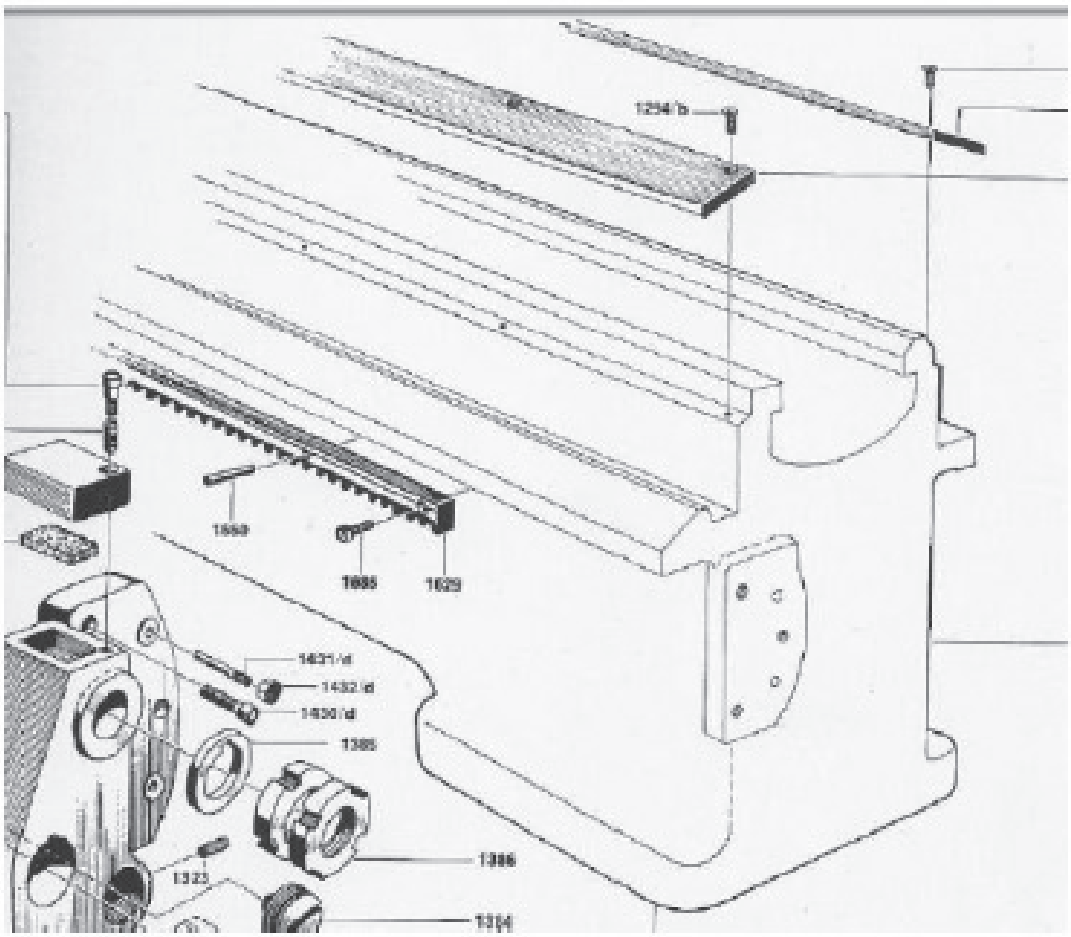

Figure 2.4: Support bars of a lathe on which modules are mounted

2.0.1 Relationship between hydraulic pressure and force exerted by piston

Applied load to the test ring: F_1 N
Force from hydraulic piston: F_2 N
Pressure in hydraulic cylinder: p_h Pa
Diameter of piston: d = 0.080 m
The distance from point A to contact force $F_1 = L_1$
The distance from point A to actuation force $F_2 = L_2$
$L_1 = 0.140$ m

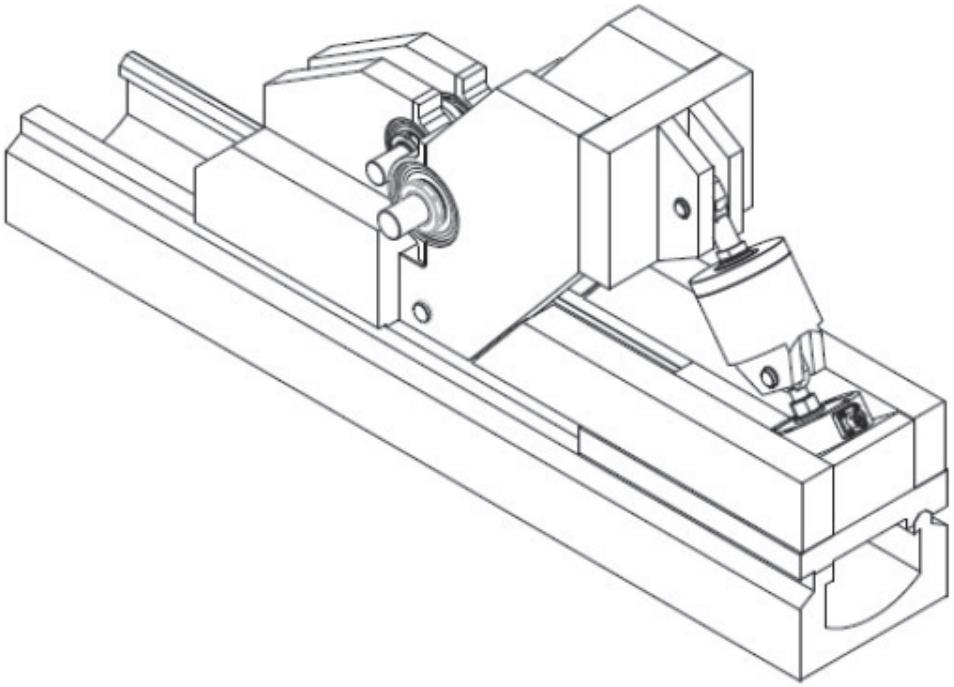

Figure 2.5: schematic of opposing modules, with the non-conformal module which can be slid along the lathe

$L_2 = 0.360\,\mathrm{m}$
The relationship is given by

$$p_h = \frac{F_2}{\pi \left(\frac{d}{2}\right)^2} \tag{2.1}$$

From Eq. 2.1 we get,

$$F_2 = p_h \pi \left(\frac{d}{2}\right)^2 \tag{2.2}$$

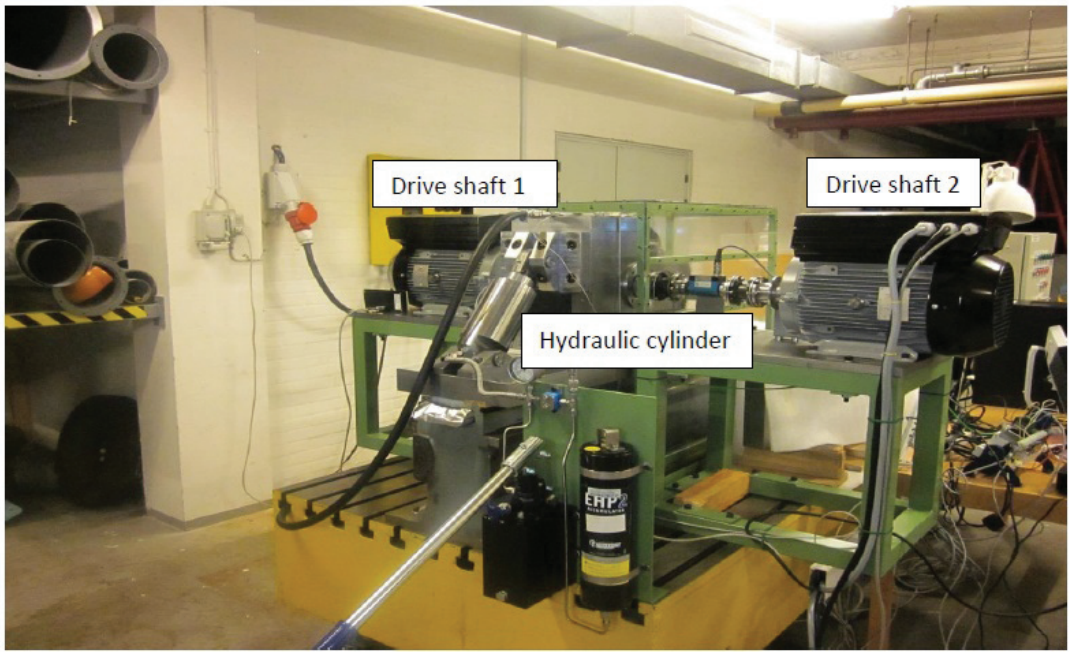

Figure 2.6: Picture of the Test Rig

2.0.2 Relationship between force exerted by piston and applied load to test ring

Taking the equilibrium of moments w.r.t A in Fig. 2.9, we get

$$F_1.L_1 - F_2.L_2 = 0 \tag{2.3}$$

$$F_1 = \frac{F_2.L_2}{L_1} \tag{2.4}$$

Using Eq. 2.2 we get

$$F_1 = \frac{p_h \pi \left(\frac{d}{2}\right)^2 (L_2)}{L_1} \tag{2.5}$$

Inserting the values of d, L_1 and L_2 we get

$$F_1 = (0.01293)p_h \tag{2.6}$$

Eq. 2.3 - Eq. 2.6 show the calculations involved in establishing the relationship between the pressure in the hydraulic cylinder (Fig. 2.8) p_h and the applied

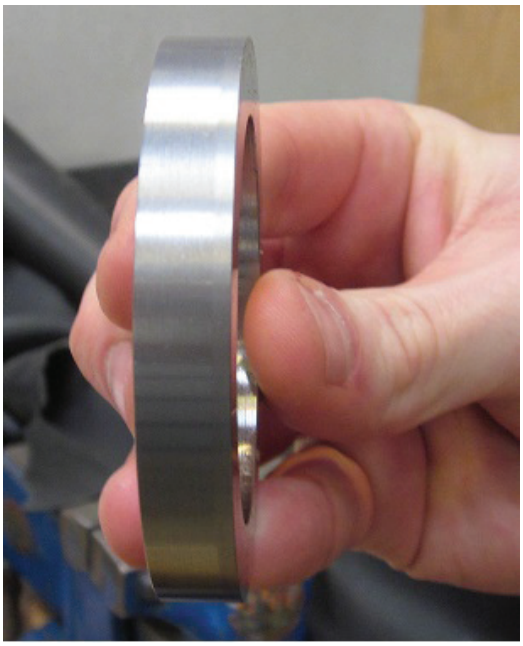

(a) Unchamfered test ring

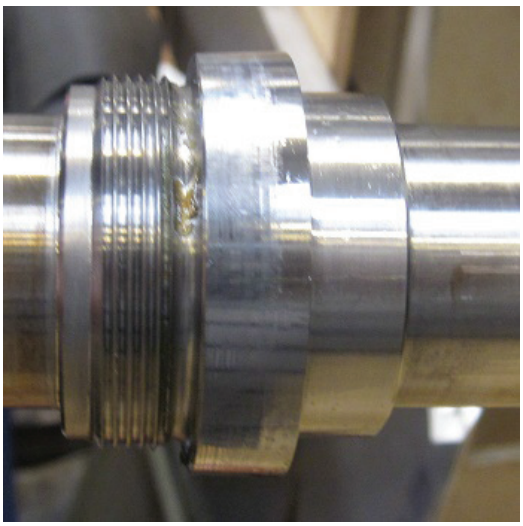

(b) cone on shaft

load to the test ring (Fig. 2.9) F_1. This load that is applied to the test ring can then be used to calculate the maximum Hertzian stress that is applied to the ring.

Thus the various components of the test-rig have been described and the method used to calculate the load on the test ring has been described in this chapter as well.

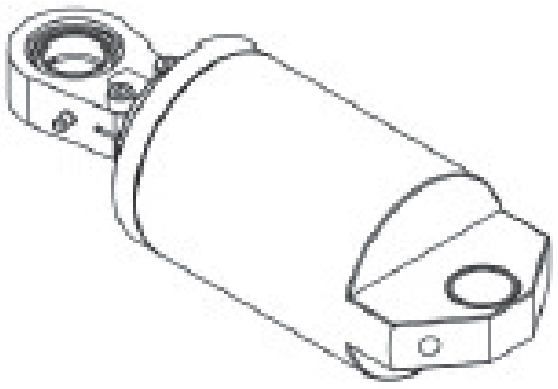

Figure 2.8: Hydraulic cylinder and piston

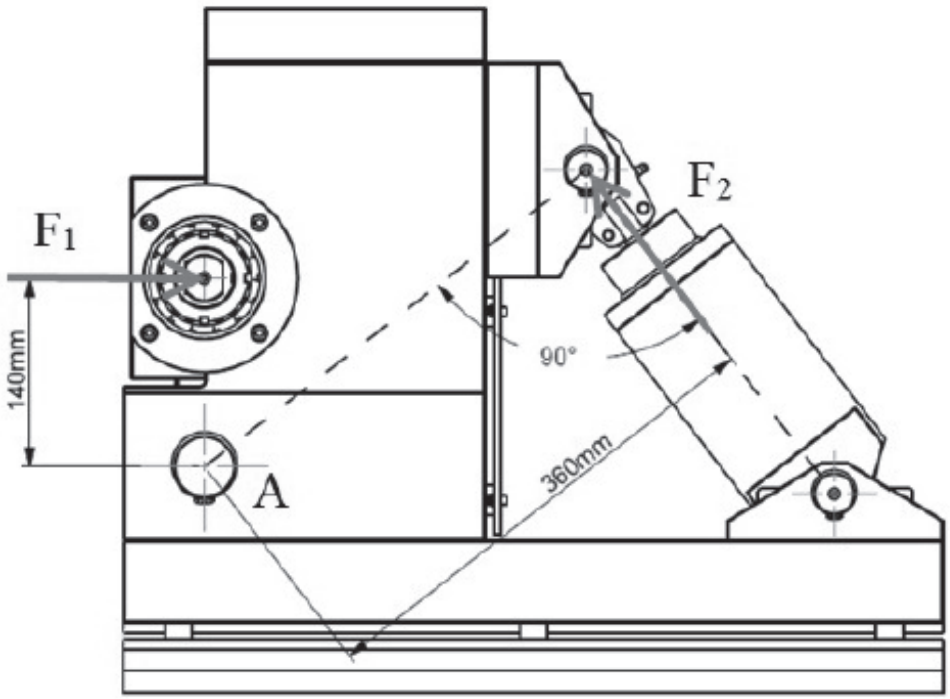

Figure 2.9: Diagram showing forces and dimensions

Chapter 3

EHL Modeling

3.1 Elastohydrodynamic Lubrication

Elastohydrodynamic lubrication (EHL) is a form of hydrodynamic lubrication where the pressures generated in the lubricant cause significant elastic deformation of the contacting surfaces. EHL conditions are often encountered in gears, rolling element bearings, cams etc. EHL usually occurs in non-conformal contacts because the converging film thickness of a viscous lubricant generates high pressures of the order greater than 1 GPa. There are two forms of EHL [2]

a. Hard EHL : Hard EHL refers to EHL occuring between high elastic modulus surfaces like metals. The EHL studied as part of this project refers to this form of EHL. The viscosity of the lubricant is significantly increased at these pressures. The viscosity at the center of the Hertzian contact is about 8-10 orders of magnitude greater than the value at the inlet.

b. Soft EHL : Soft EHL refers to the EHL occurring between surfaces with a low modulus of elasticity. Since elastic deformation can occur at lower pressures, the maximum EHL pressure in soft EHL is of the order of 1 MPa and the minimum film thickness is typically around 1 μm.

3.1.1 Viscosity-Pressure relationship

Under isothermal conditions, the viscosity and pressure are related to each other using either the Barus formula[3] or the Roelands formula[4].

The Barus relationship is

$$ln\left(\frac{\eta}{\eta_0}\right) = \psi p \tag{3.1}$$

where
η_0 absolute viscosity at p = 0 and reference temperature, N s/m^2
η absolute viscosity, N s/m^2
ψ pressure-viscosity coefficient of the lubricant, m^2/N
p pressure, N/m^2

The Roelands formula is

$$\bar{\eta} = \left(\frac{\eta_\infty}{\eta_0}\right)^{[1-(1+p/c_p)^{Z_1}]} \tag{3.2}$$

where
η_0 absolute viscosity at p = 0 and constant temperature, cP
$\bar{\eta}$ dimensionless absolute viscosity
$\eta_\infty = 6.31\text{x}10^{-5}$ N s/m^2
$c_p = 1.96\text{x}10^8$ N/m^2
Z_1 viscosity-pressure index, dimensionless constant
p pressure, N/m^2

The Roelands formaula has been shown to be more accurate at high pressures. Since this study deals with high pressures,the Roelands formula is used to calculate the pressure dependent viscosity in all the models.

A fine grid is required to capture the essential features of an EHL problem. The film thickness minima and the pressure spike at the conjunction outlet are highly localised phenomena. In certain cases, a coarse mesh can lead to a negative film thickness, which makes no physical sense. The extreme nonlinearity of the equations and a fine grid necessitate a stable and efficient solver.

[5] and [6] were the first to couple the Reynolds equation with the elastic deformation equation to predict the film thickness in EHL contacts. [7] provided the first view of the pressure spike occurring at the outlet of the EHL conjunction. [8] first solved the EHL line contact problem. A decade later [9] solved the circular contact problem.

3.2 Multigrid Method

The multigrid method was first used by [10] to solve highly loaded point and line contact EHL problems. Given the highly coupled and non-linear nature of the Reynolds equation, used for solving EHL problems, the solution to the equation is unstable at certain input parameters. The non-linearity of the Reynolds equations is caused by the pressure dependent coefficients and the cavitation conditions [11]. With greater mesh refinement, the convergence rate decreases.

[11] analysed simulation results to conclude that both the Jacobi and Gauss-Seidel relaxation schemes applied to one-dimensional problems are highly ineffective in reducing low frequency error components. They however concluded that these two relaxation schemes are very effective in reducing the the high frequency error components. The mathematical reasoning for this analysis is beyond the scope of this study. However the results of this analysis are important in understanding the principle of the multigrid method.

[11] showed that error components with wavelengths of the order of magnitude of the mesh size are reduced much faster than error components whose wavelengths are much larger than the mesh size. Thus a smooth error increases convergence time. However, the smooth error can be represented as a coarse error on a coarser mesh, thus enabling the error to be reduced faster on a coarse mesh compared to a fine mesh. Thus, the accuracy of the solution is best improved on a fine mesh, but the errors can be reduced much faster on a coarse mesh. This behaviour forms the underlying principle for using a multigrid scheme to solve EHL problems.

The error solving requires solving the Reynolds equation but with a new right hand side, except on the finest or target mesh. On the finest mesh, the right hand side of the Reynolds equation is not modified. The solution on the coarser grids leads to faster convergence by reducing the error components and fewer nodes in the coarser mesh leads to a faster solution time.

Once an iterative error approximation has been calculated on a coarsest mesh, it is interpolated to a finer mesh, and the solution at that level is improved. Each mesh is defined as a level in the multigrid solution. If the coarsest level has n+1 nodes, with n being an even number, then the next highest level (finer grid) has (2n+1) nodes. The coarsest level is always defined as level 1. For

example if level 1 has 7 nodes, then level 2 has 13 nodes, level 3 has 25 nodes, level 4 has 49 nodes and so on. The number of nodes on the coarsest grid and total number of levels required to solve the Reynolds equation is decided based on the required accuracy of the solution and the available computing time.

There are two ways of implementing a multigrid scheme. The coarse correction scheme (CS) is applied to linear equations. The full approximation scheme (FAS) is applied to both linear and non-linear equations. The FAS is used to solve Reynolds equation.

3.2.1 Full Approximation Scheme

The generalized equations describing the solution to a non-linear problem using the FAS are shown in this section.

$$L < u >= f \tag{3.3}$$

where L is the non-linear operator working on the unknown u. The discretized version of this equation is given by

$$L^h < \bar{u}^h >= f^h \tag{3.4}$$

where h is the mesh size.
An initial solution $\bar{v}^h$ is assumed to start the relaxation process. After a number of iterations on this level, an updated solution v^h is obtained. The residual is defined as

$$r^h = f^h - L^h < v^h > \tag{3.5}$$

The error vector e^h is defined as

$$e^h = \bar{u}^h - v^h \tag{3.6}$$

Substituting for v^h in Eq. 3.5 gives

$$r^h = f^h - L^h \left\langle \bar{u}^h - e^h \right\rangle \tag{3.7}$$

In Eq. 3.7, substituting for f^h and u^h from Eq. 3.4 and Eq. 3.6 respectively leads to

$$L^h \left\langle v^h + e^h \right\rangle = L^h \left\langle v^h \right\rangle + r^h \tag{3.8}$$

The coarse grid discretized equations are given by:

$$L^H \left\langle \bar{u}^H \right\rangle = f^H \tag{3.9}$$

where H is the mesh size on the coarse grid.

$$\left\langle \bar{u}^H \right\rangle = I_h^H \left(v^h + e^h \right) = I_h^H v^h + e^H \tag{3.10}$$

where I_h^H is an intergrid transfer operator

$$f^H = L^H \left\langle I_h^H v^h \right\rangle + I_h^H r^h \tag{3.11}$$

After a number of relaxations on the coarse grid, an updated value of $\left\langle \bar{u}^H \right\rangle$, $\left\langle u^H \right\rangle$ is obtained. The value of the variable on the fine grid v^h is then updated as:

$$\bar{u}^h = v^h + I_H^h \left(u^H - I_h^H v^h \right) \tag{3.12}$$

3.2.2 Intergrid Transfer

When moving from a fine grid to a coarse grid, the nodal residuals and pressures calculated on the fine grid are transferred to the appropriate nodes on the coarse grid as shown in Fig. 3.4. When moving from a coarse grid to a fine grid only the nodal pressures calculated on the coarse grid are transferred to the appropriate fine grid node as shown in Fig. 3.2.

3.2.3 W cycle

Fig. 3.3 shows the multigrid procedure using W cycles to solve Reynolds equation as described by [12]. A 4 level W(ν_1, ν_2) cycle based on the algorithm described in Fig. 3.3.

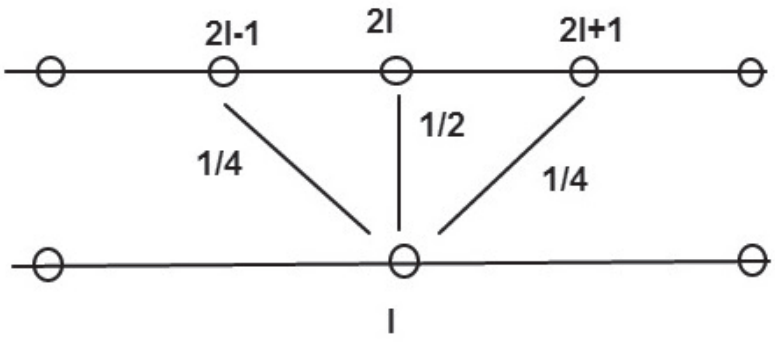

Figure 3.1: Transfer from a fine grid to a coarse grid

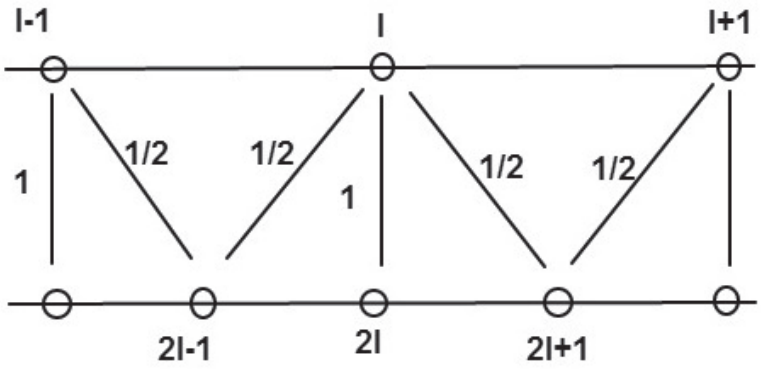

Figure 3.2: Transfer from a coarse grid to a fine grid

3.2.4 Relaxation Schemes

The Reynolds equation for an isothermal line contact problem can be written as [13]

$$L_i = \frac{1}{(\Delta X)^2}\left[\epsilon_{\frac{i-1}{2}} P_{i-1} - \left(\epsilon_{\frac{i-1}{2}} + \epsilon_{\frac{i-1}{2}}\right) P_i + \epsilon_{\frac{i+1}{2}} P_{i+1}\right] - \frac{1}{(\Delta X)}\left[H_i - H_{i-1}\right] \tag{3.13}$$

where $\epsilon = \frac{H^3}{\mu\gamma}$, $\gamma = \frac{3\pi^2 U}{(4w^2)}$, i = 2...N The film thickness formed by a combination

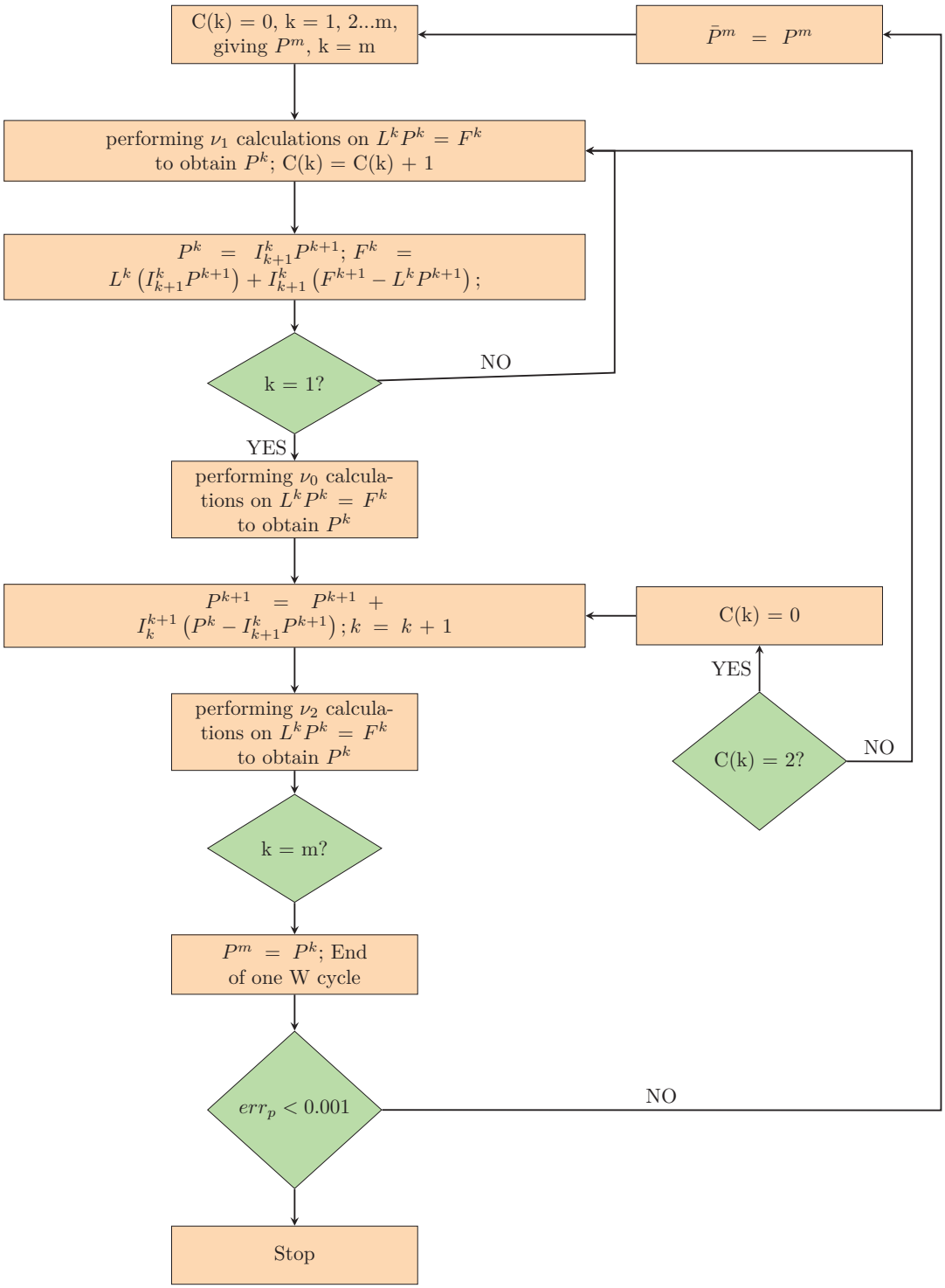

Figure 3.3: Iterative FAS multigrid scheme

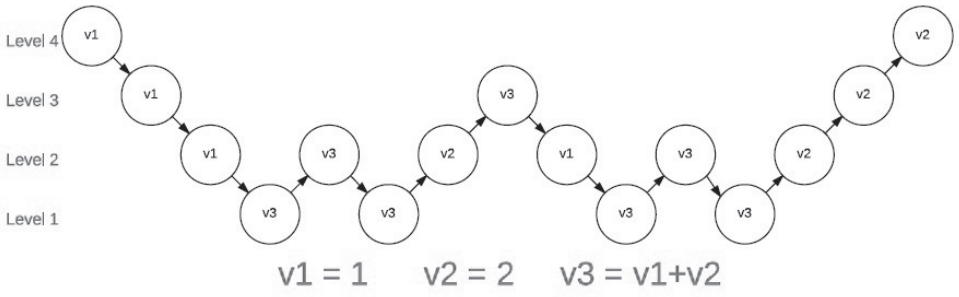

Figure 3.4: A 4 level W cycle based on the algorithm by [12]

of [14] and [13] and is

$$H_i = H_0 + \frac{{X_i}^2}{2} + \sum_{i=1}^{n} D_{ij} P_j - R(X_i) \tag{3.14}$$

The dimensionless film thickness H is not treated as independent variable but as a variable dependent on the dimensionless pressure, P.

The FAS is applied to solve the Reynolds equation on level k. Reynolds equation on level k is expressed as:

$$L^k P^k = F^k \tag{3.15}$$

where
F^k is the FAS right hand side vector. On the finest level $F^k = 0$. On the other level, F^k is calculated as:

$$F^k = L^k \left(I_{k+1}^k \bar{P}^{(k+1)} \right) + I_{k+1}^k \left(F^{k+1} - L^{k+1} \bar{P}^{(k+1)} \right) \tag{3.16}$$

where
$\bar{P}^{(k+1)}$ is the final pressure obtained after relaxation on level k+1.

The relaxation scheme used is comprised of a combination of the Gauss-Seidel scheme and the distributive Jacobi scheme. The Gauss-Seidel scheme is used primarily at the inlet where the viscosity values are much smaller compared

to the values at the contact center. The distributive Jacobi scheme is used at nodes close to the contact center where the viscosity values are high. Thus, a node is defined as a Gauss-Seidel node if:

$$\frac{\epsilon_i}{(\Delta X)^2} > 1 \tag{3.17}$$

Any node not relaxed using the Gauss-Seidel scheme is relaxed using a Jacobi scheme.
The residuals for the two schemes are defined as:

$$r_i = F_i^k - \frac{1}{(\Delta X)^2}\left[\epsilon_{\frac{i-1}{2}}\bar{P}_{i-1} - \left(\epsilon_{\frac{i-1}{2}} + \epsilon_{\frac{i-1}{2}}\right)P_i + \epsilon_{\frac{i+1}{2}}P_{i+1}\right] + \frac{1}{(\Delta X)}\left[H_i - H_{i-1}\right] \tag{3.18}$$

in the Gauss-Seidel region and

$$r_i = F_i^k - \frac{1}{(\Delta X)^2}\left[\epsilon_{\frac{i-1}{2}}P_{i-1} - \left(\epsilon_{\frac{i-1}{2}} + \epsilon_{\frac{i-1}{2}}\right)P_i + \epsilon_{\frac{i+1}{2}}P_{i+1}\right] + \frac{1}{(\Delta X)}\left[H_i - H_{i-1}\right] \tag{3.19}$$

in the Jacobi region respectively.
There is a subtle difference between the residual equation for the two relaxation schemes. The residual in the Gauss-Seidel region is formed by the updated nodal pressure at node (i-1)$\bar{P}_{i-1}$ and the 'old' pressures at node i and node (i+1), P_i and P_{i+1} respectively. The residual in the Jacobi region is formed only the 'old' pressures at nodes (i-1), i and (i+1).

The updated nodal pressure values are given by

$$\bar{P}_i = P_i + \omega_{gs}\delta_i \tag{3.20}$$

in the Gauss-Seidel region and

$$\bar{P}_i = P_i + \omega_{ja}\left(\delta_i - \delta_{(i-1)}\right) \tag{3.21}$$

in the Jacobi region where

ω_{gs} and ω_{ja} are the Gauss-Seidel and Jacobi under-relaxation factors respectively.
In the Gauss-Seidel region:

$$\delta_i = \left(\frac{\partial L_i}{\partial P_i}\right)^{-1} r_i \tag{3.22}$$

In the Jacobi region:

$$\delta_i = \left(\frac{\partial L_i}{\partial P_i} - \frac{\partial L_i}{\partial P_{i-1}}\right)^{-1} r_i \tag{3.23}$$

Differentiating Eq. 3.13

$$\left(\frac{\partial L_i}{\partial P_i}\right) = -\frac{1}{(\Delta X)^2}\left[\left(\epsilon_{\frac{i-1}{2}} + \epsilon_{\frac{i+1}{2}}\right)\right] - \frac{1}{(\Delta X)}\left[D_{ii} - D_{(i-1)i}\right] \tag{3.24}$$

$$\frac{\partial L_i}{\partial P_i} - \frac{\partial L_i}{\partial P_{i-1}} = -\frac{1}{(\Delta X)^2}\left[\left(2\epsilon_{\frac{i-1}{2}} + \epsilon_{\frac{i+1}{2}}\right)\right] - \frac{1}{(\Delta X)}\left[D_{ii} - D_{(i-1)i} - D_{i(i-1)} + D_{(i-1)(i-1)}\right] \tag{3.25}$$

The intergrid transfer operators are defined as shown in Fig. 3.4 and 3.2.

The force-balance equation on the finest level is

$$\frac{1}{2}\Delta X \sum_{j=1}^{N} (P_j + P_{j+1}) = \frac{\pi}{2} \tag{3.26}$$

At the end of each W(ν_1,ν_2)cycle, H_0 is adjusted using an under-relaxation factor of 0.001. If the left hand side of Eq. 3.26 is greater than $\frac{\pi}{2}$ then H_0 is increased. If the left hand side is lesser than $\frac{\pi}{2}$, then H_0 is decreased. This is done until the left hand side equals $\frac{\pi}{2}$.

The pressure convergence criterion is

$$err_p = \left(\frac{\sum_{j=1}^{N} |\bar{P}_i - P_i|}{\sum_{j=1}^{N} P_i} \right) < 0.001 \tag{3.27}$$

Once this criterion is reached, the solver is stopped and the converged values of pressure have been obtained.

3.3 Results of the multigrid method

The results of the multigrid simulations on the EHL problem are presented in this section.

A 4 level multigrid solution is obtained using W(1,2) cycles. The number of nodes on the finest level is 241 and the number of nodes on the coarsest level is 31. The inlet velocity is 1 m/s. The maximum Hertzian pressure, p_h is 1 GPa. The absolute viscosity at atmospheric pressure is 0.03 Pa s

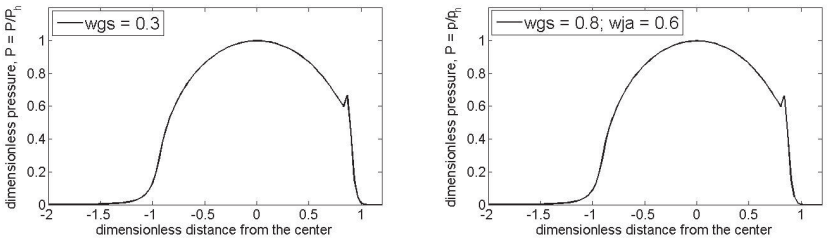

(a) wgs = 0.3 (b) wgs = 0.8; wja = 0.6

Figure 3.5: The EHL pressure curves calculated using the multigrid method. The solution method consists of 4 level W(1,2) cycles. The maximum Hertzian pressure p_h is 1 GPa. The lubricant inlet velocity is 1 m/s.

Fig. 3.5 and Fig. 3.6 show the EHL pressure and film thickness curves for two infinitely long rollers under lubricated contact. The converged curves have been obtained using the multigrid method. As has been explained earlier, it is possible to use two separate relaxation schemes to solve the Reynolds equation for large loads. Fig. 3.5a and Fig. 3.6a show the converged pressure and film

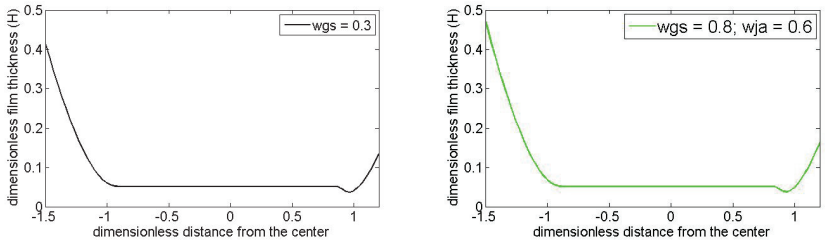

(a) wgs = 0.3 (b) wgs = 0.8; wja = 0.6

Figure 3.6: The EHL film thickness curves calculated using the multigrid method. The solution method consists of 4 level W(1,2) cycles. The maximum Hertzian pressure p_h is 1 GPa. The lubricant inlet velocity is 2 m/s.

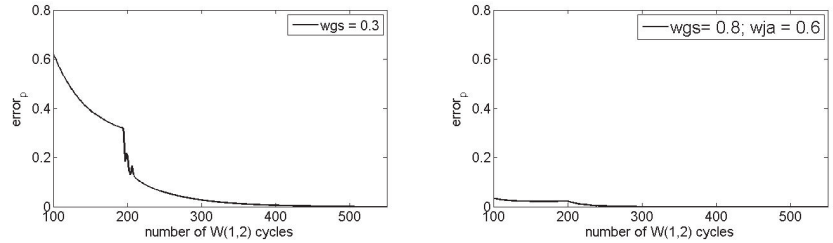

(a) wgs = 0.3 (b) wgs = 0.8; wja = 0.6

Figure 3.7: The convergence curves calculated using the multigrid method. The solution method consists of 4 level W(1,2) cycles. The maximum Hertzian pressure p_h is 1 GPa. The lubricant inlet velocity is 2 m/s.

thickness curves solved using just the Gauss-Seidel relaxation scheme. The under-relaxation factor used is 0.3. The number of W-cycles to convergence is 506 (Fig. 3.7a). Fig. 3.5b and Fig. 3.6b show the converged pressure and film thickness curves solved using a combination of the Gauss-Seidel relaxation scheme and the Jacobi relaxation scheme. The Gauss-Seidel under-relaxation factor is 0.8 and the Jacobi under-relaxation factor is 0.6. The number of W-cycles to convergence using the mixed relaxation scheme is 292 iterations (Fig. 3.7b. Simulations were run for various values of under-relaxation factors in both schemes. The results for the various values of under-relaxation values are shown in Fig. 3.8. Under-relaxation values for the Gauss-Seidel scheme greater than 0.3 did not produce convergence under the current input conditions. The Jacobi under-relaxation values for the mixed relaxation scheme greater than 0.6

did not produce convergence under the current input conditions. The Gauss-Seidel under-relaxation value was kept fixed at 0.8, while the the Jacobi values were varied.

The results show that the mixed relaxation scheme produced a faster convergence compared to the Gauss-Seidel relaxation scheme. This is because a Jacobi relaxation scheme is used in updating the nodal pressures in the Hertzian contact width region. The Jacobi scheme is more accurate than the Gauss-Seidel scheme because it updates nodal pressure values, by taking into account the pressure values at the neighbouring nodes. The Gauss-Seidel scheme does not use the pressure values at the neighbouring nodes to update nodal pressures. This introduces errors, which take more number of iterations to smooth out. In Fig. 3.7a it is observed that the $error_p$ value decreases steadily until about 200 iterations. Then a sudden increase in convergence rate is observed. This occurs when the integral of the dimensionless nodal pressures equals $\frac{\pi}{2}$.

Multigrid simulations are also run for higher levels of solution. Comparisons of the results at the different levels of solution are presented in Publication A.

3.4 Non-Newtonian EHL model

A mathematical model to calculate the interfacial pressures, film thickness and shear stresses in EHL contacts at low slide-roll ratios (SRRs) and loads is described in this section. Classical EHL theory deals with a Newtonian lubricant. A Newtonian lubricant is one where the lubricant shear stress varies linearly with the shear rate. The Newtonian model used to predict EHL line contact pressures and film thickness assumes isothermal conditions throughout the conjunction [15]. However at high SRRs and loads, the assumption of isothermal conditions is invalid because of the effect of shear and squeeze heating [16]. At high SRR, the heat generated per unit volume is very large($approx.100$ TW/m^3) giving rise to a large increase in temperature. This causes a decrease in the viscosity and the limiting shear strength of the oil. Hence the isothermal model cannot accurately describe the lubricant behaviour at high SRR.The model described in this section deals with low SRRs and loads and is based on the model developed by [15]. Hence it is an isothermal problem.

The geometry of the problem is a roller, rolling and sliding against an infinitely long half plane. The radius of the roller is much smaller compared to its length.

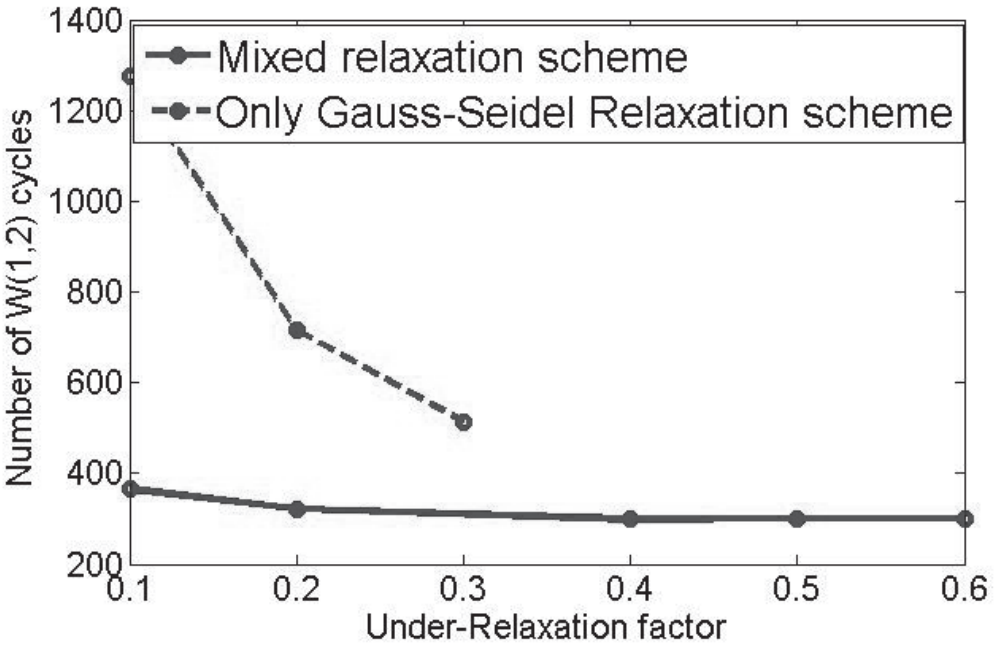

Figure 3.8: Comparing the number of cycles to failure using various under-relaxation values. The solution method consists of 4 level W(1,2) cycles. The maximum Hertzian pressure p_h is 1 GPa. The lubricant inlet velocity is 2 m/s.

In the non-Newtonian model in this study, if the lubricant shear stress exceeds the limiting shear strength of the lubricant, then the value of shear stress is set to the limiting value. The fluid model is considered Newtonian until this shear strength value is reached. When the lubricant is unable to take on any more shear, then slip occurs at the interface between the lubricant and the solid surface.

The non-Newtonian model described here was developed by [17] and considers the velocity of the lubricant at the solid-lubricant interface to define the non-Newtonian behaviour of the conjunction. Fig. 3.9 and Fig. 3.10 depict the 5 different zones that can occur in an EHL conjunction experiencing rolling and sliding. In each figure, the velocity of the top surface (u_a) is greater than the bottom surface (u_b). In Fig. 3.9, zone 0 refers to the Newtonian zone where, the lubricant behaves as a Newtonian lubricant and no slip occurs at either of the two surfaces. In Fig. 3.9, $\frac{dp}{dx} > 0$. In Zone 1 of the same figure, the

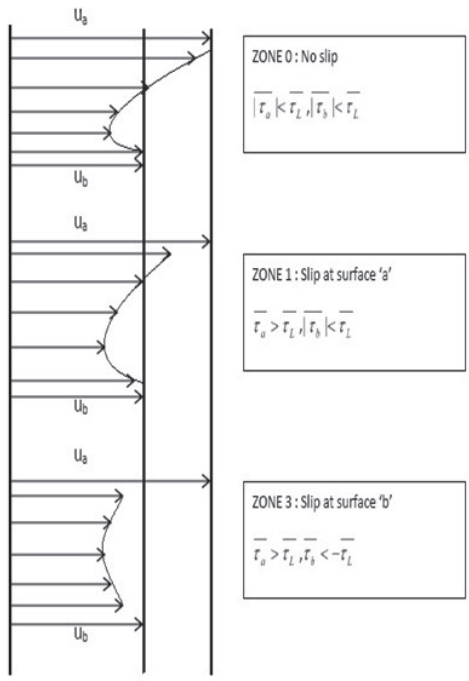

Figure 3.9: Velocity distribution at $\frac{\partial p}{\partial x} > 0$

velocity of the lubricant is lesser than that of the top surface and slip occurs. There is no slip at the bottom surface. In Zone 3, slip occurs at both the top and bottom surface, and the shear stress values at both interfaces are set to the limiting shear strength value. In Fig. 3.10 the velocity distributions are shown for those parts of the conjunction where $\frac{\partial p}{\partial x} < 0$. In Zone 2 of this figure, slippage occurs at the bottom surface and in Zone 4, slippage occurs at both surfaces, with the velocities of the lubricant being greater than u_a and u_b.

3.4.1 Theory

The velocity profile is defined as

$$u = \frac{(z^2 - zh)}{2\eta}\frac{dp}{dx} + \frac{u_b(h-z)}{h} + \frac{u_a z}{h} \tag{3.28}$$

where
z is the coordinate in the film thickness direction (m)
h is the film thickness (m)

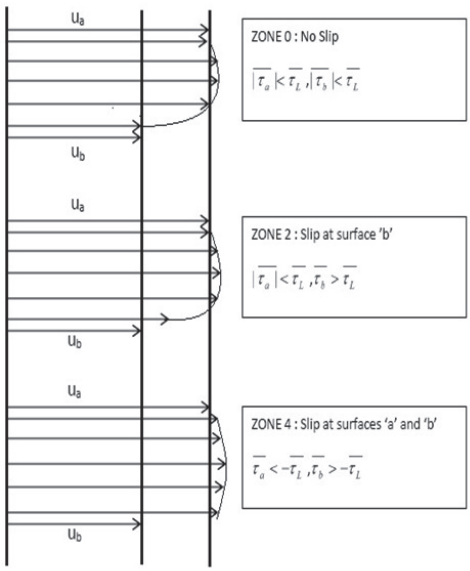

Figure 3.10: Velocity distribution at $\frac{\partial p}{\partial x} < 0$

η is the lubricant viscosity [Pas]
p is the pressure [Pa]

The velocity gradient is

$$\frac{du}{dz} = \frac{2z - h}{2\eta}\frac{dp}{dx} + \frac{u_a - u_b}{h} \tag{3.29}$$

The shear stress at surface a is

$$\tau_a = (\tau)_{z=h} = \eta\left(\frac{du}{dz}\right)_{z=h} = \frac{h}{2}\frac{dp}{dx} + \frac{(u_a - u_b)\eta}{h} \tag{3.30}$$

The shear stress at surface b is

$$\tau_b = (\tau)_{z=0} = \eta\left(\frac{du}{dz}\right)_{z=0} = -\frac{h}{2}\frac{dp}{dx} + \frac{(u_a - u_b)\eta}{h} \tag{3.31}$$

The dimensionless limiting shear stress is defined as

$$\bar{\tau}_L = \bar{\tau}_0 + \gamma P \tag{3.32}$$

where
$\bar{\tau}_0$ is the dimensionless initial shear stress constant. In this model we use a value of 9x10^{-5}
γ is the limiting shear strength proportionality constant. It's value usually lies between 0.07 and 0.1

The variables are made dimensionless using the following equations:

$$H = h/R \tag{3.33}$$

H is the dimensionless film thickness
R is the effective radius in m

$$W = \frac{w_z}{ER} \tag{3.34}$$

W is the dimensionless load parameter
w_z is the load/unit length in N/m
E is the equivalent Youngs Modulus in Pa

$$U = \frac{\eta_0 u_s}{ER} \tag{3.35}$$

U is the dimensionless speed parameter
η_0 is the viscosity at base pressure in Pa s
u_s is the avg. velocity of the 2 surfaces, $\frac{u_a+u_b}{2}$ in m/s

$$U^* = \frac{u_a - u_b}{u_a + u_b} \tag{3.36}$$

U^* is the dimensionless sliding velocity

$$X = \frac{x}{b} \tag{3.37}$$

X is a dimensionless coordinate

$$Z = \frac{z}{h} \tag{3.38}$$

Z is a dimensionless coordinate

$$b = R\sqrt{\frac{8W}{\pi}} \tag{3.39}$$

b is the Hertzian contact half-width

$$\bar{\eta} = \frac{\eta}{\eta_0} \tag{3.40}$$

$\bar{\eta}$ is the dimensionless viscosity

$$P = \frac{p}{E} \tag{3.41}$$

P is the dimensionless pressure

$$\bar{\tau}_a = \frac{\tau_a}{E} \tag{3.42}$$

$\bar{\tau}_a$ is the dimensionless shear stress at the top surface

$$\bar{\tau}_b = \frac{\tau_b}{E} \tag{3.43}$$

$\bar{\tau}_a$ is the dimensionless shear stress at the bottom surface

The pressure equations are described for each zone in the following subsections. The pressure equation describes the flow of the lubricant in each section. Solving the pressure equation provides the nodal pressures. The pressure equations are solved using a Jacobian matrix. The elements of the Jacobian matrix are also derived for each section.

Fig. 3.9 and Fig. 3.10 describe the surface velocities and slip behaviour at the top and bottom surfaces for positive and negative pressure gradient values respectively.

3.4.2 Zone 0

In zone 0, the Newtonian regime is valid and no slip occurs at either the top or the bottom surface.

The dimensionless velocity is defined as

$$UU = \frac{H^2 Z(Z-1)}{4\bar{\eta}U}\sqrt{\frac{\pi}{2W}}\frac{dP}{dX} + 1 - U^*(1-2Z) \tag{3.44}$$

The dimensionless velocity gradient is defined as

$$\frac{d(UU)}{dZ} = \frac{H^2(2Z-1)}{4\bar{\eta}U}\sqrt{\frac{\pi}{2W}}\frac{dP}{dX} + 2U^* \tag{3.45}$$

The dimensionless shear stress at the upper surface 'a' is

$$\bar{\tau_a} = \frac{2UU^*\bar{\eta}}{H} + \frac{H}{4}\sqrt{\frac{\pi}{2W}}\frac{dP}{dX} \tag{3.46}$$

The dimensionless shear stress at the lower surface 'b' is

$$\bar{\tau_b} = \frac{2UU^*\bar{\eta}}{H} - \frac{H}{4}\sqrt{\frac{\pi}{2W}}\frac{dP}{dX} \tag{3.47}$$

The pressure equation in Zone 0 describing the flow of the Newtonian lubricant, with no side leakage is described as

$$\frac{\partial}{\partial X}\left(\frac{H^3}{12\bar{\eta}}\frac{\partial P}{\partial X}\right) = 24U\sqrt{\frac{2W}{\pi}}\left(\frac{\partial H}{\partial X}\right) \tag{3.48}$$

Integrating wrt X we get

$$\frac{H^3}{\bar{\eta}}\frac{dP}{dX} = KH + A \tag{3.49}$$

where $K = 288U\sqrt{\frac{2W}{\pi}}$

Applying the boundary conditions, $\frac{dP}{dX} = 0$ at $X = X_m$ and $H = H_m$ we get

$$A = -KH_m \tag{3.50}$$

Substituting for A in Eq. 3.49, we get

$$\frac{dP}{dX} = K\bar{\eta}\left(\frac{H - H_m}{H^3}\right) \tag{3.51}$$

The functional at each node is thus

$$f_i = H_i^3\left(\frac{dP}{dX}\right)_i - K\bar{\eta_i}\left(H_i - H_m\right) \tag{3.52}$$

The dimensionless film thickness H_i is given by

$$H_i = H_0 + \frac{X_i^2}{2} + \sum_{j=1}^{N} D_{ij}P_j \tag{3.53}$$

The dimensionless viscosity is given by

$$\bar{\eta_i} = exp\left\{[ln(\eta_0) + 9.67][-1 + (1 + 5.1 \times 10^{-9} p_H P_i)^{Z_1}]\right\} \tag{3.54}$$

The Jacobian factors are

$$\frac{\partial f_i}{\partial P_j} = 3H_i^2 \left(\frac{dP}{dX}\right)_i D_{i,j} + H_i^3 \frac{\partial[\left(\frac{dP}{dX}\right)_i]}{\partial P_j} - K\frac{\partial \bar{\eta_i}}{\partial P_j}(H_i - H_m) - K\bar{\eta_i} D_{i,j} \tag{3.55}$$

$$\frac{\partial f_i}{\partial H_m} = K\bar{\eta_i} \tag{3.56}$$

$$\frac{\partial f_i}{\partial H_0} = 3{H_i}^2 \left(\frac{\partial P}{\partial X}\right)_i - K\bar{\eta_i} \tag{3.57}$$

Differentiating the film thickness, H_i we get

$$\frac{\partial H_i}{\partial H_0} = 1 \tag{3.58}$$

$$\frac{\partial H_i}{\partial P_j} = D_{i,j} \tag{3.59}$$

3.4.3 Zone 1

In zone 1, $|\bar{\tau_a}| > \bar{\tau_L}$ and $|\bar{\tau_b}| < \bar{\tau_L}$. Since, $|\bar{\tau_a}| > \bar{\tau_L}$, $|\bar{\tau_a}|$ is set to τ_L. Slip occurs at the top surface 'a' in zone 1.

The slip velocity at surface a is

$$\tilde{u_a} = u_b + \frac{\tau_L h}{\eta} - \frac{h^2}{2\eta}\frac{dp}{dx} \tag{3.60}$$

The dimensionless velocity is defined as

$$UU = \frac{H^2 Z(Z-2)}{4\bar{\eta}U}\sqrt{\frac{\pi}{2W}}\frac{dP}{dX} + (1 - U^*) + \frac{\bar{\tau}_L H Z}{\bar{\eta}U} \tag{3.61}$$

The dimensionless velocity gradient is

$$\frac{d(UU)}{dZ} = \frac{H^2(Z-1)}{2\bar{\eta}U}\sqrt{\frac{\pi}{2W}}\frac{dP}{dX} + \frac{\bar{\tau}_L H}{\bar{\eta}U} \tag{3.62}$$

The dimensionless shear stress at surface b is

$$\bar{\tau_b} = \bar{\tau_L} - \frac{H}{2}\sqrt{\frac{\pi}{2W}}\frac{dP}{dX} \tag{3.63}$$

The pressure equation for zone 1 is now defined as

$$\frac{\partial}{\partial X}\left(\frac{H^3}{\bar{\eta}}\frac{\partial P}{\partial X}\right) = 6U\sqrt{\frac{2W}{\pi}}\left[(1-U^*)\frac{\partial H}{\partial X} + \frac{1}{2U}\frac{d}{dX}\left(\frac{H^2\tau_L}{\bar{\eta}}\right)\right] \tag{3.64}$$

Integrating w.r.t X

$$\left(\frac{H^3}{\bar{\eta}}\frac{\partial P}{\partial X}\right) = 6U\sqrt{\frac{2W}{\pi}}\left[(1-U^*)H + \frac{1}{2U}\left(\frac{H^2\tau_L}{\bar{\eta}}\right) + A\right] \tag{3.65}$$

Applying Boundary Conditions $\frac{dP}{dX} = 0$ at $X = X_m$ and $H = H_m$

$$A = -\left[(1-U^*)(H_m) + \frac{1}{2U}\frac{{H_m}^2\tau_{Lm}}{\bar{\eta_m}}\right] \tag{3.66}$$

Eq. 3.65 now becomes

$$\left(H^3\frac{\partial P}{\partial X}\right) = 6U\sqrt{\frac{2W}{\pi}}\bar{\eta}\left[(1-U^*)H + \frac{1}{2U}\left(\frac{H^2\tau_L}{\bar{\eta}}\right) - (1-U^*)(H_m) - \frac{1}{2U}\frac{{H_m}^2\tau_{Lm}}{\bar{\eta_m}}\right] \tag{3.67}$$

The functional at node i is now defined as

$$\begin{aligned} f_i = {H_i}^3\left(\frac{\partial P}{\partial X}\right)_i &- 6U\sqrt{\frac{2W}{\pi}}\bar{\eta}_i\left[(1-U^*)H_i\right] \\ &- 6U\sqrt{\frac{2W}{\pi}}\bar{\eta}_i\left[\left(\frac{H_i^2\tau_{Li}}{\bar{\eta}_i}\right) - (1-U^*)(H_m) - \frac{1}{2U}\frac{{H_m}^2\tau_{Lm}}{\bar{\eta}_m}\right] = 0 \end{aligned} \tag{3.68}$$

Let $6U\sqrt{\frac{2W}{\pi}} = K$ and rearranging terms we get

$$f_i = {H_i}^3 \left(\frac{\partial P}{\partial X}\right)_i - K\bar{\eta_i}\left[(1-U^*)H_i + \frac{1}{2U}\left(\frac{H_i^2\tau_{Li}}{\bar{\eta_i}}\right) - (1-U^*)(H_m) - \frac{1}{2U}\frac{{H_m}^2\tau_{Lm}}{\bar{\eta}_m}\right] = 0 \tag{3.69}$$

Defining the elements of the Jacobian matrix

$$\begin{aligned}\frac{\partial f_i}{\partial P_j} = {} & 3{H_i}^2\left(\frac{\partial P}{\partial X}\right)_i D_{ij} + {H_i}^3\frac{\partial\left(\frac{\partial P}{\partial X}\right)_i}{\partial P_j} \\ & - K\bar{\eta_i}(1-U^*)D_{ij} - KH_i(1-U^*)\frac{\partial\bar{\eta_i}}{\partial P_j} - \frac{K}{2U}\left[2(\bar{\tau_L})_i H_i D_{ij} + {H_i}^2\gamma\delta_{ij}\right] \\ & + KH_m(1-U^*)\frac{\partial\bar{\eta_i}}{\partial P_j}\delta_{ij} \\ & + \frac{K\tau_{Lm}{H_m}^2}{2U\bar{\eta_m}}\frac{\partial\bar{\eta_i}}{\partial P_j}\end{aligned} \tag{3.70}$$

$$\frac{\partial f_i}{\partial H_m} = K\bar{\eta_i}(1-U^*) + \frac{K\bar{\eta_i}\tau_{Lm}H_m}{U\bar{\eta_m}} \tag{3.71}$$

$$\frac{\partial f_i}{\partial H_0} = 3{H_i}^2\left(\frac{\partial P}{\partial X}\right)_i - K\bar{\eta_i}(1-U^*) - \frac{K(\bar{\tau_L})_i H_i}{U} \tag{3.72}$$

3.4.4 Zone 2

In zone 2, $\bar{\tau_a} < \bar{\tau_L}$ and $\bar{\tau_b} > \bar{\tau_L}$. Since, $\bar{\tau_b} > \bar{\tau_L}$, $\bar{\tau_b}$ is set to τ_L. In this zone, slip occurs at the bottom surface.

The slip velocity at surface b is

$$\tilde{u_b} = u_a - \frac{\tau_L h}{\eta} - \frac{h^2}{2\eta}\frac{dp}{dx} \tag{3.73}$$

The dimensionless velocity is defined as

$$UU = \frac{H^2(Z^2-1)}{4\bar{\eta}U}\sqrt{\frac{\pi}{2W}}\frac{dP}{dX} + (1+U^*) - \frac{\bar{\tau_l}H(1-Z)}{\bar{\eta}U} \tag{3.74}$$

The dimensionless velocity gradient is

$$\frac{d(UU)}{dZ} = \frac{H^2 Z}{2\bar{\eta}U}\sqrt{\frac{\pi}{2W}}\frac{dP}{dX} + \frac{\bar{\tau}_l H}{\bar{\eta}U} \tag{3.75}$$

The dimensionless shear stress at surface a is

$$\bar{\tau_a} = \bar{\tau_L} + \frac{H}{2}\sqrt{\frac{\pi}{2W}}\frac{dP}{dX} \tag{3.76}$$

In zone 2, $|\bar{\tau_a}| < \bar{\tau_L}$. Based on Eq. 3.76 will be negative when $\frac{dP}{dX}$ is negative.

The pressure equation for zone 2 is

$$\frac{\partial}{\partial X}\left(\frac{H^3}{\bar{\eta}}\frac{\partial P}{\partial X}\right) = 6U\sqrt{\frac{2W}{\pi}}\left[(1+U^*)\frac{\partial H}{\partial X} - \frac{1}{2U}\frac{d}{dX}\left(\frac{H^2\tau_L}{\bar{\eta}}\right)\right] \tag{3.77}$$

Integrating w.r.t X

$$\left(\frac{H^3}{\bar{\eta}}\frac{\partial P}{\partial X}\right) = 6U\sqrt{\frac{2W}{\pi}}\left[(1+U^*)H - \frac{1}{2U}\left(\frac{H^2\tau_L}{\bar{\eta}}\right) + A\right] \tag{3.78}$$

Applying Boundary Conditions $\frac{dP}{dX} = 0$ at $X = X_m$ and $H = H_m$

$$A = -\left[(1+U^*)(H_m) - \frac{1}{2U}\frac{{H_m}^2\tau_{Lm}}{\bar{\eta_m}}\right] \tag{3.79}$$

Eq. 3.78 now becomes

$$\left(\frac{H^3}{\bar{\eta}}\frac{\partial P}{\partial X}\right) = 6U\sqrt{\frac{2W}{\pi}}\left[(1+U^*)H - \frac{1}{2U}\left(\frac{H^2\tau_L}{\bar{\eta}}\right) - (1+U^*)(H_m) + \frac{1}{2U}\frac{{H_m}^2\tau_{Lm}}{\bar{\eta_m}}\right] \tag{3.80}$$

The functional at node i is now defined as

$$f_i = \frac{H_i^3}{\bar{\eta}_i}\left(\frac{\partial P}{\partial X}\right)_i - 6U\sqrt{\frac{2W}{\pi}}\left[(1+U^*)H_i - \frac{1}{2U}\left(\frac{H_i^2\tau_{Li}}{\bar{\eta_i}}\right) - (1+U^*)(H_m)\right] - 6U\sqrt{\frac{2W}{\pi}}\left[\frac{1}{2U}\frac{{H_m}^2\tau_{Lm}}{\bar{\eta_m}}\right] = 0 \tag{3.81}$$

Let $6U\sqrt{\frac{2W}{\pi}} = K$ and rearranging terms we get

$$f_i = H_i^3 \left(\frac{\partial P}{\partial X}\right)_i - K\bar{\eta_i}\left[(1+U^*)H_i - \frac{1}{2U}\left(\frac{H_i^2\tau_{Li}}{\bar{\eta_i}}\right) - (1+U^*)(H_m) + \frac{1}{2U}\frac{{H_m}^2\tau_{Lm}}{\bar{\eta_m}}\right] = 0 \tag{3.82}$$

Defining the elements of the Jacobian matrix

$$\begin{aligned}\frac{\partial f_i}{\partial P_j} = {3H_i}^2 \left(\frac{\partial P}{\partial X}\right)_i D_{ij} + {H_i}^3 \frac{\partial\left(\frac{\partial P}{\partial X}\right)_i}{\partial P_j} \\ - K\bar{\eta_i}(1+U^*)D_{ij} - KH_i(1+U^*)\frac{\partial\bar{\eta_i}}{\partial P_j} + \frac{K}{2U}\left[2(\bar{\tau_L})_i H_i D_{ij} + {H_i}^2\gamma\delta_{ij}\right] \\ + KH_m(1+U^*)\frac{\partial\bar{\eta_i}}{\partial P_j} \\ - \frac{K\tau_{Lm}{H_m}^2}{2U\bar{\eta_m}}\frac{\partial\bar{\eta_i}}{\partial P_j}\end{aligned} \tag{3.83}$$

$$\frac{\partial f_i}{\partial H_m} = K\bar{\eta_i}(1+U^*) - \frac{K\bar{\eta_i}\tau_{Lm}H_m}{U\bar{\eta_m}} \tag{3.84}$$

$$\frac{\partial f_i}{\partial H_0} = {3H_i}^2\left(\frac{\partial P}{\partial X}\right)_i - K\bar{\eta_i}(1-U^*) + \frac{K(\bar{\tau_L})_i H_i}{U} \tag{3.85}$$

3.4.5 Zone 3

In zone 3, slip occurs at both the top and bottom surfaces. $\bar{\tau}_a > \bar{\tau}_L$ and $\bar{\tau}_b \leq -\bar{\tau}_L$. Since $\bar{\tau}_a > \bar{\tau}_L$, $\bar{\tau}_a$ is set to $\bar{\tau}_L$. Since $\bar{\tau}_b \leq -\bar{\tau}_L$, $\bar{\tau}_b$ is set to $-\bar{\tau}_L$.

The pressure equation in zone 3 is

$$\frac{\partial P}{\partial X} = 4\sqrt{\frac{2W}{\pi}}\frac{\tau_L}{H} \tag{3.86}$$

The functional at node i is defined as

$$f_i = \left(\frac{\partial P}{\partial X}\right)_i - 4\sqrt{\frac{2W}{\pi}}\frac{\tau_{Li}}{H_i} = 0 \tag{3.87}$$

The elements of the Jacobian matrix are defined as

$$\frac{\partial f_i}{\partial P_j} = \frac{\partial \left(\frac{\partial P}{\partial X}\right)_i}{\partial P_j} - 4\sqrt{\frac{2w}{\pi}}\left[\frac{H_i\gamma\delta_{ij} - (\bar{\tau_L})_i D_{ij}}{{H_i}^2}\right] \tag{3.88}$$

$$\frac{\partial f_i}{\partial H_m} = 0 \tag{3.89}$$

$$\frac{\partial f_i}{\partial H_0} = 4\sqrt{\frac{2w}{\pi}}\frac{(\bar{\tau_L})_i}{{H_i}^2} \tag{3.90}$$

3.4.6 Zone 4

In zone 4, slip occurs at both the top and bottom surfaces. This is similar to the conditions in zone 3. However in zone 3, the slip velocity is smaller than the slower surface velocity (bottom surface), while in zone 4, the slip velocity is greater than the faster surface velocity (top surface). In this zone $\bar{\tau}_b > \bar{\tau}_L$ and $\bar{\tau}_a \leq -\bar{\tau}_L$. Hence $\bar{\tau}_b$ is set to $\bar{\tau}_L$ and $\bar{\tau}_a$ is set to $-\bar{\tau}_L$. For a node to be in zone 3, $\frac{dP}{dX}$ is positive, while it is negative in zone 4.

$$\frac{\partial P}{\partial X} = -4\sqrt{\frac{2W}{\pi}}\frac{\tau_L}{H} \tag{3.91}$$

The functional at node i is defined as

$$f_i = \left(\frac{\partial P}{\partial X}\right)_i + 4\sqrt{\frac{2W}{\pi}}\frac{\tau_L}{H} = 0 \tag{3.92}$$

The elements of the Jacobian matrix are defined as

$$\frac{\partial f_i}{\partial P_j} = \frac{\partial \left(\frac{\partial P}{\partial X}\right)_i}{\partial P_j} + 4\sqrt{\frac{2w}{\pi}}\left[\frac{H_i\gamma\delta_{ij} - (\bar{\tau_L})_i D_{ij}}{{H_i}^2}\right] \tag{3.93}$$

$$\frac{\partial f_i}{\partial H_m} = 0 \tag{3.94}$$

$$\frac{\partial f_i}{\partial H_0} = -4\sqrt{\frac{2w}{\pi}}\frac{(\bar{\tau_L})_i}{{H_i}^2} \tag{3.95}$$

3.5 Solution Method

Since the Reynolds Equation is a highly coupled non-linear equation, the Newton-Raphson method is used to solve a set of linearized equations.

If $f_n(x) = 0$ is a set of n equations, with n ranging from 1...n and if X is an n-dimensional vector of n unknowns, then the Newton Raphson formula for calculating the increment in the values of unknowns after an iteration is

$$\delta x = -J^{-1}(x) f(x) \tag{3.96}$$

The new values of the unknowns are then updated as

$$x_{new} = x_{old} + \delta x = x_{old} - J^{-1}(x) f(x) \tag{3.97}$$

$J(x)$ is the Jacobian matrix of size n x n.

$$[J] = \begin{bmatrix} \frac{\partial f_1}{\partial H_m} & \frac{\partial f_1}{\partial P_2} & \cdots & \frac{\partial f_1}{\partial P_N} & \frac{\partial f_1}{\partial H_0} \\ \frac{\partial f_2}{\partial H_m} & \frac{\partial f_2}{\partial P_2} & \cdots & \frac{\partial f_2}{\partial P_N} & \frac{\partial f_2}{\partial H_0} \\ . & . & . & . & . \\ . & . & . & . & . \\ . & . & . & . & . \\ \frac{\partial f_N}{\partial H_m} & \frac{\partial f_N}{\partial P_2} & \cdots & \frac{\partial f_N}{\partial P_N} & \frac{\partial f_N}{\partial H_0} \\ 0 & C_2 & ... & C_N & 0 \end{bmatrix} \tag{3.98}$$

C_j are weighting factors described in Appendix A.

$$[F] = \begin{bmatrix} -\mathbf{f_1} \\ -\mathbf{f_2} \\ . \\ . \\ . \\ -\mathbf{f_N} \\ \triangle \mathbf{W} \end{bmatrix} \tag{3.99}$$

$$\{X\} = \begin{Bmatrix} \triangle(\mathbf{H_m}) \\ \triangle(\mathbf{P_2}) \\ . \\ . \\ . \\ \triangle(\mathbf{P_N}) \\ \triangle(\mathbf{H_0}) \end{Bmatrix}. \tag{3.100}$$

Using the Gaussian elimination method the following set of linearised equations are solved

$$[J]\{X\} = [F] \tag{3.101}$$

The equations to calculate the elastic deformations at each node i are described in Appendix B.

Fig. 3.11 shows the flowchart describing an iterative process to allocate the appropriate zone and it's relevant pressure equation to each node i. The Newton-Raphson method requires an initial assumption for the pressures at each node. A Hertzian pressure distribution is initially assumed in the conjunction. Once each node is allotted with a relevant pressure equation, Eq. 3.101 is solved to obtain the change in nodal pressures. The pressures are then updated using an under-relaxation factor. This process is continued until convergence is obtained.

3.6 Results

The results of the simulations are shown in this section. Fig. 3.12 shows the pressure curves at three different dimensionless sliding velocities. In all the figures described in this section, the inlet lies to the left of the figure and the outlet to the right. The characteristic pressure spike is seen at the outlet. It is seen that as the dimensionless sliding velocity, U*, is increased the pressure spike amplitude decreases. This implies that the pressure spike amplitude decreases as the sliding increases. The results presented in this section are based on simulation run at a maximum Hertzian pressure of 0.5 GPa. The maximum value of the dimensionless sliding velocity is 0.04. Larger values of the maximum Hertzian pressure and dimensionless sliding velocities are not run because of the introduction of thermal effects at those conditions.

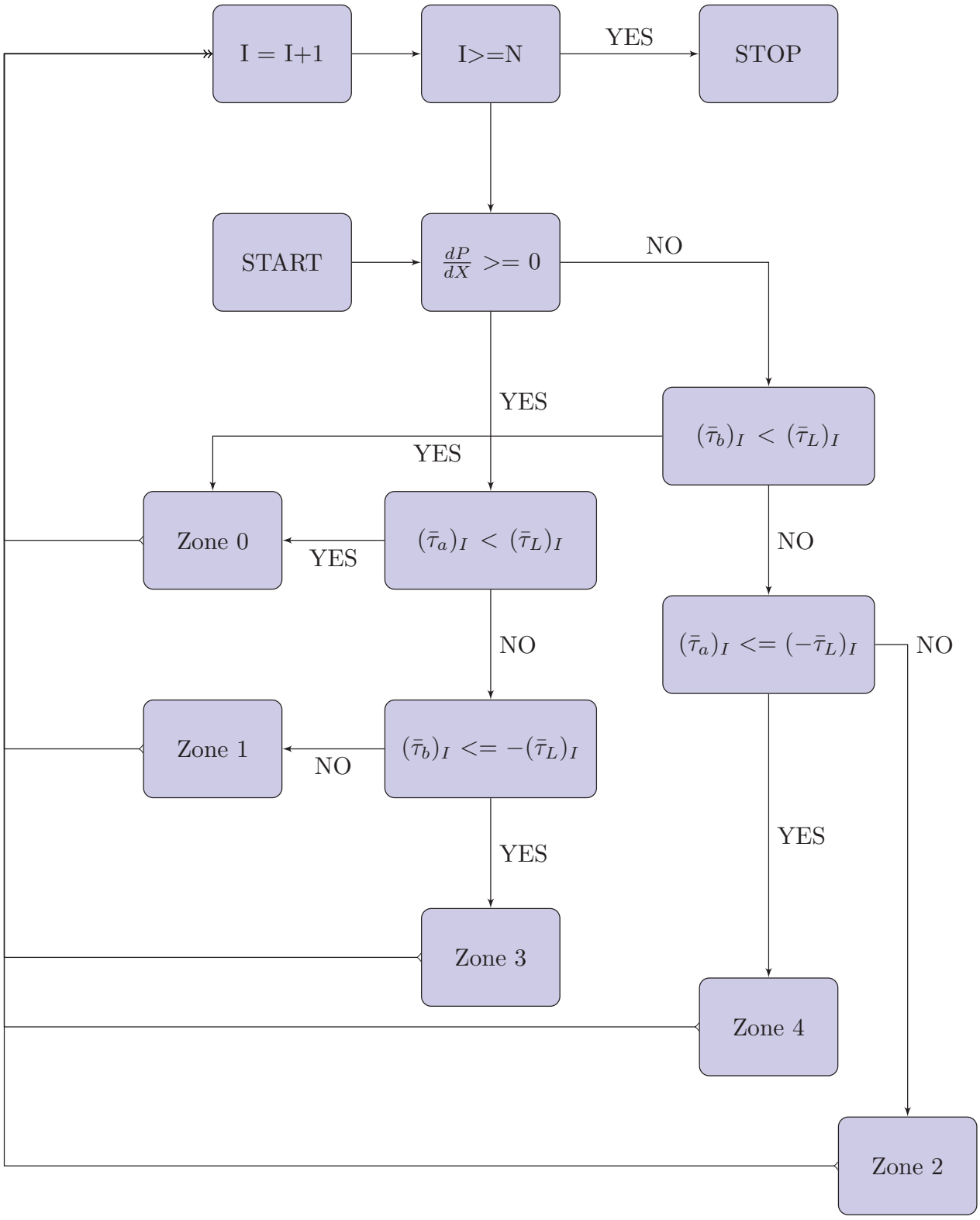

Figure 3.11: Flowchart depicting iterative process [17]

Fig. 3.13 shows the dimensionless film thickness curves at the same operating conditions and varying dimensionless sliding velocities. The figure shows a very minimal difference in the central film thickness at the different dimensionless sliding velocities. Based on these results there appears to be no significant change in the film thickness at relatively low loads and dimensionless sliding velocities.

Fig. 3.14 shows the shear stress ratio (SSR) curves at each surface, for varying dimensionless sliding velocities. The shear stress ratio is defined as:

$$SSR = \frac{\tau}{\tau_L} \tag{3.102}$$

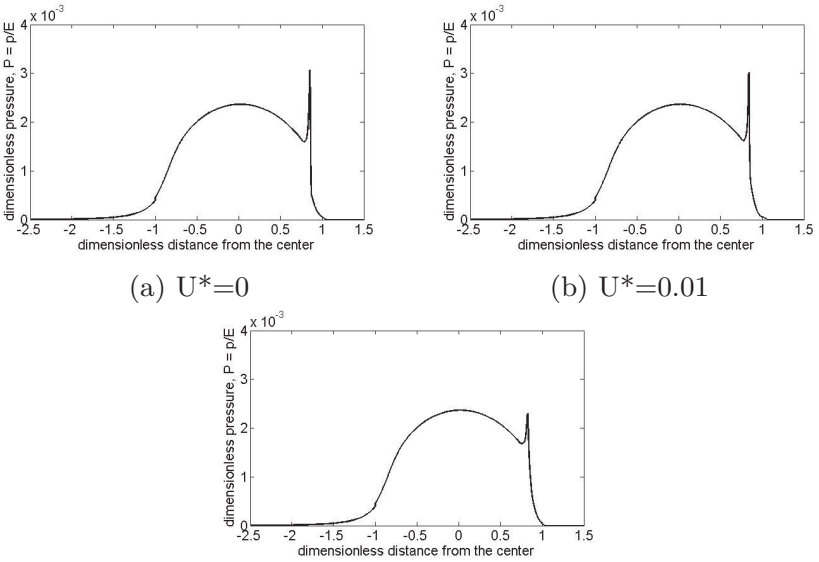

(a) U*=0 (b) U*=0.01

(c) U*=0.04

Figure 3.12: The pressure curves at varying dimensionless sliding velocities. The maximum Hertzian pressure p_h is 0.5GPa. The average inlet velocity u_s is 2m/s.

The SSR curves for the top surface 'a' and the bottom surface 'b' are both plotted in Fig. 3.14. At U* = 0 (pure rolling), all nodes lie with zone 0 and the Newtonian model is valid throughout the conjunction and the SSR at surface a is symmetrical to the SSR at surface b about the x-axis. This can be seen from Eq. 3.46 and Eq. 3.47. The first term on the right hand side is 0 because

of the fact that U* = 0. So the only remaining term is the pressure gradient term on the right hand side. Thus the values of SSR at surfaces a and b are identical but differ in their signs. At U* = 0.01, the spikes at the outlet reside in zone 1 and zone 2, while the rest of the nodes reside in zone 1. At U* = 0.04 there are no nodes in zones 1,2 ,3 or 4. However during the course of the convergence process, some nodes enter zones 3 and 4, before finally entering either zone 0. The effect of the decrease in the pressure spike amplitude with increasing U*, as seen in Fig. 3.12, is seen in Fig. 3.14c. The SSR at surface a becomes significantly less negative with increasing U*.

In the inlet region, the SSR at different sliding velocities are very similar. However a significant change in the SSR at varying U* values can be observed in the Hertzian region. As U* increases, the SRR increases in the Herztian region. These results are in agreement with those produced by [17].

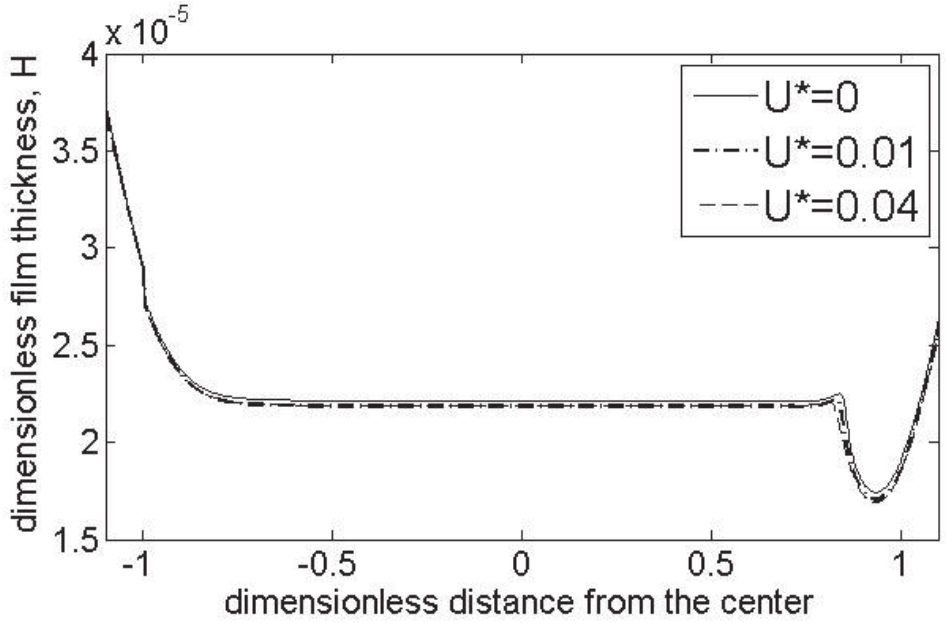

Figure 3.13: Comparing the film thickness at varying dimensionless sliding velocities. The maximum Hertzian pressure p_h is 0.5GPa. The average inlet velocity u_s is 2m/s.

Fig. 3.15 compares the pressure curves at varying average inlet velocities. The average inlet velocity, u_s is defined as

$$u_s = \frac{u_a + u_b}{2} \tag{3.103}$$

Simulations were run for two different values of inlet velocities, 1m/s and 2m/s. Fig. 3.15a compares the pressure curves at U* = 0. Fig. 3.15b compares the pressure curves at U* = 0.04. Both plots show a decrease in the pressure spike amplitude with increasing dimensionless sliding velocity. They also show that the spike is moved closer to the outlet with decreasing inlet velocity. These results are well established and are in concurrence with the analytical solution predicted by [8]. The inlet velocity is known to have a significant effect on the film thickness. A higher inlet velocity is known to cause an increase in the interfacial film thickness. This can be observed in Fig. 3.16a and Fig. 3.16b. Thus it is seen that relatively low levels of sliding does not cause a change to the difference in film thickness values at varying inlet velocities.

Fig. 3.17 compares the SSR curves at varying inlet velocties. At both values of U*, it is observed that the SSR decreases in the Hertzian region and the spike region as the inlet velocity is decreased.

3.7 Conclusions

In this chapter, EHL pressure and film thickness curves are generated using the multigrid method for line contact solution. The characteristic pressure spike and the gap closing at the outlet are observed. The convergence rates of using different relaxation schemes are studied in Publication A. The multigrid model is also useful because it can be extended to study the effect of a single groove on the pressure and film thickness under line contact conditions. This model is constructed in Chapter 5. The results of the multigrid model are also used as an input in studying the fatigue life of rolling element bearings using the Dang Van criterion.

Pressure, film thickness and shear stress curves are generated based on the finite difference model by [17] for low loads and slide-roll ratios. At low SRRs it is observed that there is no significant change in the interfacial pressures at a given load. The limitation of this model is that this model can only be used at low loads and SRRs because this model assumes isothermal conditions. However at higher loads and SRRs, a model that takes into account thermal effects can be built using the multigrid method.

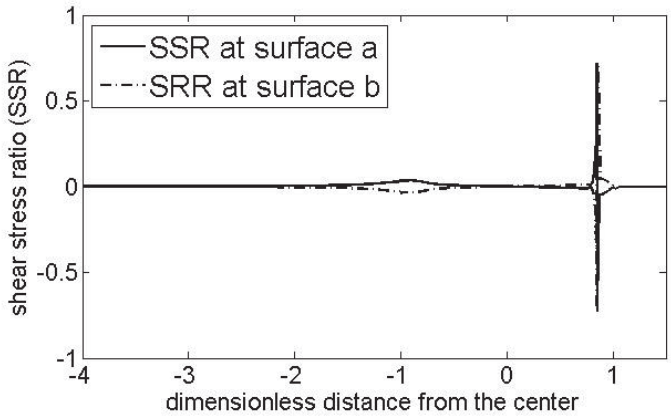

(a) U*=0

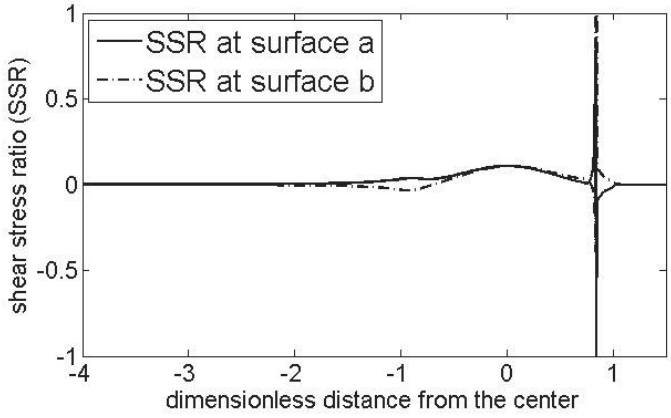

(b) U*=0.01

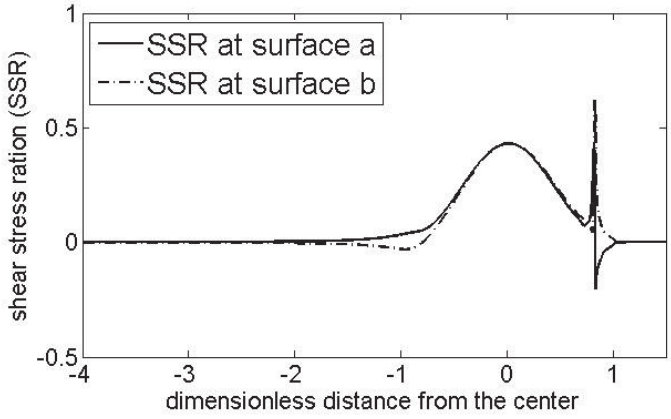

(c) U*=0.04

Figure 3.14: The shear stress ratio curves at varying dimensionless sliding velocities. The maximum Hertzian pressure p_h is 0.5GPa. The average inlet velocity u_s is 2m/s.

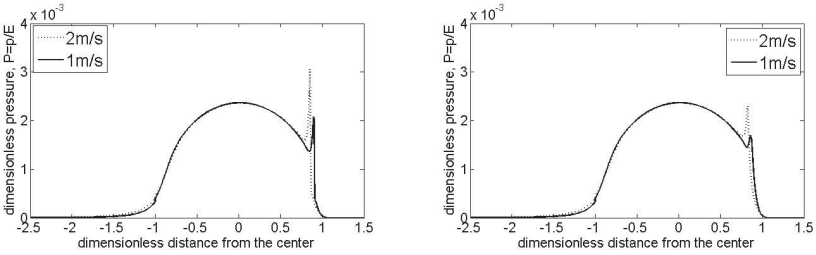

(a) U*=0 (b) U*=0.04

Figure 3.15: Comparing the pressure curves at varying average inlet velocities. The maximum Hertzian pressure p_h is 0.5GPa.

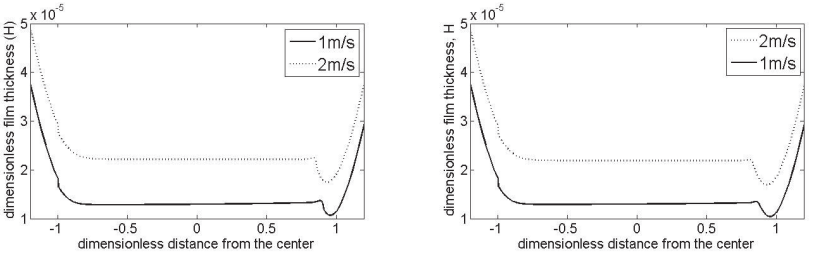

(a) U*=0 (b) U*=0.04

Figure 3.16: Comparing the film thickness curves at varying average inlet velocities. The maximum Hertzian pressure p_h is 0.5GPa.

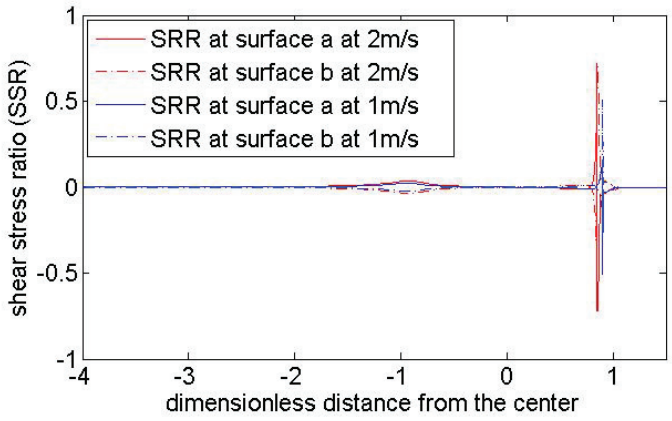

(a) U*=0

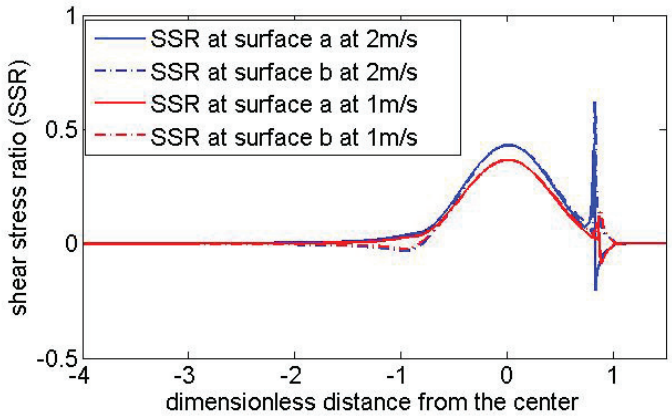

(b) U*=0.04

Figure 3.17: Comparing the SSR curves at varying average inlet velocities. The maximum Hertzian pressure p_h is 0.5GPa.

Chapter 4

Effect of hydrogen on the fatigue failure of bearing steels

4.1 Fatigue failure of bearing steels

Premature fatigue failure of 100Cr6 bearing steels is observed in wind turbine gearboxes. Some rolling element bearings in the wind turbine gearbox do not last for 10% of their expected lifetime [18–20]. Rolling contact fatigue (RCF) of these bearings is characterized by a failure feature known as white etching cracks (WECs). This failure mode is termed white structure flaking (WSF). WSF occurs due to slow subsurface decay under RCF [18]. WECs are enveloped by areas of microstructural change known as white etching areas (WEAs). These areas of microstructural change turn white when etched with 2 % Nital. Hence the name white etching areas.

There have been many reasons put forward for the premature failure of these bearings. However the primary reasons for WSFs are still being investigated. The two main drivers for WSF are suggested to be transient operating conditions [18, 20, 21] and the diffusion of hydrogen into the surface of bearing steels.[21] believed that the slip between the rolling elements and the raceway impacts flaking failure. The hydrogen is assumed to diffuse into the surface of the steel by the decomposition of the lubricant [19, 22–30]. [28] conducted RCF tests on thrust ball bearings.

4.2 Decomposition of lubricant

[28] suspected a primary role of hydrogen in the fatigue failure of these bearings because they observed that the WEAs formed preferentially along former austenite grain boundaries, which served as unstable hydrogen diffusion and trap sites. [28] measured the hydrogen content in the bearing before and after RCF testing. They observed a significant increase in the concentration of hydrogen in the bearing after RCF testing (test stopped after 26 million cycles). [28] postulated that hydrogen from the lubricant diffused into the surface of the bearing during RCF testing. To further confirm these findings, [28] filled an airtight autoclave with a maximum capacity of 177ml with 145 ml of oil at 200 C. The oil was left standing for 200 hours. The gas collected in the container was then measured for hydrogen content. The hydrogen contained in the gas was 1125ppm, while the hydrogen in the undecomposed lubricant was 400ppm. Thus under conditions of high temperature and pressure, [28] noted that the lubricant decomposed, releasing hydrogen. Under RCF conditions for bearings, the released hydrogen can diffuse into the surface of the bearings causing hydrogen embrittlement.

[27] studied the mechanism of hydrogen generation from various types of lubricants by performing sliding tests and measuring the concentration of hydrogen released from the lubricant. Ball on disc sliding tests were conducted in an oil bath. Three balls were fixed and pressed against a steel ring. The ring was then moved relative to the balls causing pure sliding. Since the balls were fixed there was no rolling. A 20 hours sliding tests was conducted and the concentration of hydrogen in the steel ring was measured using a hydrogen analyzer. [27] measured an increase in hydrogen concentration in the steel surface after the sliding tests. [27] also observed that the quantity of hydrogen generated in the sliding tests depended on the lubricity of the lubricant. Lubricity is defined as the reduction in friction and wear by a lubricant. The fact that hydrogen generated was shown to be dependent on the lubricity indicated that the hydrogen generated is increased when the lubricant comes into contact with a fresh steel surface. Fresh steel surfaces are generated when wear occurs, exposing the underlying fresh steel to the lubricant. To further confirm this finding, [27] conducted sliding tests under similar test conditions for a ceramic ball and disc pair and a steel ball and disc pair. The ceramic ball and disc pair simulated an inactive steel surface. [27] observed that the hydrogen generated in the ceramic system was significantly lower compared to the steel system. [27] suggested that the dominant factor for hydrogen generation was the de-

composition of the lubricant by a catalytic reaction with the fresh steel surface.

The results of the tests conducted above prove that hydrogen is generated by the decomposition of the lubricant at temperatures corresponding to those observed in rolling element bearing contacts in wind turbine gearboxes. Thus hydrogen is assumed to be an integral feature in the premature bearing failure and formation of WECs. So RCF tests are conducted on hydrogen diffused 100Cr6 bearing steel rings in this chapter.

4.3 Hydrogen as a WSF driver

The mechanism of hydrogen diffusing into the surface of the steel and causing embrittlement is described in this section. Hydrogen molecules, H_2, are too large to enter into the surface of the steel. However H^+ ions can enter into the steel surface. The disassociation of the hydrogen molecule into it's constituent ions allows for it to enter the steel surface electrochemically or via chemisorption[31]. The hydrogen ions absorbed by the fresh steel surface recombines with electrons in the steel to form atomic hydrogen (Fig. 4.1). Hydrogen has a low solid solubility in iron. Hence most hydrogen atoms are trapped at crystal defects [32].The atomic hydrogen is attracted to grain boundaries, inclusions, microvoids and other regions where crystal defect densities are high [22, 23, 32–34]. The atomic hydrogen exists as an interstitial solute and has a high mobility in high strength steels [35].

[32] used thermal desorption spectroscopy (TDS) results to study the hydrogen trapping sites in steels. The authors used hydrogen as a tracer to study the nature of defects created due to plastic deformation of steels. [32] plastically deformed and annealed various types of steels. Under constant hydrogen charging conditions, they noticed that the hydrogen desorption increased with increasing strain. They postulated that the vacancy clusters annihilate during TDS measurements, thereby releasing hydrogen. When the plastically deformed samples were annealed before being hydrogen charged and studied by the TDS, they observed that hydrogen desorption decreased significantly as the annealing temperature was increased. Based on these findings, [32] concluded that, plastic deformation increases the number of crystal defects in steel. The mobile hydrogen atoms are then attracted to these defects and are released when the defects annihilated during TDS. However when annealing is

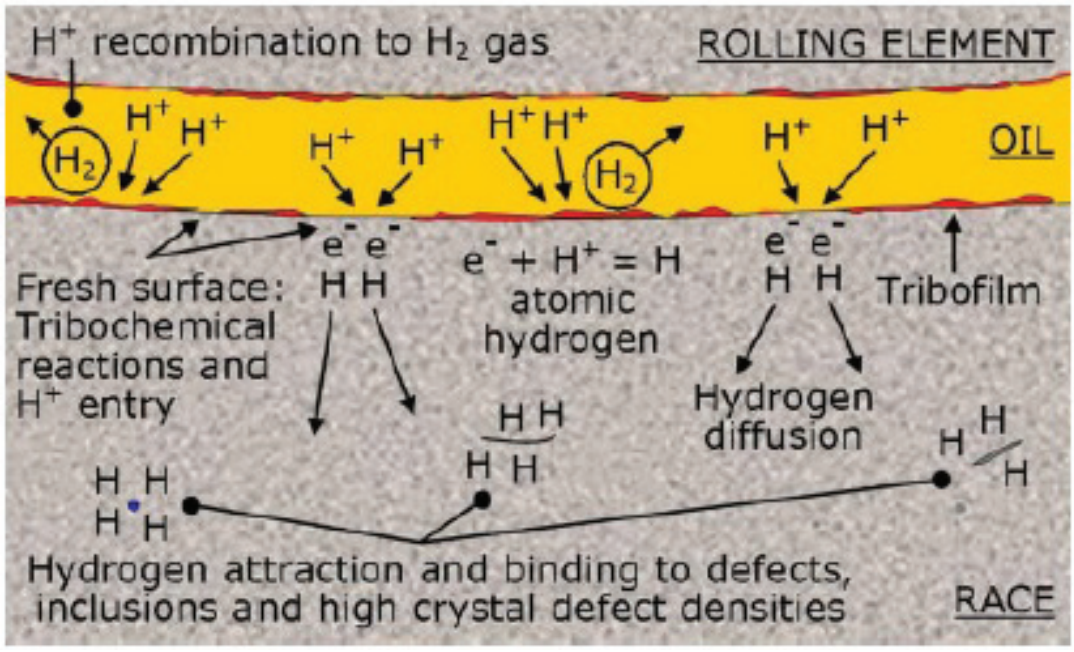

Figure 4.1: Schematic of hydrogen ions from the lubricant combining with electrons in fresh steel surfaces to form atomic hydrogen. Picture from [36]

performed before hydrogen charging, recovery of the plastically deformed structure occurs, thereby reducing these crystal defects. The reduction of defects increases with higher annealing temperatures. Thus when TDS is performed on annealed and hydrogen charged steels, a decrease in hydrogen desorption is observed because of the lack of crystal defects due to annealing. Thus [32] were able to conclude that defects created by plastic deformation act as hydrogen trapping sites.

[37] performed RCF tests on both hydrogen infused and non-hydrogen infused bearings. They concluded that hydrogen strongly accelerates the fatigue crack nucleation and growth mechanism under RCF conditions. [37] used the fact that the vacancies generated due to plastic deformation tend to cluster in different configurations when an interstitial solute like hydrogen is present [38] [39], to make their case for a vacancy-self generating mechanism in the presence of hydrogen. [40][41] suggested that atomic hydrogen interacts with the iron lattice significantly increasing the concentration of vacancies at even lower

temperatures. [37] suggested that the concentration of vacancies is further increased in carbon-containing steels. They noted in an earlier paper that slow damage accumulation with fatigue is controlled by a 'cyclic creep-like damage mechanism' [42]. This climb was controlled by a process known a iron self diffusion. The self diffusion requires the sequential formation of a vacancy and it's subsequent filling by an iron atom. The vacancy-hydrogen pairs in steels are highly mobile and facilitate the iron-self diffusion process. This leads to an acceleration in the damage accumulation rate. As damage is increased, further crystal-defects are created, attracting hydrogen atoms. Thus hydrogen atoms help generate vacancies and accelerate fatigue damage accumulation.

[29] studied the effect of hydrogen on the mode II fatigue crack behaviour in bearing steels. They conducted fatigue tests on hydrogen charged and uncharged samples and subjected them to a cyclic torsion test. In some tests a compressive axial stress was also applied. They observed that the hydrogen charged samples failed significant faster compared to the uncharged samples. Previous research [43–47] showed that hydrogen localized the slip deformation near Mode I crack tips and increased the Mode I fatigue crack growth rate. [29] then showed that hydrogen accelerates Mode II fatigue crack growth. [29] explained the decrease in lifetime of the hydrogen charged samples in a pure cyclic torsion test by noting that hydrogen enhances plastic deformation localization and mode I crack growth rate. They explained the shortened lifetime of charged samples in the cyclic torsion with compressive axial stress by noting the enhanced localization of plastic deformation and the increased mode I and mode II fatigue crack growth rates. Thus hydrogen has been shown to be detrimental to the fatigue life of steels by localizing plastic deformation and accelerating the propagation of Mode I and Mode II fatigue cracks.

The measurement of the concentration of hydrogen in actual bearings in wind turbine gearboxes is a difficult task. Hydrogen diffuses out of the steel surface at room temperature. Most of the hydrogen usually diffuses out in the time taken to dismount the bearing and measure it's hydrogen content in an onshore lab.

4.4 Measurement of hydrogen

As has been mentioned in the previous section, the measurement of hydrogen concentration in steels is an onerous task because the hydrogen diffuses out at

room temperature. Most of the experiments conducted in the laboratory use the TDS method to quantify the concentration of hydrogen in steel after the charging process [18, 29, 37, 48]. The process involves heating the cut sections of the pre-charged steel samples in a vacuum chamber in the TDA equipment. Hydrogen is released, which is then detected using a mass spectrometer.

In the experiments performed by us, as described in this chapter, no quantitative measurement of hydrogen was made as we did not have access to a TDS equipment.

4.5 White Etching Areas

WEAs have been observed in both through hardened martensitic steels [37, 49–52] and bainitic steels[53]. WEAs are composed of equiaxed nano sized ferrite grains 10-100nm in diameter [49, 51, 53–55]. WEAs usually are much harder than the matrix [54]. Cracks surrounded by WEAs on either side are called White Etching Cracks (WECs).

WECs can initiate on the surface or in the sub-surface[36]. The formation of WECs is thought to be caused either by hydrogen embrittlement as described previously or by transient operating conditions [18][20]. [55] suggested that WEAs are formed by a hydrostatic pressure causing the crack faces to close resulting in nanocrystallisation.

4.6 RCF tests

The objectives of conducting RCF tests on the 100Cr6 rings are twofold.
1. Generate WECs by replicating conditions existing in a wind turbine gearbox.
2. Study the effect of two different Hoop stress levels on the fatigue life of the bearing steel.

The bearing material(100Cr6 bearing steel) and the maximum Hertzian pressure (1.65 GPa) applied in the RCF tests are similar to those observed in the wind turbine gearbox. The testing method is briefly described in this section. For a more detailed explanation of the testing process, the reader is referred to Publication C.

The ring is pre-charged with hydrogen by immersing it in a solution of 12 wt.% aqueous ammonium thiocyanate for 24 hours at 50 C. Prior to the hydrogen charging process, the rings are cleaned. Each ring is first cleaned with a clean paper towel. The ring is then immersed in toluene for 4 minutes. It is then taken out and wiped dry with a paper towel. The ring is then immersed in acetone for 4 minutes, taken out and wiped clean.

After the ring is hydrogen charged, it is taken out and wiped dry with a paper towel. It is then cleaned with water and then ethanol.

Once the ring is cleaned, it is mounted onto a shaft. The Hoop stress to be applied on the ring due to the fitting is calculated by measuring the increase in outer diameter of the ring. Once the desired Hoop stress is known, the corresponding outer diameter of the ring can be calculated using Eq. 4.1. Hence the ring is pushed further up the cone, using a hydraulic press, until the required increase in diameter is obtained.

$$\sigma_{\theta\theta(r=r_f)} = \frac{v_d E_h (r_b^2 + r_f^2)}{4 r_f^2 r_b} \tag{4.1}$$

where
v_d is increase in outer ring diameter, E_h the elastic modulus, r_b is the outer radius of the hub and r_f is the fit radius.

The RCF tests are conducted at two values of tensile Hoop stress viz., 440 MPa and 540 MPa. The maximum Hertzian pressure is 1.65 GPa. The lubricant inlet velocity is 20 m/s. The steady state lubricant temperature at the inlet is 35 C. The surface roughness of the the hydrogen charged ring is $R_a = 150$ nm. The RCF tests conducted are pure rolling tests and no sliding is applied.

The RCF tests are continuously run until either of the two rings cracks. When one of the rings fails, a sharp spike in the interfacial torque is observed, a critical torque value is breached and the test-rig is automatically shut off. However in some tests the torque spike is not large enough to breach the critical torque value. In such cases, the rig is manually shut down. In such tests, the lubricant can seep into the crack face of the fractured ring.

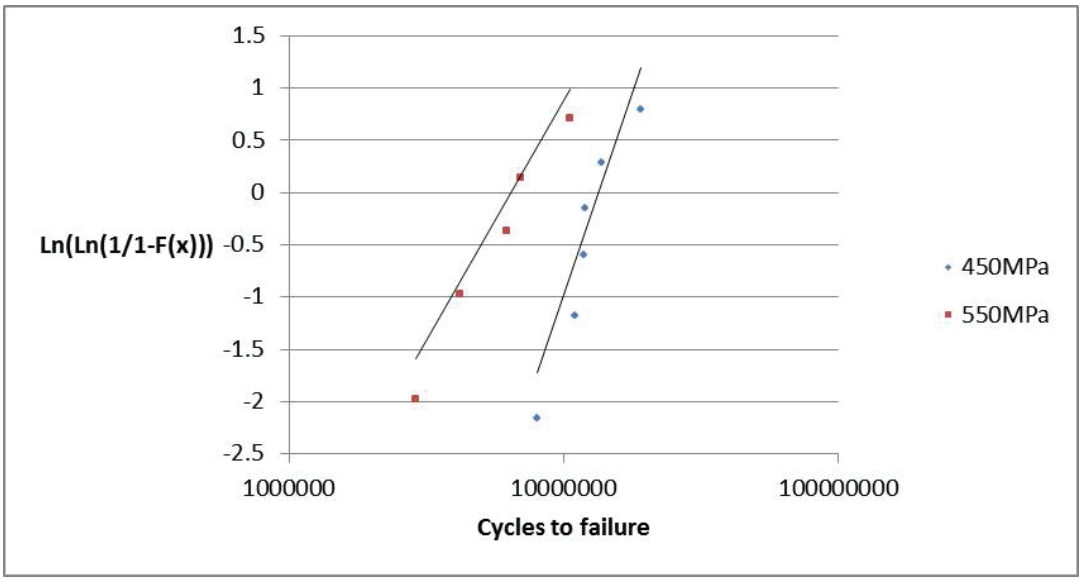

Figure 4.2: Weibull curve showing the effect of two different tensile Hoop stresses on the fatigue life of 100Cr6 steels

4.7 Results of RCF tests

The main results of the RCF tests are encapsulated in this section.

Table 4.1 and Table 4.2 contain the number of cycles to failure for the RCF tests at 440 MPa Hoop stress and 540 MPa Hoop stress respectively. Fig. 4.2 shows the effect of two different tensile Hoop stresses on the RCF life of 100Cr6 steel. Their fatigue life decreases as the tensile Hoop stress in increased. This is because the higher tensile Hoop stress decreases the time for crack initiation. Section 4.8 describes the methodology used to plot the Weibull curve.

After a ring fails, it is sectioned for reflecting light microscopy (RLM). The fracture surface (with plane normal to the circumferential direction) is viewed under a Leica MZ 125 stereo microscope equipped with a Leica DFC450C camera (cooled CCD). Then it is hot mounted, ground and polished to reveal a circumferential cross section just below fracture surface. This cross section is etched with 2% nital and observed under a Olympus CK40M microscope equipped with a Leica DFC450C camera (cooled CCD) to look for WECs. Suspected WECs are investigated with a Phenom ProX Desktop Scanning Electron Microscope (SEM) to confirm their presence and perform detailed investigations

ring number	cycles to failure (millions)	WEC found?
A19-b	8	Yes
A20	19	Yes
B23	11	Yes
B24	11.8	Yes
B26	12	Yes
A27	13.8	Yes

Table 4.1: Number of cycles to failure at 440MPa Hoop stress and charged with 12 wt.% ammonium thiocyanate solution

ring number	cycles to failure (millions)	WEC found?
A26	2.9	No
B28	10.6	Yes
A29	6.2	Yes
B30	4.2	Yes
B33	7.0	Yes

Table 4.2: Number of cycles to failure at 540 MPa Hoop stress and charged with 12 wt.% ammonium thiocyanate solution

of associated WEAs under high magnification. The SEM uses a back scattered electron detector. Additionally it is investigated if WECs are initiated at inclusions by performing Energy Dispersive X-Ray Spectroscopy (EDS) studies. If no WECs are found in the circumferential cross section, axial cross sections, adjacent to the fracture surface, are investigated as well. However no serial sectioning of the rings is performed for microscopy. Since no serial sectioning is performed, WECs only very close to the fracture surface are investigated.

The fractographs of the failed samples revealed WECs in most of the tested rings, as encapsulated in Tables 4.1 and 4.2.

RCF tests are also conducted on uncharged 100Cr6 ring specimens. The ring is pre-stressed with a tensile Hoop stress of 540MPa and a compressive radial stress of 165 MPa. This ring failed after 45 million cycles, which translates to about 2 weeks of actual run time. Fig. 4.6 shows the fracture surface of

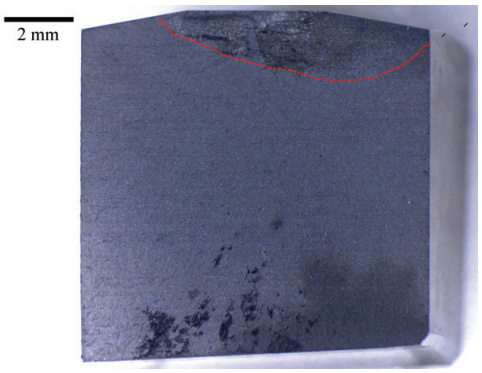

Figure 4.3: The fracture surface of the failed ring A27, when viewed under a stereo microscope. The ring was pre-loaded with a tensile Hoop stress of 440 MPa.

this failed ring, A24. In this figure no clear boundary between the incremental fatigue crack growth region and the rapid crack growth region is observed. Fig. 4.7 and Fig. 4.8 show a magnified image of the crack region in ring A24. Even though this ring required the most number of cycles to failure, no WECs are observed close to the fracture surface. This result seems to suggest that under the current testing conditions, without any slip and hydrogen charging, it is not possible to form WEAs in the failed samples.

More tests on uncharged hydrogen samples are not performed due to the long testing time involved.

Fig. 4.4 and Fig. 4.5 show the WECs observed in a typically failed ring specimen, ring A27. Ring A27 failed after 13.8 million cycles. The ring was pre-stressed with a tensile Hoop stress of 440 MPa and a compressive radial stress of 138 MPa.

Fig. 4.3 shows the fractured surface when viewed under the stereo microscope. The crack appears to have initiated away from the chamfer. The area demarcated by the red boundary indicates the region where incremental fatigue crack propagation occurred. After the incremental fatigue crack grew to a certain critical length, sudden fracture occurs. The region on incremental fatigue crack growth has a grainier appearance compared to the sudden fracture region. The sudden fracture region appears smooth. While the crack initiation appears to

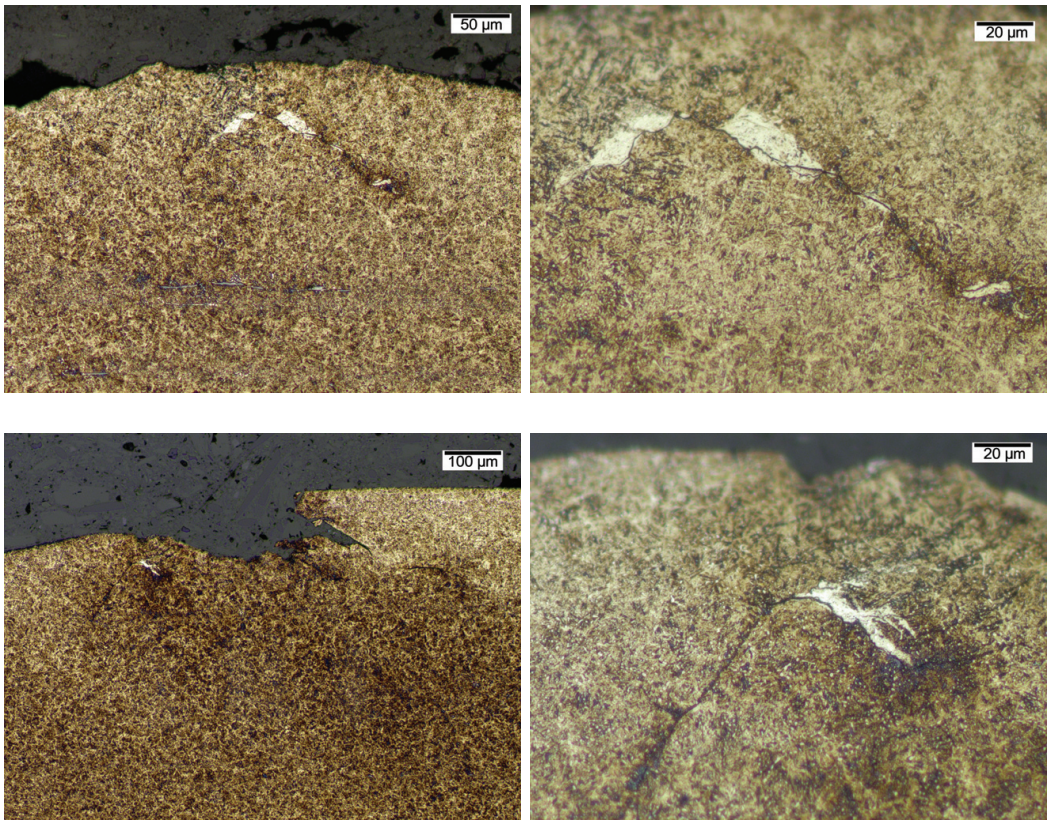

Figure 4.4: WECs observed in the etched circumferential sections of ring A27. The ring was pre-loaded with a tensile Hoop stress of 440 MPa Hoop stress.

have occurred away from the chamfer in this specimen, majority of the other failed rings show a propensity for crack initiation close to or directly below the chamfer.

Fig. 4.4 shows etched circumferential cross sections of the failed ring, close to the fracture surface. WECs are visible upon etching with nital. The WECs are approximately about 50 microns below the running surface. The maximum shear stress is expected to be about 150 microns below the running surface. Hence it is interesting to note the presence of WECs much closer to the surface compared to the expected maximum shear stress depth. This is possible due to the fact that the running surface is not completely smooth as can be seen

in the figure. This ragged running surface introduces local pressure peaks in the lubricant and raises the depth of the maximum shear stress closer to the surface. The concentration of hydrogen also decreases with increasing distance from the running surface. So the presence of local pressure peaks and higher concentrations of hydrogen closer to the running surface lead to WECs being formed closer to the surface compared to the expected depth of the maximum shear stress.

Fig. 4.5 shows the SEM images of the WECs. The SEM images confirm the presence of WECs. The WECs have a much finer grain structure compared to the rest of the matrix. This is consistent with the description on WECs by [49, 51, 53–55].

For a more detailed study on the microstructures of each failed sample, the reader is referred to Publication C .

It is also interesting to note that the ring which failed after the lowest number of cycles, A26, which failed after 2.9 million cycles, did not reveal any WEAs close to the fracture surface. This appears to confirm the findings of [18] that the number of cycles to failure plays a role in the formation of WEAs. This is consistent with the mechanism of WEA formation by [37]. During each cycle, the microstructure adjacent to the crack undergoes severe plastic deformation. Material transfer by a bonding/debonding sequence between the crack faces occur, leading to a deposition of WEA on the receiving side of the crack. This mechanism leads to an incremental increase in WEA on the crack sides with each cycle.

4.8 Weibull Curve

The Weibull Curve is plotted to study the relationship between the percentage of samples failed on the vertical axis and number of cycles to failure on the horizontal axis. The steps to plot the curve are as follows:
1. Arrange the samples in increasing order of number of cycles to failure by assigning a rank(R).
2. A median rank(MR) for each sample is calculated using the formula $MR = \frac{R-0.3}{N+0.4}$
where N is the number of samples.
3.The value for each sample to be plotted on the vertical axis is calculated as

$y = ln(ln(\frac{1}{(1-MR)}))$

Table 4.3 shows the calculation of the vertical axis values for plotting on the Weibull curve. The suffixes 1 and 2 in the column headings refer to the tests conducted at 450 MPa and 540 MPa Hoop stress respectively.

Num1 (million)	R	MR1	ln(ln(1/1-MR1))	Num2 (million)	MR2	ln(ln(1/1-MR2))
8	1	0.109	-2.15	2.9	0.129	-1.97
11	2	0.265	-1.17	4.2	0.314	-0.972
11.8	3	0.421	-0.601	6.2	0.500	-0.366
12	4	0.578	-0.147	7	0.685	0.144
13.8	5	0.734	0.281	10.6	0.870	0.714
19	6	0.890	0.794	N.A.	N.A.	N.A.

Table 4.3: Calculating the vertical axis values for the tests conducted at 450 MPa and 540 MPa Hoop stress

4.9 Conclusions

RCF tests were conducted on hydrogen charged 100Cr6 bearing steel rings. The maximum Hertzian stress applied is 1.65 GPa. The following conclusions are drawn based on the results of the RCF tests.
1.WECs similar to those found in the rolling element bearings in wind turbine gearboxes can be generated using the test-rig.
2.Higher tensile Hoop stress levels lead to a decrease in the RCF life of bearing steels. This is because cracks nucleate faster with increasing tensile Hoop stress.
3.The formation of WECs is dependent on the number of cycles to failure. This is because the microstructural change increases incrementally with each cycle.
4.Under current testing conditions, with no applied slip, it appears that it is not possible to provoke WEA formation in uncharged, failed, 100Cr6 ring samples.

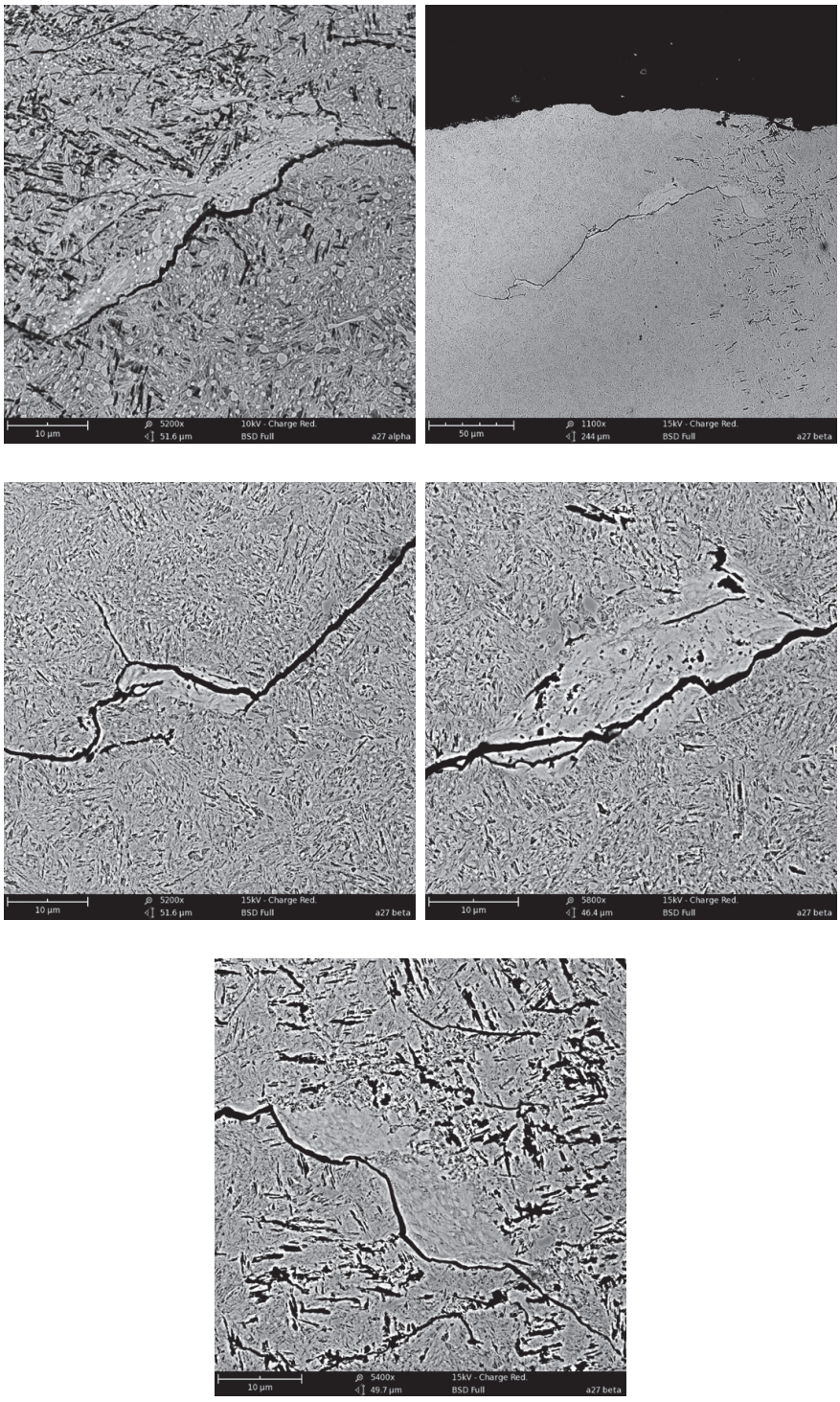

Figure 4.5: SEM images of the WECs in ring A27.The ring was pre-loaded with a tensile Hoop stress of 440MPa Hoop stress.

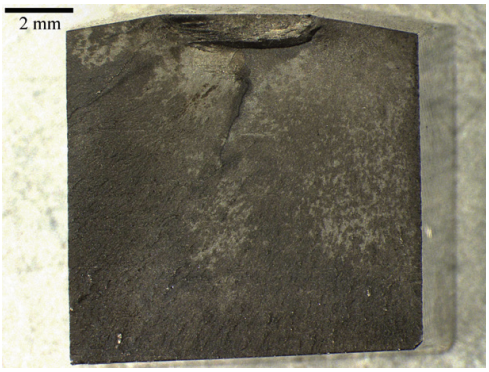

Figure 4.6: Fractography of failed ring A24. A24 was not charged with hydrogen and was pre-stressed with 540MPa tensile Hoop stress

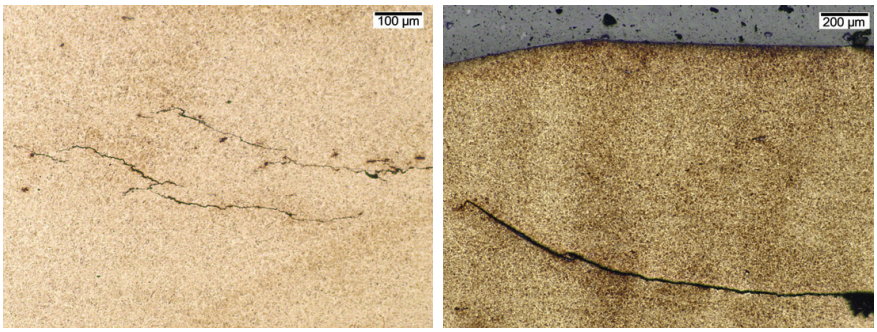

Figure 4.7: Magnified image of crack in ring A24 when viewed under a RLM

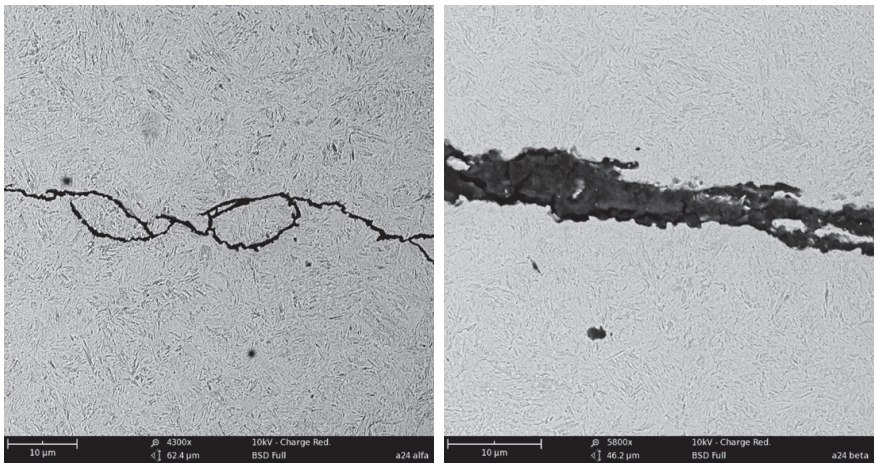

Figure 4.8: SEM images of crack in ring A24

Chapter 5

Surface Texturing and It's Effect on Tribological Properties

5.1 Micro-textures

Surface textures provide an improvement in the tribological features of certain industrial applications under hydrodynamic loading conditions. [56] studied the improved tribological performance of piston rings with surface texturing. [57] investigated the tribological properties of laser-textured mechanical seal faces. [58] suggested that micro sized dimples act as reservoirs of lubricant, which is then transferred to the contact.[59] observed that the roughness in a non-conformal contact produces a film perturbation as it enters the EHL conjunction. However this perturbation moves at a different speed through the conjunction than the roughness feature. So when the smooth surface moves faster than the grooved surface, the lubricant moves at an average velocity of the two surfaces in the junction. Thus the lubricant stored in the groove rushes into the junction increasing the film thickness. The physical phenomena used to explain the positive effects of micro grooves are wear debris entrapment, grooves are lubricant reservoirs and an increase in load carrying capacity due to hydrodynamic effects [60]. However, the positive effects of micro grooves are observed only at optimized geometry (groove dimensions and density)[60] and operating conditions. [60] showed that under pure rolling conditions, there is no significant effect of the groove on film thickness. Under negative SRR, where the grooved surface is slower than the opposing smooth surface, [60] observed that deep cavities (approx. 0.7 microns) reduce the film thickness

compared to two smooth surfaces in contact. A cavity with a depth of 0.4 microns however showed a 30% increase in film thickness at the leading edge of the cavity compared to the smooth surface case. The leading edge of the cavity is that edge of the cavity that enters the contact region first. Thus there exists optimum geometry specifications at which the groove increases the film thickness compared to smooth surface tests. The maximum Hertzian stress applied by [60] is 0.385 GPa.

[60] performed sliding-rolling tests with a ball engraved with a micro-cavity running against a smooth flat surface and observed the transient changes in interfacial film thickness. The slide-roll ratio at which the tests are conducted is 0.5. Studying the film thickness at each stage of micro-cavity motion through the conjunction, [60] observed the following phenomenon. When the cavity just enters the conjunction, a slight decrease in film thickness at the leading edge of the cavity is observed. The pressure in the cavity is still small at this stage so the viscosity of the lubricant is low. As the cavity moves towards the contact center, the pressure is rapidly increased at the inner side of the leading cavity edge. This pressure spike leads to a local increase in lubricant viscosity. When the lubricant viscosity is large enough, the lubricant trapped in the cavity fails to flow along with the rest of the lubricant in the conjunction. This high viscosity lubricant is extracted from the cavity by the applied tangential shear stress. When this lubricant leaves the cavity it elastically deforms the contacting surfaces and the film thickness is increased. As the cavity moves further along the conjunction, the pressure in the cavity drops again. This causes a decrease in viscosity and film thickness and the lubricant leaves the conjunction.

At negative SRRs [60] observed that the local film thickness increase propagates faster than the speed of the cavity. Once the lubricant and cavity leave the conjunction, the surfaces regain their original geometry. [60] concluded that the behaviour of lubricated micro-grooved contacts depends on the groove depth and the ratio of the groove diameter to the contact width.

At shallow groove depths, [60] observed a decrease in the pressure in the groove counterbalancing the pressure spike at the outlet. [60] extrapolated his results to postulate that at a depth of 0.75 microns, the pressure in the groove becomes 0. At low pressures, the lubricant flows into the cavity. When the pressure in the groove is large, piezo-viscous effects occur and the lubricant is dragged out of the cavity by Couette flow. Thus when the pressure in the groove is large

enough, the lubricant is moved from the groove into the interface between the two surfaces and the film thickness is improved. When the depth of the groove increases beyond 0.75 microns (according to [60]), the pressure in the groove is not large enough for Couette flow to be dominant and Poisuelle flow becomes the dominant term moving lubricant into the cavity.

[61] created an artificial dent on the surface of a spherical surface by applying a load on a cone shaped carbide tool. The width of the groove is approximately 100 microns and it's depth is 1 micron. When rolling-sliding tests are performed with the dented surface moving faster than the smooth surface, [61]observed EHL pressures generated in the dent as it passes through the contact. [61] observed that the converging part of the dent increases the pressure and the diverging part reduces the local pressure. Consequently the pressure and film thickness within the dent is reduced, while an increase in film thickness is observed at the trailing edge of the dent. Since the dent moves faster than the average speed of the lubricant, the pressure "tail" as described by [61] trails the dent. [61] observed significant elastic deformation at the trailing edge of the dent thus signifying the presence of large pressures at that edge.
[61] also studied the effect of a single, transverse, shallow groove on the pressure and film thickness under rolling and sliding conditions. The groove was engraved on a polished ball using a wedge shaped tungsten carbide tool. The depth of the groove is maximum at the center and tapers towards the edges. The width of the groove is 20 microns and the depth at the center is 0.5 microns. Phenomena observed in the case of a single dent are also observed with a groove under rolling-sliding conditions. A pressure "tail" lags the groove as seen in the single dent case. The pressure in the groove is reduced. The film thickness experiences an increase at the leading edge of the groove.

5.2 Experimental method

This section describes the experiments performed on grooved ring surfaces to study the tribological behaviour of contacting ring surfaces. The study consists of an experimental portion and a modeling portion, which can explain some of the experimentally observed behaviour. This section summarizes the experimental method briefly. For a more detailed explanation, the reader is referred to Publication D.

The experiments performed in this study aim to study the effect of sub microm-

eter sized grooves on the tribological properties of the interface. The grooved rings are run against a ring with a polished surface (Fig. 5.1). The grooved ring is chamfered while the ring without grooves has no chamfer (Fig. 5.2). The contact is lubricated using a fully synthetic, heavy duty drive train lubricant. The grooves are engraved on the surface of the rings using two well established industrial methods - laser engraving and Electric Discharge Machining (EDM) process.

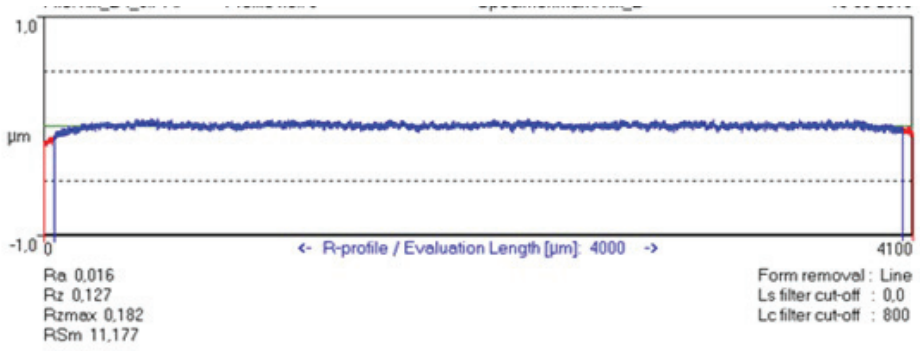

Figure 5.1: The roughness profile of the fully polished unchamfered ring

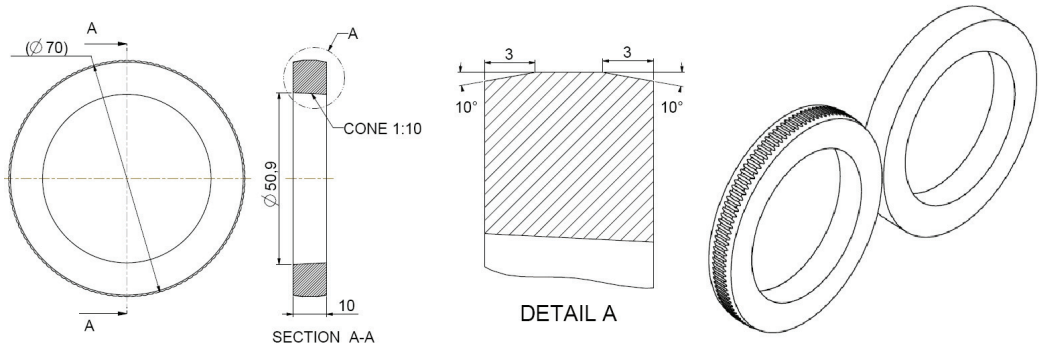

Figure 5.2: Schematic of contact between grooved and smooth ring

Laser engraving process

Grooves of depth 13 μm are engraved on the surface of the chamfered ring by laser engraving (Fig. 5.3). The ring before engraving has a highly polished surface with a roughness R_a of 0.017 μm. The width of each groove is 210 μm. The plateau between two grooves also measures 210 μm. During the design of the experiment, it was intended to create grooves with the smallest possible groove width. Since the manufacturer could engrave grooves with a minimum width of 210 μm, this value was settled upon.

5.2.1 Electric Discharge Machining (EDM) process

Grooves of depth 3 μm and varying wavelengths are engraved on the chamfered rings using the EDM method. Fig. 5.4 shows the groove profile of a ring engraved using the wire EDM process. The different wavelengths engraved are 200 μm, 300 μm, 400 μm and 500 μm.

The process of wire EDM begins with mounting the chamfered ring onto a fixture in the wire EDM machine. The ring is centred using a high precision centring mechanism. A multilayer brass wire is used to cut the surface of the steel ring by melting the steel. The heat required to melt the steel surface is generated when the brass wire comes in contact with the ring. To engrave grooves of shallow depths ($< 5\,\mu$m), the time of contact is set to approximately 1 second. The molten metal solidifies as 'hills' at the edges of the grooves. These 'hill' shaped deposits are flattened by light polishing. The pleateaus between the grooves are fine polished using a rotary polisher. So a highly polished surface is obtained between the grooves on the ring.

5.3 Effect of a single groove under EHL contact

This section describes the results of a multigrid model built to study the effect of varying groove depth under EHL rolling contact conditions. The geometry of the problem involves a single cylindrical grooved surface rolling against a smooth half plane under lubricated conditions. Simulations are run to study the effect of groove depth on the interfacial pressure in the lubricated EHL contact.
Fig. 5.5a shows the groove texture comparing the grooves of 1 μm and 3 μm depth. Fig. 5.5b shows the smooth surface vs grooved surface film thickness.

This figure shows that there is no significant change in the film thickness in the plateau regions of the grooved ring compared to a smooth surface. There is a small decrease in the film thickness around the inlet edge of the groove. The inlet side lies to the left of the figure. These results prove that there is no significant change in the film thickness when comparing the grooved surface to the smooth surface.

Fig. 5.6 shows the pressure and film thickness curves at varying groove depths. Fig. 5.6a shows the increase in interfacial pressure at the inlet and outlet edges of the grooves. Fig. 5.6b shows that there is negligible change in the central film thickness with increasing groove depth. This result combined with Fig. 5.5b shows that there is no significant change in the film thickness along the plateaus compared to the smooth surface film thickness. These results together are used to explain the increase in interfacial torque with increasing groove depth in the following section. Since the change in film thickness is negligible, but the pressures and pressure gradients are significantly increased at the entrance and exit of these grooves, an increase in interfacial torque is observed based on the following two equations.

$$\tau = \frac{h}{2}\frac{dp}{dx} + \frac{(u_a - u_b)\eta}{h} \tag{5.1}$$

where
τ is the interfacial shear stress at the top surface
h is the film thickness
p is the pressure
u_a and u_b are the top and bottom surface velocities respectively
η is the lubricant viscosity

$$\bar{\tau_L} = \bar{\tau_0} + \gamma P \tag{5.2}$$

where
$\bar{\tau_L}$ is the dimensionless limiting shear strength of the lubricant
$\bar{\tau_0}$ is the dimensionless initial shear strength
γ is the limiting shear strength proportionality constant
P is the dimensionless pressure

Eq. 5.1 describes the shear stress in the Newtonian region and Eq. 5.2 describes the shear stress in the Non-Newtonian region [17]. Eq. 5.1 shows that an increase in pressure gradient leads to an increase in the interfacial shear stress (torque), while Eq. 5.2 shows that an increase in pressure leads to an increase in the interfacial shear stress.

5.4 Experimental tests on the grooves rings

This section briefly describes the tests and results of the grooved rings against smooth rings rolling contact tests. For a more complete study of the tests and the associated results, the reader is referred to Publication D. All the tests described in this section are lubricated rolling-sliding contact tests. The interfacial torque is measured in each case using a torque transducer attached to one of the motors.

Tests are conducted on the laser engraved ring to study the effect of increased groove depth on the interfacial torque. It is observed that at a given load, inlet velocity and wavelength, increasing groove depth increases the interfacial torque (Fig. 5.7). This is explained using the results of the multigrid model described in the previous section.
At a given load, inlet velocity and positive SRR, there is no significant change in the torque with varying wavelength (Fig. 5.8).
At negative SRR values, there is no significant increase in the torque with decreasing inlet velocities (Fig. 5.9). This result is counter-intuitive because as the inlet velocity decreases, it is expected that the film thickness would decrease, thereby increasing the torque. This result needs to be examined further and the reason for such a behaviour assessed. At positive SRR values, the curves corresponding to the highest inlet velocity exhibit the lowest torque (Fig. 5.10). This behaviour is expected because of the increase in film thickness with increase in inlet velocity. The increase in film thickness causes a decrease in the torque. The results of the experimental tests show that grooves appear to be beneficial at certain optimum operating conditions. But these results are few and far in between to observed any kind of trend in the results.

5.5 Conclusions

The performance of axial grooves under EHL loads and lubricated, rolling contact conditions has been studied in this chapter. It was intended to increase the

interfacial film thickness by using these grooves as lubricant reservoirs. This phenomenon had been shown to work under certain optimum operating conditions and lower loads. But it had not been studied at EHL loads. Grooves were engraved using currently available industrial methods - laser engraving and EDM. The results of the tests showed that there appears to be no improvement in the tribological performance of the system under EHL loading. There is a possibility that the tribological performance might increase under certain optimum conditions, but it is hard to ascertain what those conditions might be. The tribological performance might also improve if grooves of depth lesser than $1\,\mu$m were able to be engraved. However, this is an extremely expensive process compared to the wire engraving and EDM processes, by which one cannot engrave such shallow depths.

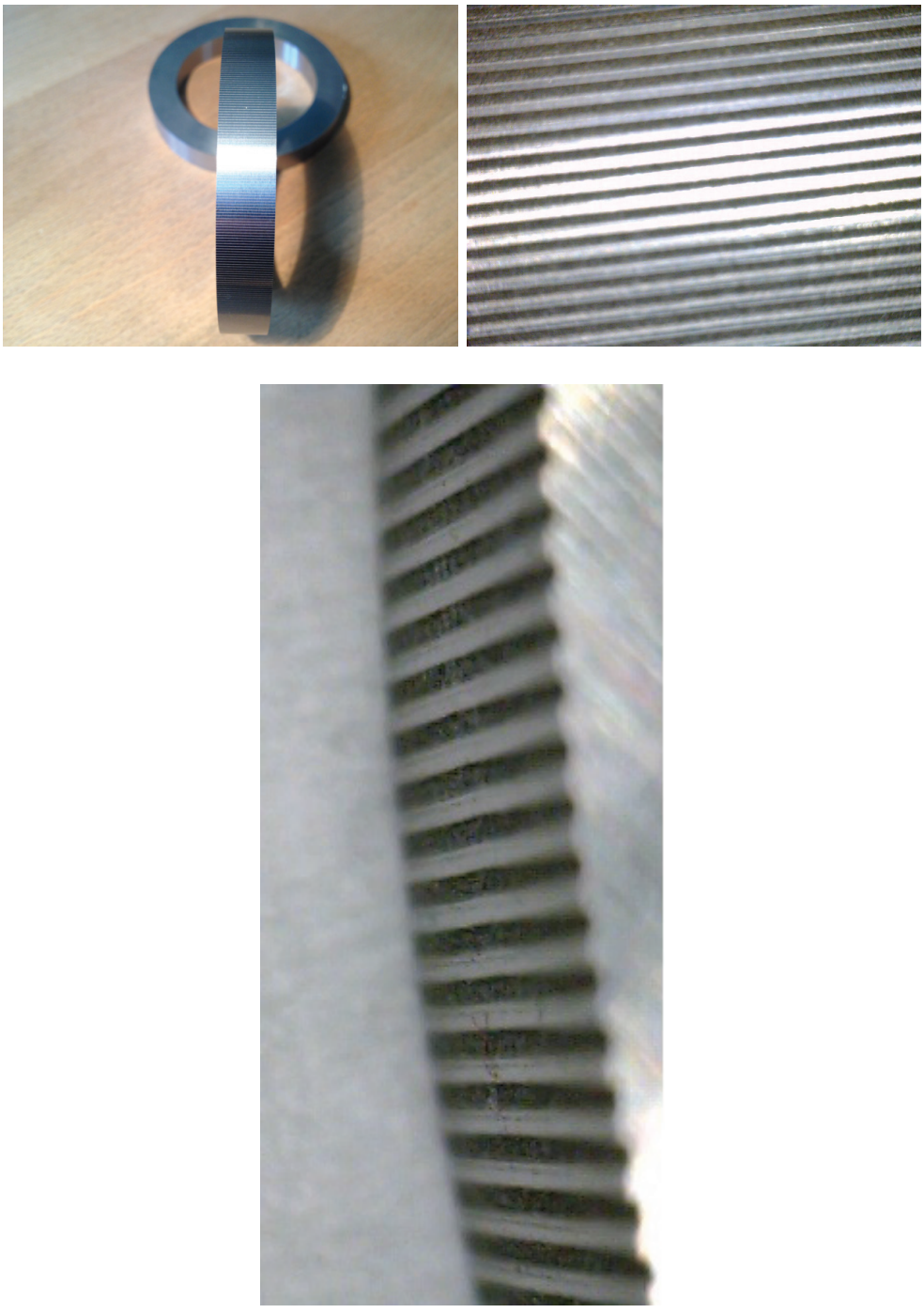

Figure 5.3: The grooves engraved on the surface on a steel ring using the laser engraving process

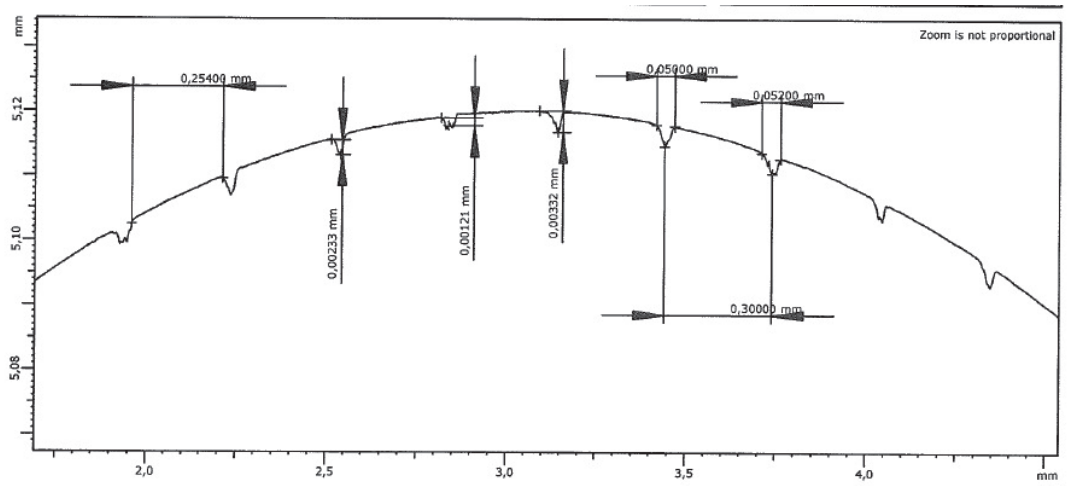

Figure 5.4: Groove profile with wavelength 3 mm engraved using the EDM process

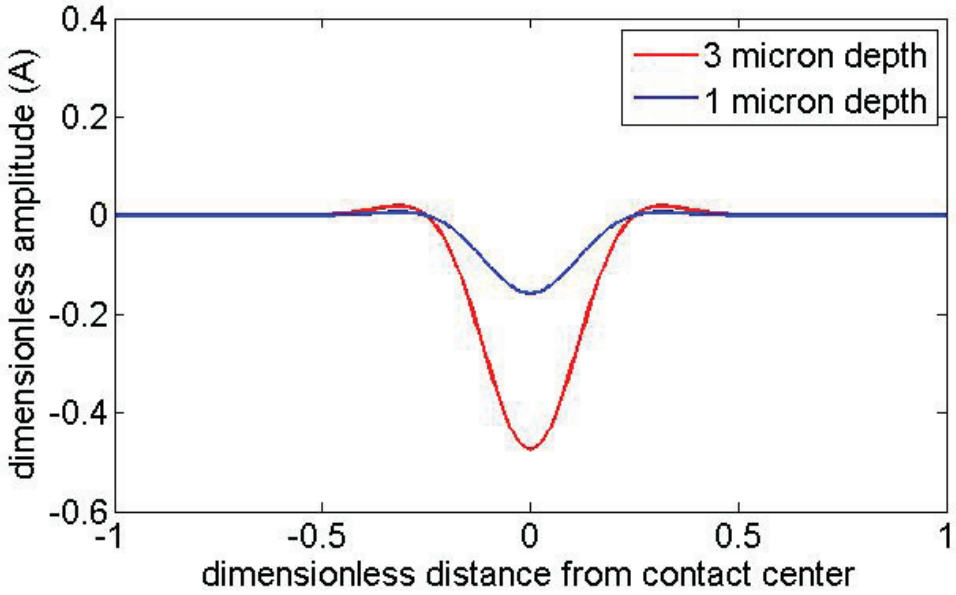

(a) Groove texture

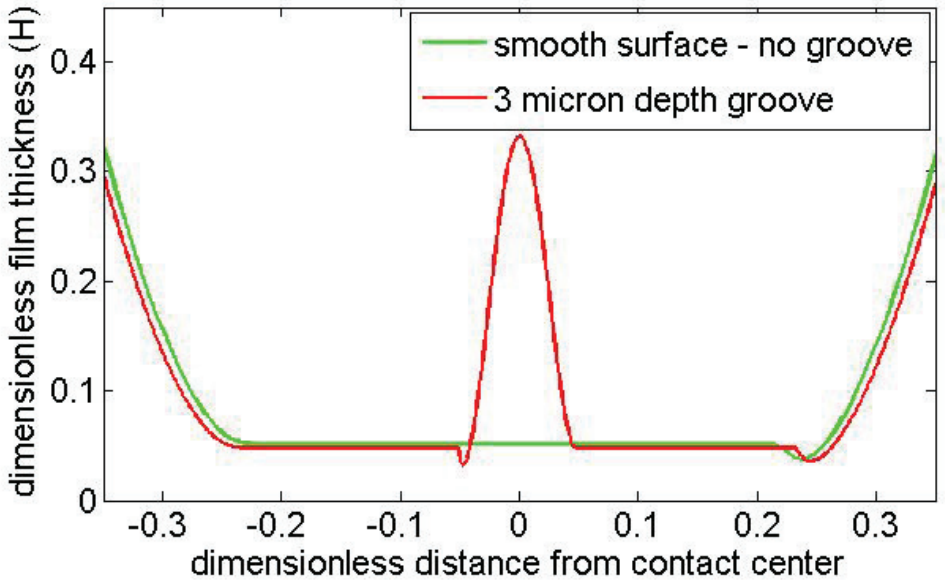

(b) smooth surface vs grooved surface film thickness

Figure 5.5: Single groove texture and comparison of the film thickness between a grooved surface and a smooth surface. The inlet velocity is 1 m/s. The effective elastic modulus is 2.1×10^{11} Pa. The lubricant's viscosity at zero pressure is 0.03 Pa s. The dimensionless load, w is 1 42 x 10^{-4}. The wavelength of each groove equals the Herztian contact half-width.

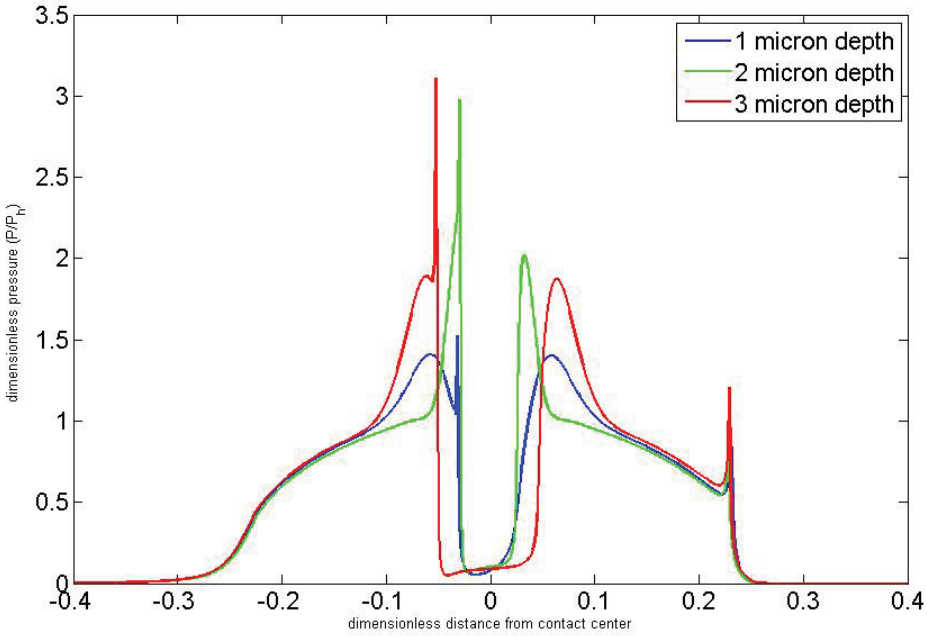

(a) Pressure curves for varying grove depth

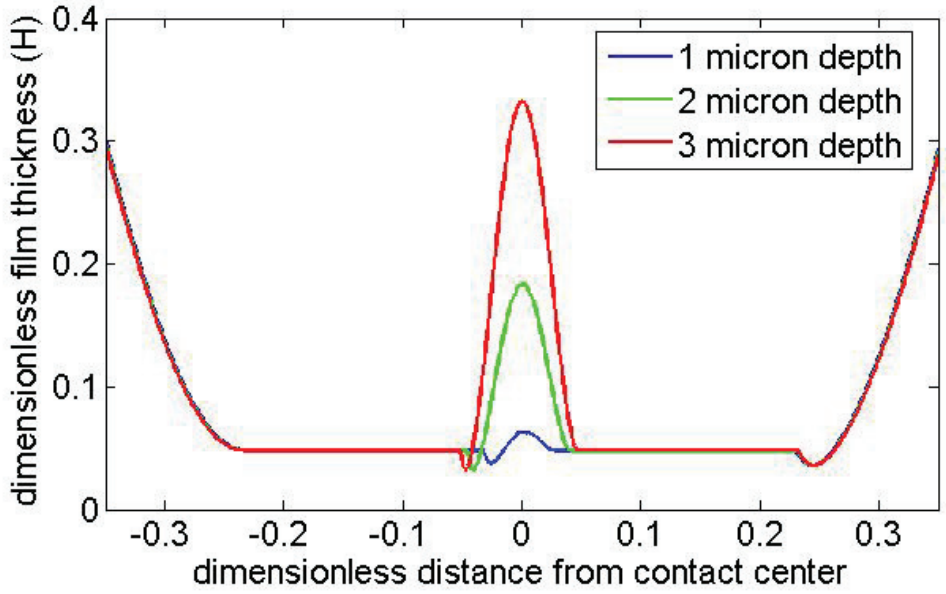

(b) Film thikcness curves for varying groove depth

Figure 5.6: Pressure and film thickness curves at varying groove depths. The inlet velocity is 1 m/s. The effective elastic modulus is 2.1×10^{11} Pa. The lubricant's viscosity at zero pressure is 0.03 Pa s. The dimensionless load, w is 1 42e−4.

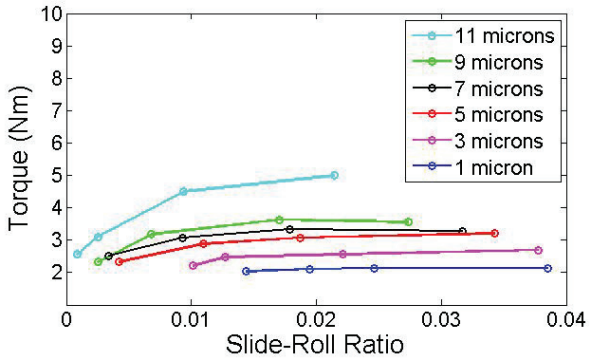

(a) Max. Hertzian pressure 0.95 GPa

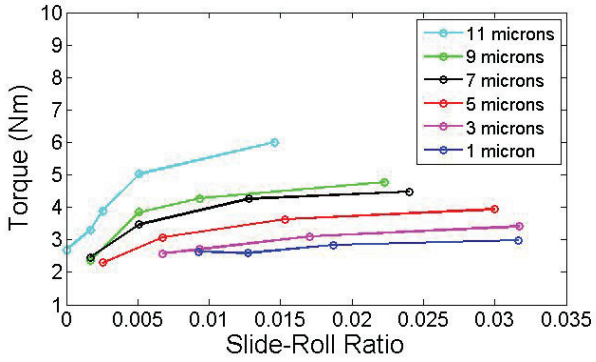

(b) Max. Hertzian pressure 1.07 GPa

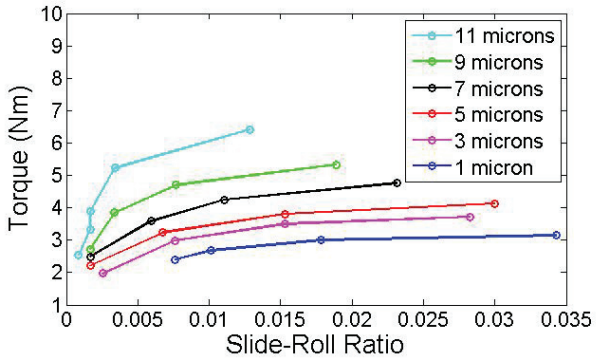

(c) Max. Hertzian pressure 1.11 GPa

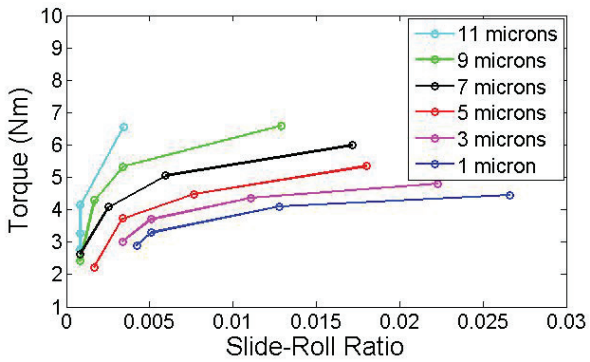

(d) Max. Hertzian pressure 1.20 GPa

Figure 5.7: Effect of varying groove depth on the interfacial torque on a grooved ring with an inlet speed of 8.792 m/s at a given load and positive SRR.

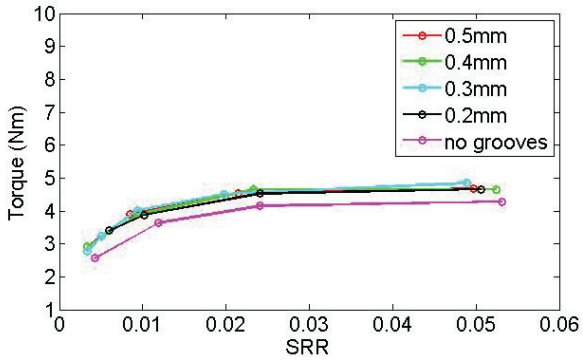

(a) Max. Hertzian pressure 1.1 GPa

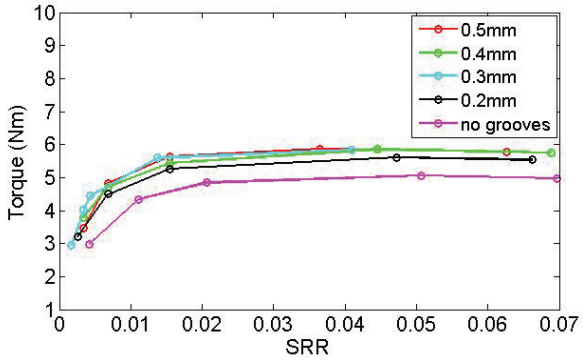

(b) Max. Hertzian pressure 1.2 GPa

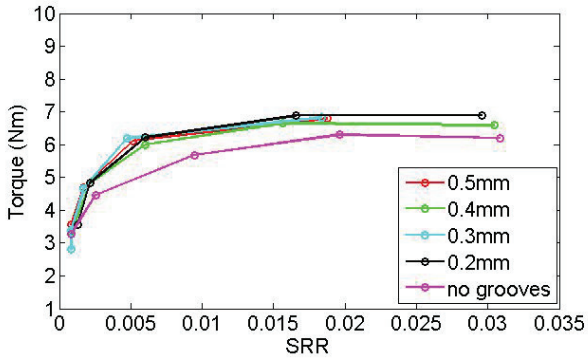

(c) Max. Hertzian pressure 1.4 GPa

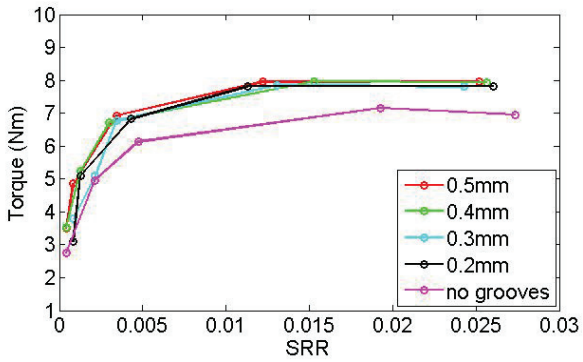

(d) Max. Hertzian pressure 1.45 GPa

Figure 5.8: Effect of varying wavelength on the interfacial torque on a grooved ring with an inlet speed of 8.792 m/s at a given load and positive SRR.

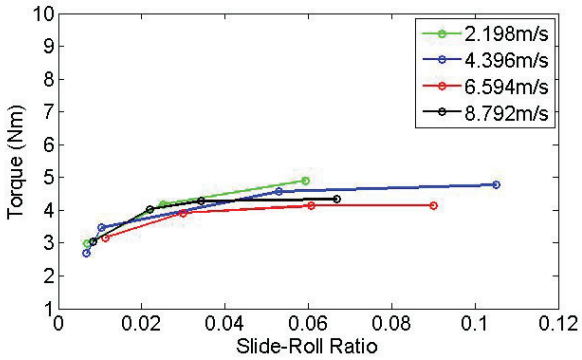

(a) Max. Hertzian pressure 1.1 GPa

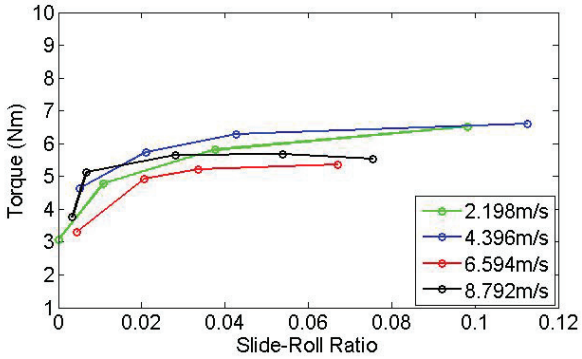

(b) Max. Hertzian pressure 1.2 GPa

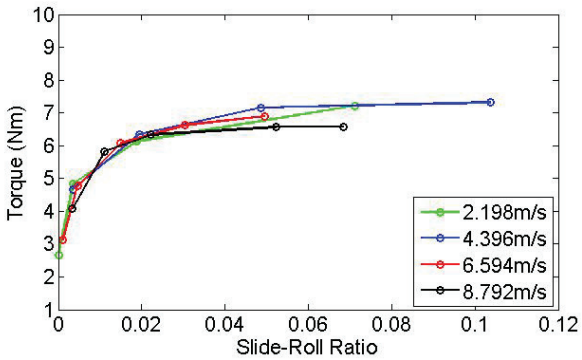

(c) Max. Hertzian pressure 1.4 GPa

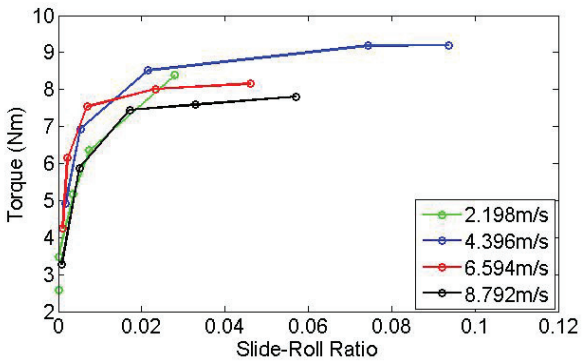

(d) Max. Hertzian pressure 1.45 GPa

Figure 5.9: Effect of varying inlet velocities on the interfacial torque on a grooved ring with wavelength 0.25 mm at a given load and negative SRR.

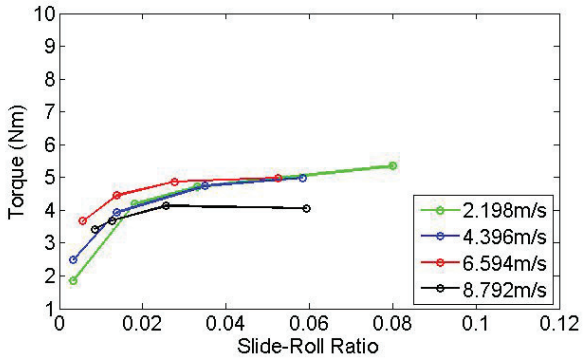

(a) Max. Hertzian pressure 1.1 GPa

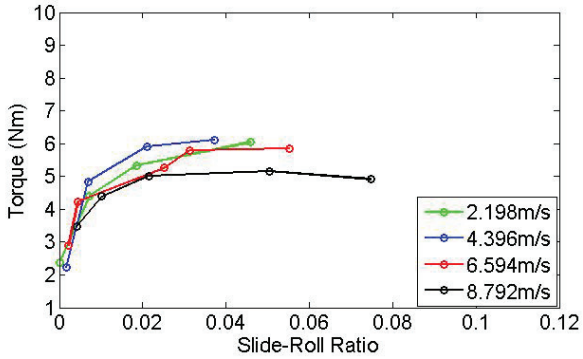

(b) Max. Hertzian pressure 1.2 GPa

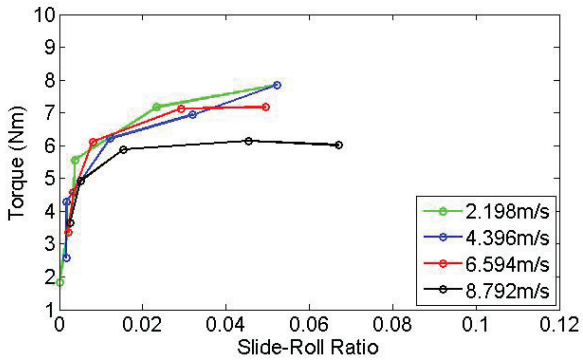

(c) Max. Hertzian pressure 1.4 GPa

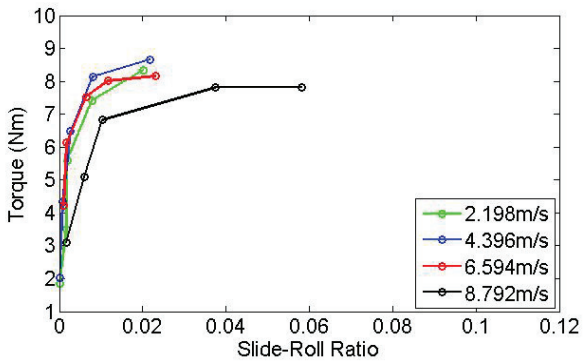

(d) Max. Hertzian pressure 1.45 GPa

Figure 5.10: Effect of varying inlet velocities on the interfacial torque on a grooved ring with wavelength 0.25 mm at a given load and positive SRR.

Chapter 6

Conclusions

Rolling Contact Fatigue tests and tribology tests on grooved rings have been performed to study the behaviour of rolling element bearings in wind turbine gearboxes. Finite Difference models and multigrid models have also been built to support the findings of the experimental results. The conclusions made from these studies are encapsulated below.

Rolling Contact Fatigue tests were conducted on bearing steel rings, with testing condition mimicking actual service conditions as much as possible. A test rig was built to conduct these RCF tests. It was concluded after running these tests that, WECs similar to those seen in actual bearings from service, can be generated using this test rig. An increase in tensile Hoop stress, decreases the fatigue life of the rings. The microstructural changes, associated with the formation of WECs, increases incrementally with each cycle. No WEC formation was seen in the failed ring that was not charged with hydrogen. This seems to suggest that hydrogen is a key driver in WEC formation. More uncharged rings need to be RCF tested to obtain a better understanding of the effect of hydrogen in WEC formation. More uncharged RCF tests were not conducted in this study due to the prolonged failure times for uncharged rings. In the future, more fatigue tests on uncharged samples need to be performed. Compressive residual stresses can also be introduced into the rings by processes like nitriding and it's effect on the fatigue life can be studied.

Interfacial pressure and film thickness curves have been generated using the multigrid method, for EHL line contact conditions between two smooth sur-

faces. This simulates a line contact between the rollers and the inner ring of a bearings. The results of these simulations are used as input loads to predict the fatigue life of these rings using the Dang Van criterion. These results have also been extended to study the contact between a single groove and a smooth surface. These results show that tribological performance improves with decreasing groove depth. Pressure, film thickness and shear stress curves have been calculated using the Newton-Raphson method. A limitation of this model is that the values of pressure, film thickness and shear stress can only be predicted at low loads and slide-roll ratios (SRRs). This is because the current model cannot account for large changes in temperature associated with large loads and SRRs. In the future multigrid models should be built to study the shear stresses are higher loads and SRRs.

It has been previously demonstrated that transverse grooves act as reservoirs of lubricant and improve the interfacial film thickness under low loading conditions. The effect of these grooves under EHL conditions is studied in this project. The grooves were engraved using two currently available industrial methods - laser engraving and EDM. Sub micrometer depth grooves are however not possible to be engraved using either of these methods. The experiments performed show that there is no improvement in tribological performance using these grooves under EHL loading. There may be optimum operating conditions at which these grooves will be useful, but it is difficult to ascertain what those conditions are. In the future, sub micrometer depth grooves should be engraved on rings to study their tribological performance.

Efforts have been made, as part of this thesis, to study the failure of the main bearings in a wind turbine. A better understanding of the processes related to the fatigue failure of these bearings has been achieved. However, more research needs to be performed to improve the lifetime of these bearings and reduce the primary source of losses to the wind turbine manufacturers.

Chapter 7

Appendix A

This chapter provides the necessary equations to calculate the nodal elastic deformations.

The mesh is divided into multiple intervals of $[X_{j-1}, X_{j+1}]$. The nodal deformation at node i is the sum of the individual deformations $d\bar{\delta}_{i,j}$at i caused due to a pressure at node j.

$$\bar{\delta}_i = \sum_{j=2,4,\ldots}^{N-1} d\bar{\delta}_{i,j} \tag{7.1}$$

[2] expressed $d\bar{\delta}_{i,j}$ as

$$d\bar{\delta}_{i,j} = dD_{i,j-1}P_{j-1} + dD_{i,j}P_j + dD_{i,+-1}P_{j+1} + Constant \tag{7.2}$$

with

$$dD_{i,j-1} = -\frac{1}{2\pi}\left(a_1 K + a_2 \frac{M}{2}\right) \tag{7.3}$$

$$dD_{i,j} = -\frac{1}{2\pi}\left(a_3 K + a_4 \frac{M}{2}\right) \tag{7.4}$$

$$dD_{i,j+1} = -\frac{1}{2\pi}\left(a_5 K + a_6 \frac{M}{2}\right) \tag{7.5}$$

where the variables are defined as

$$d_1 = (X_{j-1} - X_j)(X_{j-1} - X_{j+1}) \tag{7.6}$$

$$a_1 = \frac{2}{d_1} \tag{7.7}$$

$$a_2 = -\frac{(X_j + X_{j+1})}{d_1} + a_1 X_j \tag{7.8}$$

$$d_2 = (X_j - X_{j-1})(X_j - X_{j+1}) \tag{7.9}$$

$$a_3 = \frac{2}{d_2} \tag{7.10}$$

$$a_4 = -\frac{(X_{j+1} + X_{j-1})}{d_2} + a_3 X_j \tag{7.11}$$

$$d_3 = (X_{j+1} - X_{j-1})(X_{j+1} - X_j) \tag{7.12}$$

$$a_5 = \frac{2}{d_3} \tag{7.13}$$

$$a_6 = -\frac{(X_j + X_{j-1})}{d_3} + a_5 X_j \tag{7.14}$$

$$Z = X_i - X_j - X' \tag{7.15}$$

$$Z_{min} = X_i - X_{j-1} \tag{7.16}$$

$$Z_{max} = X_i - X_{j+1} \tag{7.17}$$

$$M = Z_{min}^2 (lnZ_{min}^2 - 3) - Z_{max}^2 (lnZ_{max}^2 - 3) \tag{7.18}$$

$$N = Z_{max}^3 (ln|Z_{max}|3 - 4) - Z_{min}^3 (ln|Z_{min}|^3 - 4) \tag{7.19}$$

$$K = M\left(\frac{X_i - X_j}{2}\right) + \frac{2N}{9} \tag{7.20}$$

Having calculated the individual deformations $d\bar{\delta}_{i,j}$, we can now sum them to calculate the deformation at a node i due to pressures at node j

$$\bar{\delta}_i = \sum_{j=2,4,\ldots}^{N-1} d\bar{\delta}_{i,j} \tag{7.21}$$

$$\sum_{j=1}^{N} D_{i,j} P_j - \frac{1}{4} ln\left(R_x^2 \frac{8W}{\pi}\right) \tag{7.22}$$

$D_{i,j} = dD_{i,j}$ if j is even. If j is odd, for instance j = 3, then $D_{i,3}$ is the sum of $dD_{i,3}$ from the interval $[X_1, X_3]$ and $dD_{i,3}$ from the interval $[X_3, X_5]$. The first and last values of $D_{i,j}$ are

$$D_{i,1} = dD_{i,1} \tag{7.23}$$

$$D_{i,N} = dD_{i,N} \tag{7.24}$$

Chapter 8

Appendix B

For a mesh with varying element lengths, the pressure P in the interval $[X_{j-1}, X_{j+1}]$ can be described by the following second degree polynomial

$$P = \frac{X'(X' + X_j - X_{j+1})}{(X_{j-1} - X_j)(X_{j-1} - X_{j+1})} P_{j-1} + \frac{(X' + X_j - X_{j-1})(X' + X_j - X_{j+1})}{(X_j - X_{j-1})(X_j - X_{j+1})} P_j + \frac{X'(X' + X_j - X_{j-1})}{(X_{j+1} - X_{j-1})(X_{j+1} - X_j)} P_{j+1} \quad (8.1)$$

We now define coefficients $dC_{j,j-1}, dC_{j,j}$ and $dC_{j,j+1}$

$$[K_e] = \int_{X'_{min}}^{X'_{max}} P \, dX' = dC_{j,j-1} P_{j-1} + dC_{j,j} P_j + dC_{j,j+1} P_{j+1} \quad (8.2)$$

$$X'_{min} = (X_{j-1} - X_j) \quad (8.3)$$

$$X'_{max} = (X_{j+1} - X_j) \quad (8.4)$$

$$dC_{j,j-1} = \frac{1}{(X_{j-1} - X_j)(X_{j-1} - X_{j+1})} \left| \frac{(X')^3}{3} + (X_j - X_{j+1}) \frac{(X')^2}{2} \right|_{X'min}^{X'max} \quad (8.5)$$

$$dC_{j,j} = \frac{1}{(X_j - X_{j-1})(X_j - X_{j+1})} \left| \frac{(X')^3}{3} + (2X_j - X_{j-1}) \frac{(X')^2}{2} + (X_j - X_{j-1})(X_j - X_{j+1}) X' \right|_{X'min}^{X'max} \quad (8.6)$$

$$dC_{j,j+1} = \frac{1}{(X_{j+1} - X_{j-1})(X_{j+1} - X_j)} \left| (X_j - X_{j-1}) \frac{(X')^2}{2} \right|_{X'min}^{X'max} \tag{8.7}$$

If j is even, the C_j is defined as:

$$C_j = dC_{j,j} \tag{8.8}$$

If j is odd (for example j = 3), then j is defined as

$$C_3 = dC_{2,3} + dC_{4,3} \tag{8.9}$$

$dC_{2,3}$ is calculated in the interval $[X_1, X_3]$ and $dC_{4,3}$ is calculated in the interval $[X_3, X_5]$

Publication A

Comparing the Gauss-Seidel and Jacobi relaxation schemes in the solution of the EHL line contact problem using a multigrid solver.
Presented at the 16th Nordic Symposium on Tribology - NORDTRIB 2014.

Comparing the Gauss-Seidel and Jacobi Relaxation Schemes in the Solution of the EHL Line Contact Problem Using a Multigrid solver

S. Janakiraman[1]*, P. Klit[1]

[1]Technical University of Denmark, Nils Koppels Alle, bld. 404, 2800 Kgs. Lyngby, Denmark.

Abstract

The solution to the EHL line contact problem has been computed by building a multigrid solver. There are two types of relaxation schemes used in the solver, a Gauss -Seidel scheme and a combination of the Gauss-Seidel scheme and the Distributive Jacobi scheme. The differences in the convergence and residual norm values for each of the schemes is discussed.

Keywords: Multigrid, Jacobi, Gauss-Seidel.

*Corresponding author: Shravan Janakiraman (shja@mek.dtu.dk).

1. INTRODUCTION

Lubrecht[1] first solved the line and point contact EHL problem using a multigrid solution using a discretization based on the reduced pressure. Venner[2] then improved upon the solution to the EHL problem without using a reduced pressure approach. Venner also arrived at the solution using a combination of the Gauss-Seidel relaxation scheme and the distributive Jacobi relaxation scheme. Both Lubrecht and Venner used a fast multilevel, multi-integration method to calculate the nodal deformations described by Brandt and Lubrecht[3].Wang et al [4] developed a multigrid scheme without using the Full Approximation Scheme (FAS) right hand side value for the film thickness equation. This was made possible by assuming the film thickness to be dependent on the pressure and not treating it as an independent quantity. Wang used the deformation calculation scheme developed by Brandt and Lubrecht.

This paper studies the effects of using a mixed relaxation scheme (Gauss-Seidel and Jacobi) versus just a Gauss-Seidel scheme with small under-relaxation factors. The authors use a deformation calculation scheme developed by Houpert and Hamrock [5]. The FAS right hand side is not calculated as suggested by Wang [4].

2. THEORY

The basic equations necessary for solving Reynolds equation using the multigrid method are described [2].

$$L_i = \frac{1}{(\Delta X)^2}\left[\in_{\frac{i-1}{2}} P_{i-1} - \left(\in_{\frac{i-1}{2}} + \in_{\frac{i+1}{2}}\right) P_i + \in_{\frac{i+1}{2}} P_{i+1}\right] - \frac{1}{(\Delta X)}[H_i - H_{i-1}] = 0 \quad \text{(Eq 1)}$$

where $\in = \frac{H^3}{\mu\gamma}$, $\gamma = \frac{3\pi^2 U}{(4W^2)}$, i = (2….maxnode).

The dimensionless film thickness at a certain node is described by [5]

$$H_i = h_0 + \frac{X^2}{2} + \sum_{j=1}^{N} D_{i,j} P_j \quad \text{(Eq 2)}$$

The updated value of nodal pressure is given by

$$P_i^n = P_i^o + w_{gs}\delta_i \quad \text{(Eq 3)}$$

for the multigrid method solved purely by relaxing the equations at each level using a Gauss- Seidel scheme.

For the solver that uses a combination of the Gauss-Seidel scheme and the Distributive Jacobi scheme, the updated values of pressure are given by

$$P_i^n = P_i^o + w_{ja}(\delta_i - \delta_{i-1}) \quad \text{(Eq 4)}$$

in the Jacobi region and by (Eq 3) in the Gauss-Seidel region.

In the Gauss-Seidel region, δ_i is calculated as

$$\delta_i = \left(\frac{\partial L_i}{\partial P_i}\right)^{-1} r_i \quad \text{(Eq 5)}$$

In the Jacobi region of the mesh, δ_i is calculated as

$$\delta_i = \left(\frac{\partial L_i}{\partial P_i} - \frac{\partial L_i}{\partial P_{i-1}}\right)^{-1} r_i \quad \text{(Eq 6)}$$

$$\frac{\partial L_i}{\partial P_i} = -\frac{1}{(\Delta X)^2}\left[\left(\epsilon_{\frac{i-1}{2}} + \epsilon_{\frac{i+1}{2}}\right)\right] - \frac{1}{(\Delta X)}\left[D_{i,i} - D_{i-1,i}\right] \quad \text{(Eq 7)}$$

$$\frac{\partial L_i}{\partial P_i} - \frac{\partial L_i}{\partial P_{i-1}} = -\frac{1}{(\Delta X)^2}\left[\left(2\,\epsilon_{\frac{i-1}{2}} + \epsilon_{\frac{i+1}{2}}\right)\right] - \frac{1}{(\Delta X)}\left[D_{i,i} - D_{i-1,i} - D_{i,i-1} + D_{i-1,i-1}\right] \quad \text{(Eq 8)}$$

The residual r_i is given by

$$r_i = F_i^k - \frac{1}{(\Delta X)^2}\left[\epsilon_{\frac{i-1}{2}} P_{i-1}^n - \left(\epsilon_{\frac{i-1}{2}} + \epsilon_{\frac{i+1}{2}}\right) P_i^o + \epsilon_{\frac{i+1}{2}} P_{i+1}^o\right] + \frac{1}{(\Delta X)}\left[H_i - H_{i-1}\right] \quad \text{(Eq 9)}$$

for the Gauss-Seidel region and

$$r_i = F_i^k - \frac{1}{(\Delta X)^2}\left[\epsilon_{\frac{i-1}{2}} P_{i-1}^o - \left(\epsilon_{\frac{i-1}{2}} + \epsilon_{\frac{i+1}{2}}\right) P_i^o + \epsilon_{\frac{i+1}{2}} P_{i+1}^o\right] + \frac{1}{(\Delta X)}\left[H_i - H_{i-1}\right] \quad \text{(Eq 10)}$$

for the Jacobi region.

A node is characterized as a node within the Gauss Seidel region if

$$\frac{\epsilon_i}{(\Delta X)^2} > 1$$

and characterized as a Jacobi region node if it is not part of the Gauss Seidel region.

A Full Approximation Scheme (FAS) is used to solve the equations. W(1,2) cycles of different levels are run to achieve converged values of pressure and film thickness. The number of levels for which the W cycles are run are 4, 5 and 6. W(1,2) cycles are preferred to the usually used W(2,1) cycles because it was observed that the former method achieved faster convergence.

To transfer the pressure and FAS right hand side values from a fine mesh to a coarse mesh a full weighting restriction operator I_{k+1}^k is used

$$I_{k+1}^k = \frac{1}{4}[\,1\;2\;1\,] \quad \text{(Eq 11)}$$

Transferring the fine grid data

$$P^{o(k)} = I_{k+1}^k P^{n(k+1)} \quad \text{(Eq 12)}$$

$$F^k = L^k\left(I_{k+1}^k P^{n(k+1)}\right) + I_{k+1}^k\left(F^{k+1} - L^{k+1}P^{k+1}\right) \quad \text{(Eq 13)}$$

where $P^{o(k)}$ is the initial value of pressure on a grid at level k. $P^{n(k+1)}$ is the final value of pressure obtained at level k+1. F^k is the FAS RHS described by Venner [2] at level k. At the finest level (k = m), F^k is 0. k = 1 is the coarsest grid level.

To transfer the pressure values from a coarse mesh to a fine mesh a full weighting interpolation operator I_k^{k+1} is used

$$P^{o(k+1)} = P^{n(k+1)} + I_k^{k+1}\left(P^{n(k)} - I_{k+1}^k P^{n(k+1)}\right) \quad \text{(Eq 14)}$$

The value for h_0 is adjusted on the finest grid each W cycle. An under-relaxation factor of 0.001 is used for adjusting the value of h_0 .

On the finest level the force balance equation is

$$\frac{1}{2}\Delta X^m \sum_{j=1}^{maxnode}\left(P_j^m + P_{j+1}^m\right) = \frac{\pi}{2} \quad \text{(Eq 15)}$$

where m refers to the finest grid level.

The following pressure convergence criterion is used

$$error_p = \left(\frac{\sum_{j=1}^{maxnode} |P_i^n - P_i^o|}{\sum_{j=1}^{maxnode} P_i^o}\right) < 0.001 \quad \text{(Eq 16)}$$

W(1,2) cycles are run for a 4 level system with the number of nodes at the finest level being 241 and the coarsest level 31. 3 relaxations are applied on the mesh at the coarsest level. Convergence is studied when using just the Gauss-Seidel scheme and a combination of both the Gauss-Seidel and the Jacobi relaxation schemes.

The algorithm describing the number of relaxations involved at each level is described by Wang[4].

3. RESULTS & DISCUSSION

W(1,2) cycles are run for a combination of the Gauss-Seidel and the Jacobi relaxation schemes. The Gauss-Seidel scheme is used mainly in the inlet where the value of the viscosity is not relatively high. The Jacobi scheme is used in the Hertzian contact width where the pressure values are large enough to cause a large viscosity gradient.

(**Fig. 1**) shows the convergence of the multigrid method for varying values of the Jacobi under-relaxation factors.

The number of W(1,2) cycles required for convergence in increasing order of the under-relaxation values shown in the graph are 356, 313, 289, 292 and 292 cycles respectively. The Jacobi under-relaxation factor 0.4 converges the fastet. w_{ja} values of 0.5 and 0.6 converge marginally slower than than a value of $w_{ja} = 0.4$ (**Fig. 5**). Convergence is not obtained for w_{ja} values greater than 0.6.

W(1,2) cycles are also run for a relaxation scheme using just the Gauss-Seidel method. These cycles were run on the same 4 grid levels as earlier, with the number of nodes on the finest grid being 241. The results are shown in (**Fig. 3**), and (**Fig. 4**).

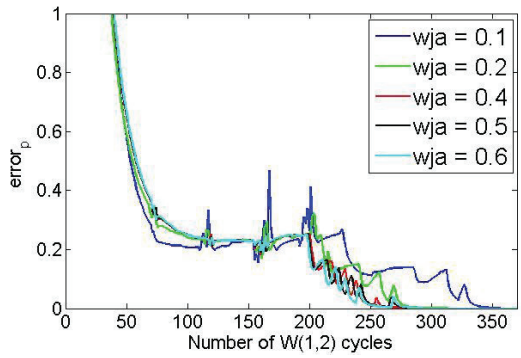

Figure 1 : *Convergence of the Reynolds equation for varying values of* w_{ja}.

(**Fig. 2**) shows the residual norm of of the finest level at the end of each W cycle. The residual norm (rn) is defined as

$$rn = \frac{1}{maxnode-1}\sum_{i=1}^{maxnode-1}|r_i| \qquad \text{(Eq 19)}$$

where $|r_i|$ is the absolute value of the residual at node i.

The rn values drop rapidly for about the first 100 W cycles and then stagnate or slightly increase before dropping off again. The flattening of each rn curve occurs around the same W cycle region as the flattened convergence curves in (**Fig. 1**). This seems to suggest that the stagnation of the residual norm values plays a role in the stagnation of the convergence curves.

(**Fig. 3**) shows the number of W cycles required for convergence as the Gauss-Seidel under-relaxation factors w_{gs} are increased. The number of cycles required at w_{gs} values of 0.1, 0.2 and 0.3 are 1276, 716 and 514 respectively. This is expected as a smaller under-relaxation factor updates the solution relatively slowly as compared to the higher under-relaxation factors. Convergence is not obtained for w_{gs} values of 0.4 and above.

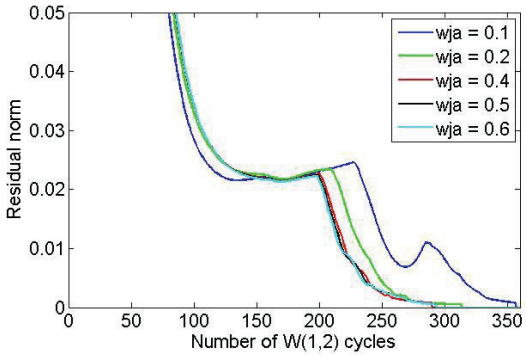

Figure 2 : *Residual norm for varying values of wja using a mixed relaxation scheme*

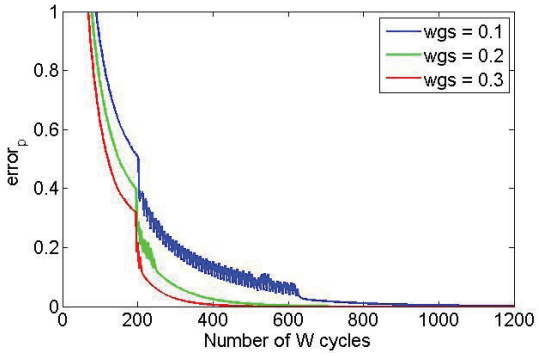

Figure 3 : *Convergence of Reynolds equation for varying values of wgs using only a Gauss Seidel relaxation scheme*

Wang[4] had stated that using just a Gauss-Seidel relaxation scheme leads to faster convergence than using a mixed relaxation scheme because the Jacobi relaxation slows down convergence. However these results show that using optimum Gauss-Seidel and Jacobi relaxation values leads to a faster convergence than the fastest converging Gauss-Seidel solution.

(**Fig. 4**) shows the rn curves for a 4 level W(1,2) cycle using only a Gauss-Seidel relaxation scheme. These curves are much more conventional in that the residual norm decreases faster as the under-relaxation factor is increased. This is also reflected in the convergence curves in (**Fig. 3**)

The fastest converging curves for each relaxation scheme are plotted in (**Fig. 6**). The mixed relaxation scheme converges much faster for about the first 75 cycles before flattening out until about the 200th W cycle. Both the curves once again increase their convergence rate after about 200 W cycles. These

curves show that the Gauss-Seidel scheme converges slower than the mixed relaxation scheme.

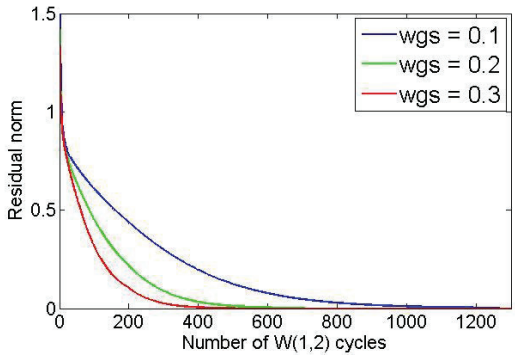

***Figure 4** : Residual norm for varying values of wgs using a Gauss-Seidel relaxation scheme*

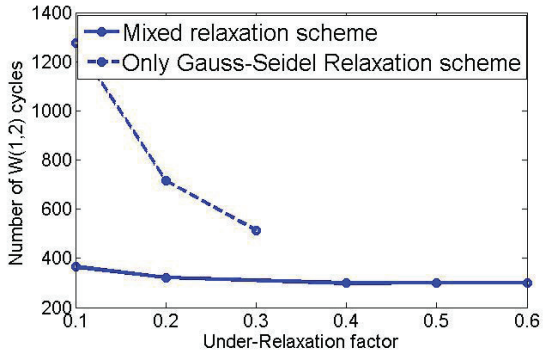

***Figure 5** : Comparison of the number of W(1,2) cycles to convergence for the 2 relaxation schemes*

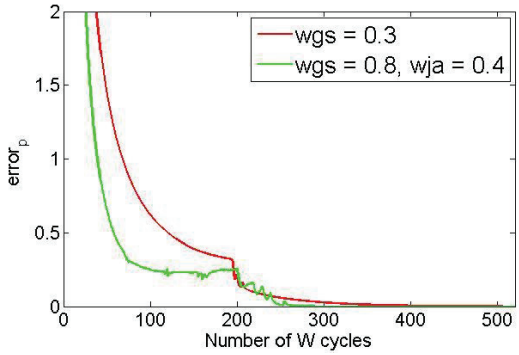

***Figure 6** : Comparison of the convergence of the two relaxation schemes*

W(1,2) cycles are also run for 3 separate maximum levels for the multigrid. The levels are 4, 5 and 6. The minimum number of nodes at each level is 31. The maximum number of nodes at each level is 241, 481 and 961 respectively.

(**Fig. 7**) shows the convergence patterns of the 3 different levels of multigrid solutions using a mixed relaxation scheme. As the mesh becomes finer, the accuracy of the solution increases. However lower frequency components of the error are introduced, thus increasing convergence time. (**Fig. 7**) also shows that there is no fixed w_{ja} value at which the fastest convergence can be reached. There seems to be an optimum value of w_{ja} and w_{gs} at which fastest convergence can be achieved .

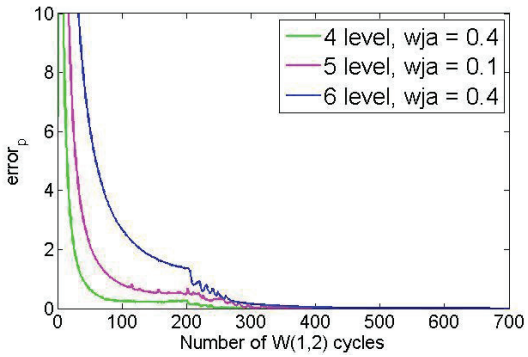

***Figure 7 :** Comparison of the convergence of varying multigrid levels incorporated in a W(1,2) cycle for a mixed relaxation scheme with w_{gs}= 0.8 .*

(**Fig. 8**) compares the residual norm of the mixed relaxation scheme for each of the 4 level, 5 level and 6 level multigrid. The 4 level solution converges after 289 W cycles, the 5 level solution at 418 cyles and the 6 level solution at 670 cycles.

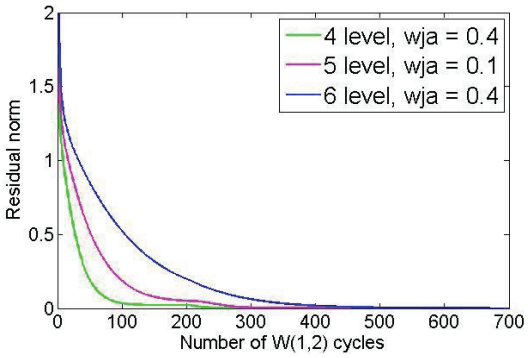

***Figure 8:** Residual norm for the 3 levels of multigrid solutions using a mixed relaxation scheme with w_{gs}= 0.8.*

5 level and 6 level multigrid solutions are also plotted using just a Gauss-Seidel relaxation scheme. Given that it is easier to predict the Gauss-Seidel under-

relaxation value at which the solution converges the fastest, a value of 0.3 was chosen.

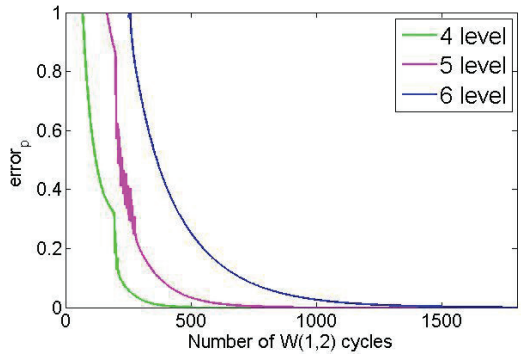

Figure 9: *Convergence curves for the 3 levels of multigrid solutions using a Gauss-Seidel relaxation scheme with* w_{gs} *= 0.3*

The multigrid solution with the finest scheme produces the slowest converging solution as expected (**Fig. 9**). The 4 level solution converges after 506 W cycles, the 5 level after 911 cycles and the 6 level solution after 1743 cycles.

The rn curves for the Gauss-Seidel solution for the 3 levels of solution is shown in (**Fig. 10**).

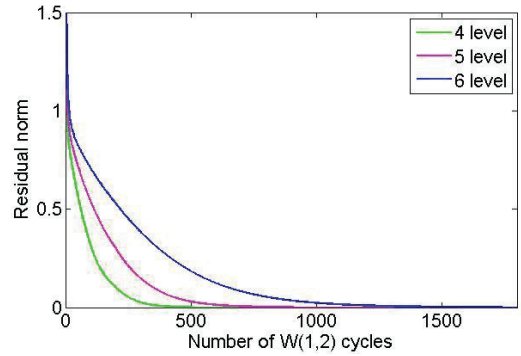

Figure 10: *Residual norm for the 3 levels of multigrid solutions using a mixed relaxation scheme with* w_{gs} *= 0.3.*

A 4 level multigrid solution is also run with the number of nodes on the finest level being 81 and the coarsest level being 11. The fastest converging solution was obtained for w_{ja} = 0.5 and w_{gs} = 0.1 . The solution converged after 371 W(1,2) cycles. Converging solutions were not obtained at w_{ja} values less than 0.5. This fastest converging solution (green curve) is plotted against the fastest converging 4 level solution, having 241 nodes as it's finest grid (pink curve) (**Fig. 11**).

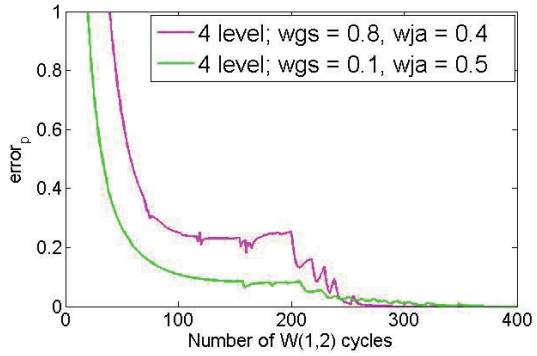

Figure 11: *Convergence curves for the two different 4 level solutions.*

The pink curve in (**Fig. 11**) refers to the 4 level solution with the coarsest grid having 31 nodes and the finest grid having 241 nodes. The green curve refers to the solution having 11 nodes at the coarsest level and 81 nodes at the finest level. The rn curves for the same solution is plotted in (**Fig. 12**). The curves are interesting because the green curve initially converges faster than the pink curve, but then flattens out and reaches convergence slower than the pink curve.

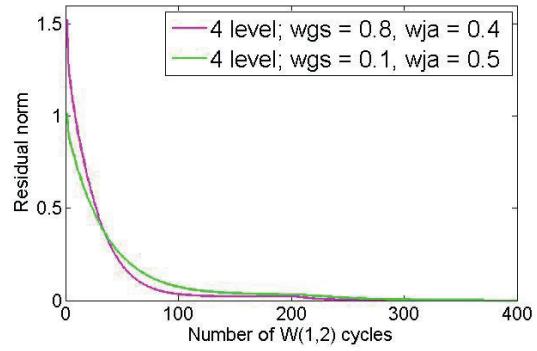

Figure 12: *Residual norm for the two different 4 level solutions.*

Thus the pink curve reaches convergence requiring a lower number of W cycles (289) as compared to the green curve (371). But given that each W cycle on the green curve requires a far computation than the pink curve, it takes far lesser time to achieve convergence on the system with the finest frid being 81 nodes and the coarsest grid being 11 nodes.

However as we approach a grid system where the finest level consists of a relatively small number of nodes, there is a loss in accuracy at the finest level.
The converged pressure spike values for the grid system having 81 nodes on the finest level and 241 nodes at the finest level are compared to the theoretical

pressure spike values predicted by Hamrock and Pan [6] in (**Fig. 13**) .

The theoretical value of the pressure spike for W' = 1.42e-4, U = 8.16e-12, G = 5007 is P_s = 0.659.

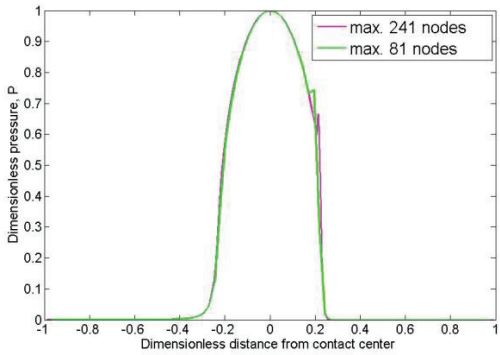

Figure 13: *Converged pressure curves for the two different 4 level solutions.*

The error in the pressure spike value for the system having 81 nodes on the finest level is 11.31% . The error for the system with 241 nodes on its finest level is 0.75% .

4. CONCLUSIONS

W(1,2) cycles are run to provide a multigrid solution to the EHL line contact problem.

- A relaxation scheme using a combination of the Gauss-Seidel scheme for the inlet region and the Jacobi scheme for the Hertzian region converges faster than a relaxation scheme using just the Gauss-Seidel method.
- A 4 level multigrid solution converges faster than a 6 level multigrid solution. This is because the larger number of nodes in the finest level of the 6 level solution introduce low frequency errors that decrease the convergence rate.
- For a multigrid solution using a mixed relaxation scheme, it is not straightforward to predict the combination of under-relaxation factors that lead to the fastest converging solution.
- For a multigrid solution using just the Gauss-Seidel relaxation scheme, the convergence rate increases with an increasing under-relaxation factor.
- For two 4 level multigrid solutions, the solution having a larger number of nodes on the finest level is more accurate than the solution having smaller number of nodes on the finest level.

5. NOMENCLATURE

b	Hertzian half contact width
E	equivalent Young's Modulus, Pa
G	Material Constant
H	dimensionless film thickness
P	dimensionless pressure, p/p_h
P_i^n	Newest value of dimensionless pressure
P_i^o	dimensionless pressure at previous step
p_h	Maximum Hertzian pressure, Pa
R	equivalent radius, m
U	dimensionless velocity parameter, $u\mu_0/ER$
u	lubricant inlet velocity, m/s
W'	dimensionless load
μ_0	ambient viscosity of lubricant, Pas
μ	dimensionless viscosity
w_{ja}	Jacobi under-relaxation factor
w_{gs}	Gauss-Seidel under-relaxation factor

6. REFERENCE

1. A.A. Lubrecht, W.E. Ten Napel, R. Bosma, Multigrid an alternative method for calculating film thickness and pressure profiles in elastohydrodynamically lubricated line contacts. ASME J Tribol 1986;108
2. C.H.Venner, Multilevel solution of the EHL line and point contact problems. Enschede: PhD thesis, university of Twente, Netherlands 1991..
3. A. Brandt, A.A.Lubrecht, Multilevel matrix multiplication and fast solution of integral equations. J Comput Phys 1990;90.
4. J. Wang, S. Qu, P. Yang, Simplified multigrid technique for the numerical solution to the steady-state and transient EHL line contacts and the arbitrary entrainment EHL point contacts. Tribology international 34 (2001), 191-202.
5. L.G. Houpert and B.J. Hamrock, Fast approach for calculating film thicknesses and pressures in elastohydrodynamically lubricated contacts at high loads. J. Tribol., vol. 108, 110.
6. B.J. Hamrock, P. Pan, R.T. Lee, Pressure spikes in elastohdrodynamically lubricated conjunctions. J. Tribol., vol. 110, no. 2, pp 279-284

Publication B

Laboratory simulation of rolling contact fatigue cracks inw ind turbine bearings using hydrogen infused 100Cr6 bearing steel
Presented at the 16th Nordic Symposium on Tribology - NORDTRIB 2014.

Laboratory Simulation of Rolling Contact Fatigue Cracks in Wind Turbine Bearings Using Hydrogen Infused 100Cr6 Bearing Steel

***S. Janakiraman*[1]*,*O. West*[1]*, P. Klit*[1]*, N. S. Jensen*[1]**

[1]*Technical University of Denmark, Nils Koppels Alle, bld. 404, 2800 Kgs. Lyngby, Denmark.*

Abstract

Premature fatigue failure is observed in rolling element bearings used in wind turbine components. It is believed that decomposed hydrogen from the lubricant diffuses into the surface of the bearing inner ring making it susceptible to failure. An attempt is made to simulate the formation of these cracks by accelerated laboratory tests. Hydrogen is artificially infused into the surface of ring specimens and the rings are then press fit onto shafts. This introduces a tensile Hoop Stress in the rings. The rings are then run against each other until fracture of one of the rings is observed. Preliminary test results show a failure characteristics similar to those observed in the inner rings of rolling element bearings used in service.

Keywords: Rolling Contact Fatigue, bearing failure, hydrogen charging, white etching areas, 100Cr6 steel.

*Corresponding author: Shravan Janakiraman (shja@mek.dtu.dk).

1. INTRODUCTION

Rolling element bearings used in wind turbine drive shafts experience premature rolling contact fatigue failure (RCF). These bearings are usually press-fit onto the shaft. This gives rise to a compressive radial stress and a tensile Hoop stress on the inner ring of the bearing. It is believed that diffusion of hydrogen from the lubricant plays a crucial role in their failure. Kohara et al., [1] conducted tests to conclude that the decomposition of the lubricant causes hydrogen to infuse into the fresh steel surface. Clark [2] states that the time for crack initiation decreases with the addition of a tensile Hoop Stress. Clark predicts that at a max. Hertzian radial stress of about 2GPa and a tensile Hoop stress of about 350GPa, the endurance life of the bearing is decreased by 88% compared to a bearing not under the influence of a Hoop Stress. Clark expects the crack initiation to occur in Mode I near the surface and change to Mode II as the circumferential stress decays. Czyzewski [3] modeled the effect of an applied Hoop Stress due to an interference fit. He estimated a maximum reduction in fatigue life of 98 %. White Etching Areas or Cracks (WEA/WEC) are a characteristic feature of failed bearings in wind turbines. Uyama [4] et al. conducted RCF tests on hydrogen infused bearing steel samples and observed that the fatigue life of these samples was shorter than the life of the uncharged samples. They also supposed that the basic role of hydrogen in these RCF tests is to localize plasticity. Evans [5] et al. conducted similar tests to study the white etching areas (WEA) formed subsurface in the test samples. They concluded that the WEA were initiated at inclusions. Evans also concluded that a certain threshold quantity of hydrogen, coupled with a maximum Hertzian stress value and number of cycles was necessary for the formation of WEA. Neither Uyama nor Evans applied any tensile Hoop Stress to their test specimens during the course of the experiments. Neither Czyzewski nor Clark studied the effects of the addition of hydrogen to the 100Cr6 bearing steels.

2. EXPERIMENTAL SET-UP

The test rig consists primarily of two drive shafts and a hydraulic cylinder (**Fig. 1**). One test ring is mounted on each shaft respectively. The two ring surfaces are brought into contact against each other by applying a normal load, using a hydraulic cylinder. The rings have a conical bore, fitting on a corresponding conical shape on the shafts. The contact pressure between the ring and shaft is controlled by the axial positioning of the ring on the shaft. Each drive shaft is capable of rotating at frequencies between 0-50Hz. There is a provision for relative slip between the two rings when the two shafts rotate at different frequencies respectively. Hence it is possible to create conditions of rolling and sliding.

An inlet resting above the contact between the two rings allows for the lubricant to flow into the contact. A torque transducer is attached to drive shaft 2, so the

interfacial torque generated between the two surfaces during slip can be measured.

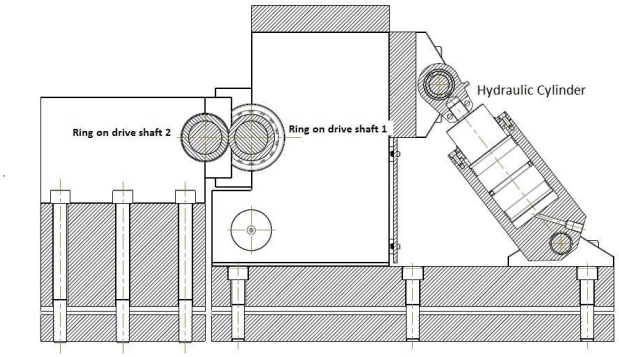

Figure 1: *Schematic of the Test Rig.*

The rings have an outer diameter of 70mm. One of the rings has a chamfered surface with an axial width of 7 mm. The angle of chamfer is 10 degrees. The opposing ring is unchamfered and has an axial width of 10mm.

The rings are through hardened, martensitic 100Cr6 bearing steel.

3. EXPERIMENTAL METHOD

Two rings are immersed in a 20% by weight aqueous solution of Ammonium Thiocyanate for 48 hours at 50º C. This process diffuses hydrogen into the rings. The quantity of hydrogen in the rings is not measured in this paper. Since Evans [5] observes that an increased quantity of hydrogen causes the WEA to be formed closer to the rolling surface, it is believed that the quantity of hydrogen beyond a certain threshold ppm value, does not change the mode of failure, but only changes the depth at which the WEA are formed.

The rings are removed from the solution after 48 hours, cleaned using ethanol and water and then slightly buffed to remove any oxidation layer on the surface.

Each ring is then press-fit mounted on a shaft and the process is completed when the outer diameter of each ring measures a certain pre-determined value that corresponds to a tensile Hoop Stress of 350MPa in the inner diameter and a compressive radial stress of 110 MPa. Once the rings are mounted on the shaft, the shafts are aligned as shown in **(Fig. 1),** so as to develop a line contact between the two rings.

The lubricant inlet is turned on and the shafts are then run at a frequency corresponding to the required inlet lubricant velocity. No load is applied at this time. A normal load is then gradually applied through the hydraulic cylinder. The loading is stopped when the required loading condition has been reached. The two shafts are run at a frequency very close to each other, so as to achieve conditions as close as possible to pure rolling. These test conditions are kept constant until the conclusion of the test.

The test is stopped when one of the rings develops a surface crack. Since there was no access to instruments that could check for in situ crack formations, the tests are run until visible surface cracks were generated. When the surface of either ring cracked, both the rings are dismounted from the shaft. The cracked ring is then sectioned to be observed under a microscope.

The fracture surfaces and the axial cross sections of the through cracked rings are observed by Reflecting Light Microscopy (RLM) microscope and Scanning Electron Microscopy (SEM). Three axial cross sections are prepared by making cuts parallel to the over-rolling direction from each ring around the area of the crack (**Fig. 2**).

The cross sections are studied to understand the failure mechanism.

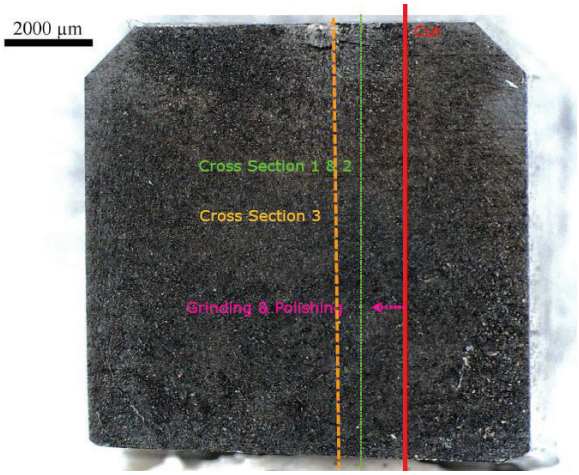

Figure 2 : Stereomicroscope image of the fracture surface of ring B1

A cut is made along the red line in (**Fig. 2**) and the sample is mounted. The specimen is then ground and polished, with material removed in the axial direction, until faces close to the crack are reached. White Etching Areas are usually observed in these axial cross sections. However, there may be some cross sections where the white areas might not be found as the total number of WEA can be small. Thus, the probability of finding a White Etching Area close to a crack

increases with increasing number of axial cross sections studied.

4. RESULTS & DISCUSSION

Table 1: *Number of cycles to failure for each ring pair.*

Ring Pair	Cycles to Failure (million)
A1 – B1	13
A2 – B2	11
A3 – B3	26
A4 – B4	11.5

The number of cycles to failure for each ring pair are shown in **Table 1**.

Of each ring pair that is tested, the test is stopped as soon as one of the rings fractured. The ring that is not fractured is not tested further to develop any surface cracks.

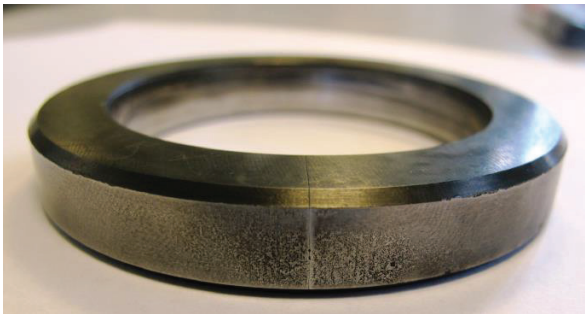

Figure 3 *: Axial crack on ring B1.*

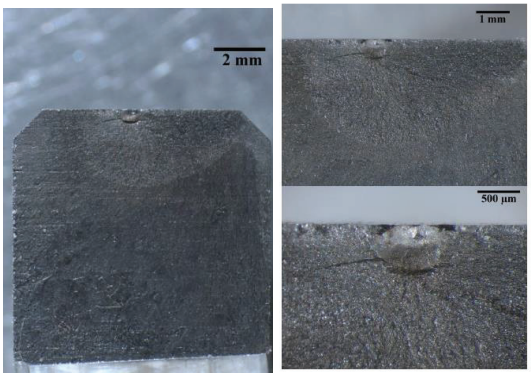

Figure 4: *Stereomicroscope images of the fracture surface of ring B1*

(Fig. 3) and **(Fig. 4)** show the fracture surfaces of the ring B1 that fractured after 11 million cycles. A cross section is defined as circumferential if the normal to that cross-sectional plane is pointed in the circumferential direction.

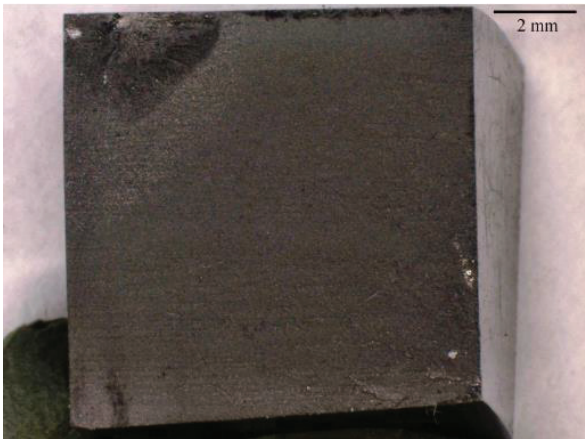

Figure 5: *Stereomicroscope image of the fracture surface of the ring A2*

(Fig. 4) and **(Fig. 5)** shows a resemblance to the fractured sample in the ball bearing fatigue test conducted by Clark [2]. The fracture surface shows a difference in texture between the top and bottom of the specimen. The rough, rounded portion close to rolling surface appears to have fractured by fatigue while the smooth lower portion appears to have fractured in a brittle manner.

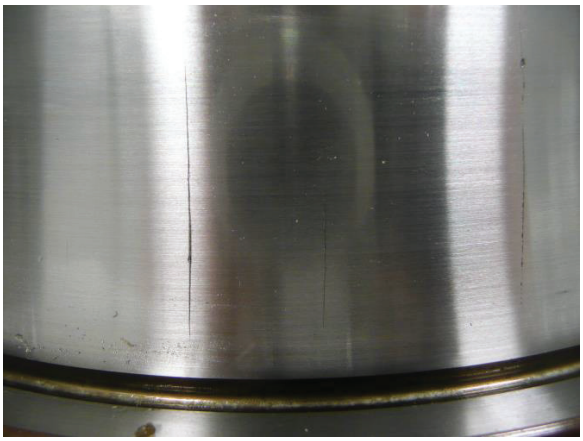

Figure 6: *Axial crack on the inner ring of a bearing from service*

(Fig. 6) shows multiple axial cracks on the inner ring of a tapered roller bearing from service. The bearing was positioned on the shaft at the intermediate stage inside the gearbox of a wind turbine. The gearbox belonged to a 2.3 MW turbine. The material is a through-hardened martensitic bearing steel. This

material is similar to the material of the test ring specimens used for testing. These cracks look similar to the axial crack on the surface of the ring B1 (**Fig. 3**). The failed bearing inner ring from service are sectioned, polished, etched and viewed under a microscope. Their failure characteristics are then compared to the failure characteristics in the laboratory simulated RCF rings.

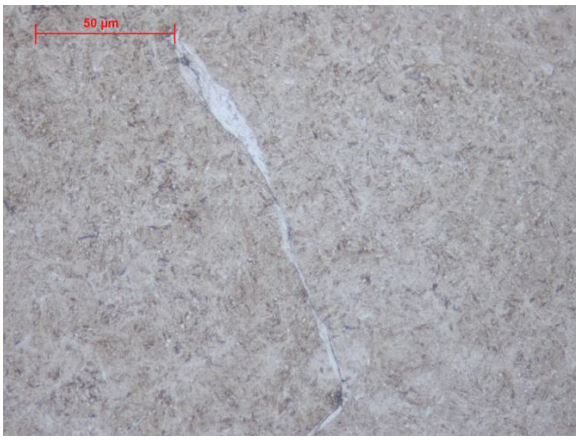

Figure 7: *RLM image* of a nital etched axial cross section (cut parallel to the over-rolling direction) showing a White Etching Area(WEA) around a crack in the inner ring of the bearing.

(**Fig. 7**) shows a characteristic WEA around a crack in an axial cross section of the bearing inner ring surface. It has been suggested by Kino et al., [6] that hydrogen plays a role in the formation of these WEA. Uyama [6] studied these WEA using a Transmission Electron Microscope (TEM) and observed that the white structure consisted of an ultra fine grained structure. He further suggested that the localized microstructural changes are caused by the hydrogen and hence supposed that the basic role of hydrogen is to localize plasticity.

(**Fig. 8**) shows a WEA found in an axial cross section near a crack formed subsurface. This crack is less than 20 microns from the rolling surface. This is believed to be because raised levels of hydrogen closer to the rolling surface, weaken the material and make it more susceptible to crack initiation. Evans [5] showed that decreasing the levels of hydrogen artificially infused in the surface of the ring causes these cracks to be formed much further away below the rolling surface.

(**Fig. 8**) shows a highly magnified SEM image of the WEA. The light triangular shaped region within the red dotted circle is suspected to be a deformity like an inclusion or a void formed at the location of a former inclusion, just like Evans [5] had predicted, although not yet confirmed by performing EDAX studies. The shape of the crack also seems to resemble the butterfly cracks described by Evans in the same paper.

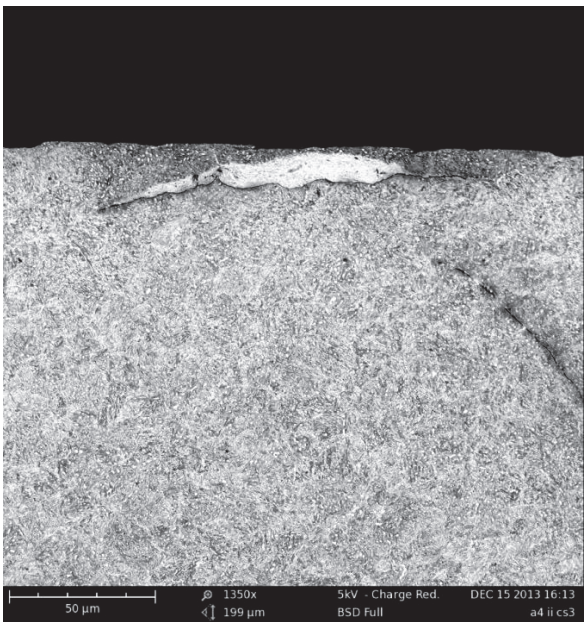

Figure 8: *WEA found near a crack on the failed lab specimen B2*

Figure 9**:** SEM image of the WEA around the crack

(**Fig. 3**) and (**Fig. 8**) also show pitting on the surface of the test specimen. Pitting could occur due to the presence of small solid contaminants in the lubricant, or due to a subsurface cracks growing to the surface.

The surfaces of the test specimens are also not highly polished mirror surfaces. The Ra for these test rings is approximately 0.15 microns. This could lead to a mixed lubrication regime in certain phases of the tests, leading to metal on metal contact and hence removal of surface material. The primary reason for pitting in these set of fatigue tests in not known and needs to be studies further.

The microscopic studies however do not conclusively prove as to whether the cracks are surface initiated cracks or if the cracks are initiated subsurface.

5. CONCLUSIONS

The preliminary microscopy studies have shown encouraging results with regards to simulating the cracks found in wind turbine bearing, in the lab by conducting RCF tests . Axial cracks are formed on the test specimen, leading to failure. These are similar to cracks found on the inner ring of the bearing from service. Light Optical Microscopy and SEM studies have shown the presence of the characteristic WEA in the test rings. These WEA are similar to the WEA observed in the axial cross sections of the inner ring of the bearing from service. The presence of a WEA close to the rolling surface (< 25 microns) indicates a high quantity of hydrogen supplied to the test specimen during the hydrogen charging process. It is still not confirmed whether the cracks initiate subsurface or at pitting sites on the rolling surface. Further samples need to be sectioned and studied to understand if the cracks initiate subsurface.

The test rig has shown the capability to simulate characteristic failure features observed in cracked bearing specimens, through accelerated RCF tests.

6. REFERENCES

1. M. Kohara, T. Kawamura, M. Egami, Study on Mechanism of Hydrogen Generation from Lubricants. Tribology Transactions, 49:1, 53-60, (2006), 1040-2004.
2. J. C. Clark, Fracture Tough Bearings for High Stress Applications, AIAA/SAE/ASME/ASEE 21st Joint Propulsion Conference, USA, 1985.
3. T. Czyzewski, Influence Of A Tension Stress Field Introduced In The Elastohydrodynamic Contact Zone On Rolling Contact Fatigue. Wear, 34 (1975), 201-214.
4. H. Uyama, H. Yamada, H. Hidaka, N. Mitamura, The Effects of Hydrogen on Microstructural Change and Surface Originated Flaking in Rolling Contact Fatigue. Tribology Online, 6, (2001), 123-132, 1881-2198.
5. M. –H. Evans, A. D. Richardson, L. Wang, R. J. K. Wood, Effect of Hydrogen on Butterfly and White Etching Crack (WEC) Formation under Rolling Contact Fatigue (RCF). Wear, (2013).
6. N. Kino, K. Otani, The Influence of Hydrogen on Rolling Contact Fatigue Life and its Improvement. JSAE Review, 24, 2003, 289-294.

Publication C

Observations on the effect of varying Hoop stress on the fatigue failure and the formation of White Etching Areas in hydrogen infused 100Cr6 steel rings.
Submitted to International Journal of Fatigue, August 2014.
Accepted for publication on 01-03-2015.

Observations of the effect of varying Hoop stress on fatigue failure and the formation of White Etching Areas in hydrogen infused 100Cr6 steel rings

Shravan Janakiraman[a], Ole West[a], Peder Klit[a,*], Niels S. Jensen[a]

[a]*Department of Mechanical Engineering, Technical University of Denmark, Lyngby 2800, Denmark*

Abstract

White etching cracks (WECs) in wind turbine gearbox bearings have been studied previously. Rolling contact fatigue (RCF) tests are conducted on 100Cr6 bearing steel rings, in this study, to generate WECs like those found in wind turbine bearings. This research studies the effect of two different levels of tensile Hoop stresses on the failure life and formation of WECs in the rings. The rings are pre-charged with hydrogen before RCF tests are conducted. It is found that these rings experience incremental fatigue failure, followed by a sudden rapid failure. The fractography, Reflecting Light Microscopy (RLM) and Scanning Electron Microscopy (SEM) results are presented in this paper.

Keywords: rolling contact fatigue, bearings, hydrogen charging, hoop stress

1. Introduction

Rolling element bearings experience premature rolling contact fatigue (RCF) failure in engine auxiliary devices and wind turbine drive trains [1–5, 9–11, 38, 44]. Their fatigue failure is characterized by the formation of regions of microstructural changes along cracks called white etching areas (WEAs) [5, 8, 12–14]. WEAs appear white when the sectioned and polished cross-sections of the bearing sample are etched in nital and viewed with the Reflecting Light Microscope (RLM). The cracks bordering or passing

*Corresponding author. Ph:+45 45256267
Email address: klit@mek.dtu.dk (Peder Klit)

through WEAs are termed White Etching Cracks (WECs). [15] showed that the WEA is a region of ultra fine grained material formed by cyclic plasticity. The grains vary in size from 10nm to 300nm [2, 30, 31, 46, 52, 54, 57, 58]. WEAs are thought to be caused by 2 main factors, viz. transient operating conditions like sliding, vibrations etc. [8, 20] and diffusion of hydrogen into the surface of the bearing steels [5, 8, 12–14, 21].

According to [8], WECs likely initiate subsurface. However a complete three-dimensional view of the crack network could indicate surface interaction. Hence it is important not to make final judgements based on viewing a single cross-section, which represents a two-dimensional view of a three-dimensional crack network. [38] showed that WECs can be surface initiated. [55] suggested subsurface initiation at inclusions. [19] conducted extensive work to conform that subsurface initiation at non-metallic inclusions was one mechanism of WEC formation. Serial sectioning of failed bearings from service [56] and test specimens from experiments [16, 18] provided significant metallographic analysis that proved that WEC formation could be subsurface. Further research needs to be conducted to obtain a clearer understanding of WEC formation mechanisms.

Hydrogen embrittlement has been studied extensively [22–26, 28, 29]. Yet these studies do not fully explain the role of hydrogen in the failure of bearing steels. [21, 27] supposed that the effect of hydrogen is to localize plasticity and cause microstructural changes. Hydrogen weakens the bearing steel by decreasing mode I and mode II failure stress limits [32, 33].

Hydrogen has been found to diffuse into the surface of steels during rolling contact tests [5, 12, 14, 42]. [41] observed the diffusion of hydrogen into the steel surface while conducting ball on disk sliding tests. Hydrogen diffused into the surface of the bearing steel resides either in diffusible form or non-mobile form [34–37]. Hydrogen is believed to enter into the surface of steels by tribochemical reactions occurring at surface cracks [38] or fresh steel surfaces formed by wearing of the surface [41].

Measuring the concentration of hydrogen in bearing steels is an onerous task. Hydrogen diffuses out of the steel at room temperature. This study does not measure the hydrogen concentration during testing. However other studies have measured the concentration of hydrogen in their samples

[5, 12, 16, 21, 43–45]. Given the uncertainties associated with the testing conditions, the measured concentrations vary significantly and no comparison can be made between them. However, despite the difficulties with measurement and interpretation, what could be gleaned from these previous studies is that perhaps only a small concentration (less than 1 ppm) of mobile hydrogen is required to promote the formation of premature RCF damage.

The hydrogen charging conditions for the two Hoop stress levels in this study are kept the same. During the charging process, no stress is applied to the ring. Hence it is assumed that the concentration of hydrogen diffused into each ring does not vary because the charging conditions are exactly replicated. The concentration of hydrogen diffused into the bearing surface in offshore wind turbines is hard to measure. Given the delay in time to extract the bearing from the gearbox to the actual measurement of hydrogen in the lab, most of the diffused hydrogen escapes the bearing.

The maximum Hertzian contact pressures applied in this study are similar in magnitude to the pressures experienced in wind turbine gearboxes (less than 2 GPa [16]). WECs have been generated by other researchers at much higher pressures (greater than 3GPa) [5, 9, 12, 14, 21, 43, 44, 46–48]. The test rig used in this study to conduct RCF tests is unique because the shafts allow for a conical fit of the rings, thus enabling the application of a simultaneous static tensile Hoop stress and compressive radial stress. So a study is done to observe the differences in WEA formation at two different tensile Hoop stress levels and their Weibull curves are plotted.

2. Test-Rig

The test rig consists primarily of two drive shafts and a hydraulic cylinder (Fig. 1). One test ring is mounted on each shaft respectively. The two ring surfaces are brought into contact against each other by applying a normal load, using a hydraulic cylinder. Each ring has a conical bore, fitted onto a corresponding cone on the shaft. The contact pressure between the ring and shaft is controlled by the axial positioning of the ring on the shaft. Each drive shaft is capable of rotating at frequencies between 0-50 Hz. There is a provision for relative slip between the two rings when the two shafts rotate at different frequencies respectively. Hence it is possible to create conditions

of rolling and sliding. Drive shaft 2 is connected to the master motor and drive shaft 1 is connected to the slave motor. In the current study there is no application of slip in the RCF tests.

An inlet resting above the contact between the two rings allows for the lubricant to flow into the contact. The lubricant used is Mobil Delvac synthetic gear oil 75W-140, which is a fully synthetic, heavy duty drivetrain lubricant. This lubricant has a viscosity $182cSt$ at 40°C and $25cSt$ at 100°C. The lubrication is not pressurised and the lubricant is allowed to fall freely, from a distance of approximately 2cm, into the conjunction between the two rings.

A torque transducer is attached to drive shaft 2, so the interfacial torque generated between the two surfaces during slip can be measured. When one of the rings fails, the torque readings fluctuate wildly, setting off an internal alarm and automatically shutting down the test rig.

Each ring has an outer diameter of 70mm. One ring has a chamfered surface with an axial width of 4mm or 7mm. The angle of chamfer is 10 degrees and 45 degrees respectively. The ring opposing the chamfered ring is unchamfered and has an axial width of 10 mm. Even though the axial widths of the chamfered rings may vary from test to test, the load is adjusted so that the maximum Hertzian pressure at the conjunction is kept the same. The maximum Hertzian pressure is 1.65 GPa. The contact half width is 0.55 mm. Based on the analytical formula for the minimum film thickness provided by [60], the value of the minimum film thickness in the conjunction is 1.8 microns. The lambda value for this conjunction, given the surface roughness $R_a = 0.15$ microns, is 12. This value of lambda points to a full film lubrication in the conjunction. The inner diameter of each ring is tapered at (2.86°) so as to enable a conical fit on the shaft. The Hoop stress is calculated analytically using Eq. 1.

$$\sigma_{\theta\theta(r=r_f)} = \frac{E.d}{2}\frac{r_b^2 + r_f^2}{2.r_b.r_f^2} \tag{1}$$

where

E is the effective Elastic Modulus, r_f is the fit radius, r_b is the outer

radius of the hub, d is the increase in outer diameter of the ring.

The ring material is standard 100Cr6 martensitic bearing steel. The steel is austenitized at 850°C, quenched and twice tempered at 180°C. Each ring is cut out from a cylinder of heat treated bearing steel.

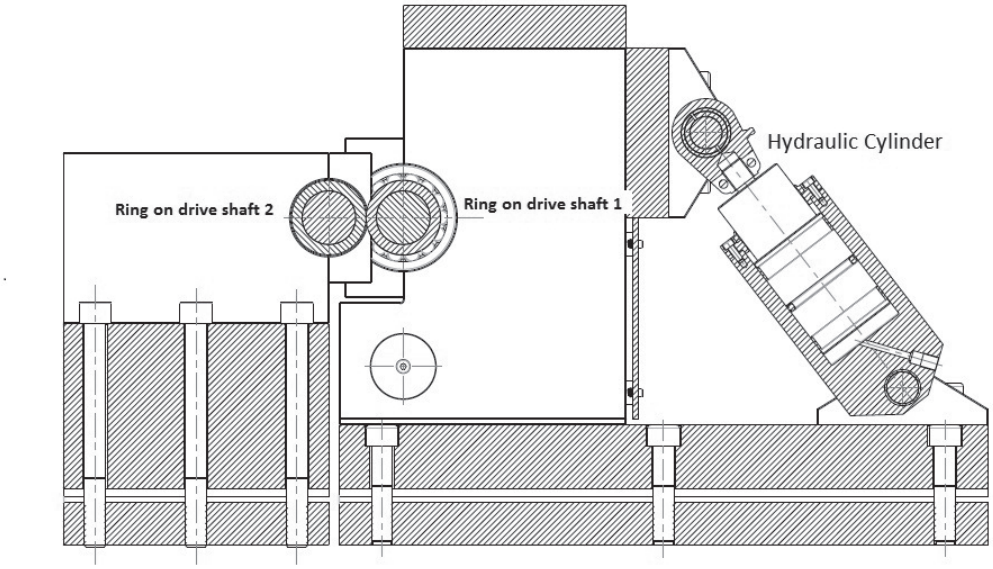

Figure 1: Schematic of the Rolling Contact Test Rig

3. Experimental method

The input parameters used in each RCF test are shown in Table 1. The tests are are run until one of the rings fails.

Initially hydrogen charging was carried out at conditions replicating those found in literature [16][21]. Each ring is wiped with a clean paper towel and then cleaned with ethanol. The ring was then immersed in a solution of 20 wt.% Ammonium thiocyanate at 50° C for 48 hours.

Since there was no access to quantitatively measure the concentration of hydrogen, a qualitative measurement was done using GDOES (Glow Discharge Optical Emission Spectrometry). With GDOES concentration depth profiles can be measured if reference standards with known concentrations

Parameter	Value
Max. Hertzian Pressure	1.65GPa
Inlet lubricant velocity	20m/s
Inlet lubricant temperature	35°C
Slide-Roll Ratio	0 (pure rolling)
Surface roughness after hydrogen charging	$R_a = 150nm$

Table 1: Input parameters for the RCF tests

are available. No standards were available for the measurement of hydrogen. Thus, just the measured voltage versus the sputtering time can be observed. A sputtering time of 360 seconds was used. The GDOES measurements were made to obtain only a qualitative comparison in diffused hydrogen between the charged and the uncharged samples. A quantitative measurement of the depth of charging and the concentration of hydrogen cannot be made because of the non-availability of a hydrogen reference standard. GDOES results showed an increase in the voltage close to the surface. This can be interpreted as a relative increase in hydrogen concentration with hydrogen charging Fig. 2. Thus the charging process is shown to have diffused hydrogen into the steel surface.The authors would once again like to emphasize that no measurement of the actual hydrogen concentration and depth of diffusion can be made in Fig. 2.

A conservative estimate of the depth of diffusion is made based on the well known formula $x = \sqrt{Dt}$, where x is the penetration depth of hydrogen, D is the diffusion coefficient of hydrogen in steel and t is the time. [6] mentions that the typical value of D in steels is $10^{-11}m^2/sec$. [7] showed that the value of D decreases with increasing carbon concentration in steels. So a conservative estimate of 10^-12 is assumed to be the diffusion coefficient of hydrogen in 100Cr6 bearing steel. 100Cr6 is a high carbon steel (approx 0.97% C). Since the charging time is 24 hours, $t = 86400sec$. Using these values an approximate penetration depth of 300 microns is calculated.

It was noticed that there were small micro-sized indents formed on the surface of the bearing steel after the hydrogen charging. These micro indents are observed even after testing Fig. 3c. However, RCF tests were still conducted on these rings to check if WECs could be generated using

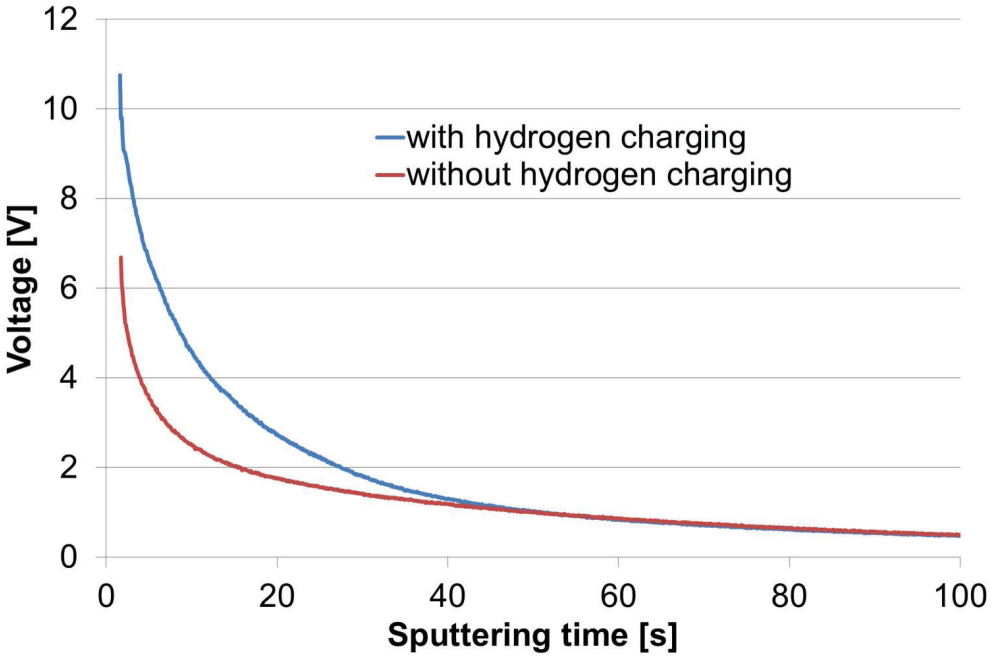

Figure 2: GDOES results showing the relative increase in hydrogen concentration after hydrogen charging

the RCF test rig and were used to calibrate the test rig and input conditions. As shown later, WECs were formed during the fatigue failure of these 100Cr6 bearing steels. Fig. 3 shows the micro-indents on the running surface of the rings A4 and B4. Ring B4 was run against ring A4 until the latter fails.

It was postulated that the micro-indents on the surface of the ring were formed due to insufficient cleaning of the ring surface before hydrogen charging. Hence the cleaning process was improved by cleaning the surface of each ring with toluene and acetone. The surface of each ring was wiped with a clean paper towel. The ring was then immersed in toluene for 4 minutes, taken out, wiped clean and then immersed in acetone for 4 minutes.

This cleaned ring was then immersed in a 20 wt.% ammonium thiocyanate solution at 50°C for 48 hours, mimicking the previous charging conditions . While fitting the ring on the shaft, it was observed that the fully cleaned, hydrogen charged ring experienced brittle fracture upon mounting. It is pos-

tulated that there was an increased diffusion of hydrogen into the surface of the ring due to a cleaner ring surface. This excess hydrogen concentration weakened the material and the tensile Hoop stress, due to mounting, caused brittle failure. So the concentration of the thiocyanate solution was decreased from 20 wt.% to 12 wt.% and the rings were immersed in solution for 24 hours instead of the original 48 hours. This new cleaning and hydrogen charging method led to no micro-indents on the surface and no brittle fracture while mounting the ring on the shaft. No GDOES analysis was made on the rings when charged in 12 wt. % Ammonium thiocyanate solution for 24 hours.

(a) cracked ring A4

(b) ring B4 not run until failure

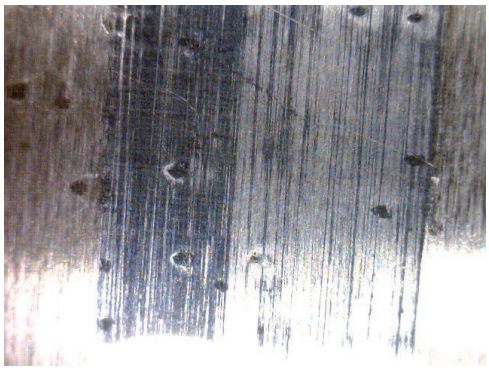

(c) magnified image of microindents on ring B4

Figure 3: Micro-indents on unchamfered rings A4 and B4 after hydrogen charging and fatigue testing

After a ring fails, it is sectioned for reflecting light microscopy (RLM). The fracture surface (with plane normal to the circumferential direction) is viewed under a Leica MZ 125 stereo microscope equipped with a Leica

DFC450C camera (cooled CCD). Then it is hot mounted, ground and polished to reveal a circumferential cross section just below fracture surface. This cross section is etched with 2% nital and observed under a Olympus CK40M microscope equipped with a Leica DFC450C camera (cooled CCD) to look for WECs. Suspected WECs are investigated with a Phenom ProX Desktop Scanning Electron Microscope (SEM) to confirm their presence and perform detailed investigations of associated WEAs under high magnification. The SEM uses a back scattered electron detector. Additionally it is investigated if the WECs formed in this study are initiated at assessing the single cross-sectional planes prepared by metallography with RLM and subsequently SEM. If any features were suspected as possible inclusions or inclusion sites, these were subsequently analyzed by performing Energy Dispersive X-Ray Spectroscopy (EDS). If no WECs are found in the circumferential cross section, axial cross sections, adjacent to the fracture surface, are investigated as well. However no serial sectioning of the rings is performed for microscopy. Serial sectioning is defined as sectioning a series of of cross sections close together, so as to be able to piece together a three-dimensional view of the crack surface.[16] performed serial sectioning in test samples by grinding and polishing cross-sections of the test-rollers at approximately 3 microns material removal interval in the circumferential direction.

4. Results of RCF calibration tests

The rings with micro-indents, formed due to poor cleaning processes, are mounted on the shafts and run against each other in lubricated RCF tests. The input parameters for the tests are given in Table 1. This set of tests are run for a tensile Hoop stress of 350MPa and a compressive radial stress of 110MPa. The number of cycles to failure for each failed ring is given in Table 2. Of the 6 rings that experienced fatigue failure, WECs were found close to the failed surface on 4 of the rings. The fact that there were no WECs observed on the two rings (A4 and A15) does not necessarily point to a lack of WEC. As no serial sectioning for microstructural investigation is performed, the presence of WECs is only checked at one circumferential cross section close to the fracture surface. WECs could potentially be present away from the investigated cross-section.

The fractographs of the failed ring surfaces are shown in Fig.4. The surfaces shown are the fracture surfaces, normal to the circumferential direction

ring number	cycles to failure (millions)	WEC found?
A4	13	No
A8	27	Yes
A11	24.2	Yes
A15	11.5	No
B5	11	Yes
B11	26.4	Yes

Table 2: Number of cycles to failure for the poorly cleaned rings at 350MPa Hoop stress and charged with 20 wt.% ammonium thiocyanate solution

of each ring. The red dashed line in each fractograph demarcates the transition between incremental fatigue crack propagation and final, rapid failure. After initiation, the crack propagates by fatigue until a point is reached where the reduced cross-sectional area is unable to support the load any further and sudden, final fracture occurs. The dark regions seen in some of the fracture surfaces like Fig. 4b and Fig. 4d are caused by the seepage of the lubricant. In some tests, the test rig is not automatically stopped even after the ring is broken, because the failure criterion to set off the control panel that stops the rig is not adequately set. So the tests need to be stopped manually and some tests run for about 15 minutes even after a ring has failed. This run time with the separated surfaces still being inundated with the lubricant is responsible for its seepage into the surface of the ring. Furthermore, running of the fractured ring can cause friction between the opposing fracture surfaces. This can change the original fracture morphology, thus impeding the identification of the transition between incremental and rapid crack growth.

The incremental crack growth region is characterized by a rougher appearance while the sudden crack propagation region is characterized by a much smoother surface. The crack initiation, indicated by a high reflective zone, in most cases appears to occur very close to where the chamfered surface comes in contact with the flat surface. For example, in Figures 4a, 4b and 4d, the initiation points appear to be very close to about 1.5mm from the axial planes (the ring sides) either to the left or the right. This point is where we expect the chamfer in a 7mm wide ring to contact the 10 mm wide flat surface of the opposing ring. In Fig. 4c the width of the contact is 4mm and the initiation appears to have occurred very close to where the chamfer

begins. However in Fig. 4e the initiation occurs at the center of the axial width and away from the chamfer.

Fig. 5 shows the results of the Reflecting Light Microscopy (RLM) on the fractured rings that showed WECs upon etching with nital. In most of the figures, (5a, 5c and 5d), it is observed that the WECs lie very close to the surface (less than 50 microns). There are multiple probable reasons for this observation. One of the reasons could be that the hydrogen concentration could be the highest in this zone. In Fig. 2 the GDOES results shows a decrease in hydrogen concentration with sputtering time. As the sputtering depth increases with sputtering time, it would be logical to conclude that the concentration of hydrogen decreases as we go deeper into the ring surface. Another reason could be the micro-indents observed on the running surface during run-time. These indents have probably been formed due to small contamination in the lubricants. The micro-indents create a local region of mixed/boundary lubrication, thereby increasing the traction coefficient. [39] and [40] showed that increasing traction coefficient brings the maximum shear stress close to the surface. This could initiate WECs closer to the surface. The maximum shear stress depth for a smooth surface has been calculated to be approximately 400 microns. It is also possible that the WECs could have initiated on the running surface, thereby causing the WECs to lie closest to it. In some cases like Fig. 5a and Fig. 5d, the cracks are irregular shaped and grow into a network. In the other rings, the WEAs appear to form along a single crack and no crack networks are visible.

The WEAs are found in the circumferential cross sections very close to the fracture surface. Regions further away from the fracture surface are not studied.

Fig.6 shows axial cracks formed on the raceway of the inner ring of an intermediate stage, tapered roller bearing from a wind turbine gearbox. This inner ring is made of 100Cr6 martensitic steel, similar to the ring material used in this study. These cracks Fig.7 have a radial orientation with respect to the contact surface, which may be a consequence of how these cracks propagate. A crack network with WEAs is observed close to the main crack. These WECs are similar in appearance to the WECs observed in Fig.5.

The SEM images of WECs in Fig. 5 are shown in Fig. 8. It is believed

that WECs are formed at inclusions [16–19, 21, 44, 55]. No evidence for crack initiation at inclusions is found by analysing the single cross-sectional planes close to the fracture surface by RLM, SEM and SEM EDS of possible inclusion sites. The presence of voids along the cracks suggest potential inclusion sites. There is another interesting feature to observe in these WEAs. Usually carbides are reported to be largely absent in WEAs [54] [59] [53]. However some of the WEAs (Fig. 8b) show the presence of many carbides, while others like Fig. 8a exhibit a WEA almost completely bereft of carbides. [9] [51] [50] suggested that carbides are dissolved due to severe plastic deformation during RCF. [2, 31, 53] observed the presence of carbides that appear to be in an early stage of a dissolution process in WEAs.

5. Results of RCF tests at varying Hoop Stress

ring number	Hoop stress	cycles to failure (millions)	WEC found?
A19-b	440	8	Yes
A20	440	19	Yes
B23	440	11	Yes
B24	440	11.8	Yes
B26	440	12	Yes
A27	440	13.8	Yes
A26	540	2.9	No
B28	540	10.6	Yes
A29	540	6.2	Yes
B30	540	4.2	Yes
B33	540	7.0	Yes

Table 3: Number of cycles to failure at different Hoop stress levels and charged with 12 wt.% ammonium thiocyanate solution

The tests in this section have been conducted on rings cleaned with toluene and acetone. There are no observable micro-indents on the surfaces of these rings after hydrogen charging with 12 wt.% thiocyanate solution. RCF tests are conducted at varying tensile Hoop stress levels (440 MPa and 540 MPa) as shown in Table 3. The corresponding compressive radial stresses at 440 MPa and 540 MPa Hoop stresses are 138 MPa and 165 MPa respectively. Weibull curves are plotted for the two tensile stress levels and shown in Fig.

9. The Weibull curves show a decrease in the fatigue life of these samples at the higher Hoop stress level. The higher tensile Hoop stress decreases the Mode I failure stress limit.

The fractographs for the failed rings at 440MPa and 540MPa tensile Hoop stresses are shown in Fig. 10 and Fig. 11 respectively. Most of the failed rings have cracks initiated close to the chamfer, while in Fig. 10f, Fig. 10e and Fig. 11b the cracks are initiated away from the chamfer. In rings where the incremental fatigue crack propagation region is easily discernible, red dashed lines are drawn to mark the region. The incremental fatigue crack propagation areas at 440MPa tensile Hoop stress appear to be slightly larger than their counterparts at 540MPa (except for ring B23). This is because the higher tensile Hoop stress requires a shorter critical crack length for sudden fracture to occur. We are unable to show the fractography images for ring A26 due to problems retrieving the saved image. The subsequent grinding of the fracture surface did not allow for fractography to be re-performed on ring A26.

Fig.12 and Fig. 13 show the WECs on the cross sections of the fractured rings at 440MPa and 540MPa tensile Hoop stress respectively. WECs are observed on all the rings at 440MPa Hoop stress. Some rings show WECs at multiple locations. The WECs closest to the rolling surface are shown in Fig.12. They lie at a depth between 40-60microns in each ring except ring A20 at 440MPa Hoop stress. The WEC in Ring A20, closest to the surface, is at a depth of about 110 microns from the rolling surface. Ring A20 also took the longest time to fail out of all the rings at 440MPa.

At 540MPa Hoop stress, in rings A29, B30 and B33 WECs are found at a depth of about 70 microns from rolling surface. In ring B28, WECs are found at a depth of 450 microns. B28 takes the highest number of cycles to fail at 550MPa Hoop stress (10.6 million) compared to 2.9, 4.2, 6.2 and 7 million cycles for the other rings. It is interesting to note that the rings that take the longest time to fail, show WECs at depths further away from the rolling surface. However, no conclusions can be drawn relating the number of cycles to failure to the depth of WECs from the rolling surface due to insufficient number of samples tested and cross sections investigated. WECs are easily observed under the RLM in ring B28 and B33. In ring A26 no WECs are observed and in rings A29 and B30 the suspected WEAs bordering observed

cracks are very small. SEM inspection is necessary to confirm their presence or absence.

Fig. 14 confirms the microstructural changes associated with WEAs observed in Fig. 12. Rings A27 and B23 show undissolved spherical carbides inside the WEA resembling those seen previously in ring B5. The WEAs on the other rings appear to be free of spherical carbides. At 540MPa Hoop stress in rings A29 and B30, the small WEAs are confirmed only by observing the morphology in the SEM. In ring A26, no WEAs are found close to the fracture surface. In general the smallest WEAs are found in the rings that failed after the lowest number of cycles (rings A29 and B30). This is in agreement with the mechanism proposed by [44]. During each cycle, the microstructure adjacent to the crack undergoes severe plastic deformation. Material transfer by a bonding/debonding sequence between the crack faces occur, leading to a deposition of WEA on the receiving side of the crack. This mechanism leads to an incremental increase in WEA on the crack sides with each cycle.

No evidence for crack initiation at inclusions is found by analysing the single cross-sectional planes close to the fracture surface by RLM, SEM and SEM EDS of possible inclusion sites. However it should be noted that the WEC is a 3-dimensional crack network, therefore inclusions interacting with WECs may be present in planes in the near vicinity.

Fig. 16 shows the RLM and SEM images of the failed ring A24. Ring A24 is not charged with hydrogen. The tensile Hoop stress on mounting is 540MPa. The number of cycles to failure for this ring is 45 million cycles. In Fig. 16a there is no clear boundary between the incremental crack growth region and the rapid crack growth region. Although this ring required a higher number of cycles to failure compared to the other rings at the same Hoop stress, no WEAs are visible close to the fracture surface (Figures. 16b, 16c, 16d, 16e).

Under the current test conditions, with no slip, it is possible to provoke failure with no hydrogen charging. However the test conditions do not appear to be conducive enough to promote the formation of WECs without hydrogen charging of the ring. More tests with uncharged ring samples are not performed due to long testing times.

6. Conclusions

RCF tests have been conducted on hydrogen charged 100Cr6 martensitic rings. The rings are press-fit onto shafts introducing a tensile Hoop stress and a compressive radial stress. Cross-sections close to the fracture surface are investigated. The following conclusions are noted.

1. The RCF tests performed show that WECs similar to those observed in the inner ring of wind turbine bearings can be generated using the test-rig on hydrogen charged rings.
2. The failed rings experience incremental fatigue crack propagation followed by final, rapid failure.
3. WEC networks and WEAs along a single crack are both observed in the failed rings. All the failed rings tested at 440MPa tensile Hoop stress exhibit WEAs. However at 550MPa, the ring that failed the earliest does not show any WEAs close to the fracture surface.
4. WEC initiation can occur both surface and subsurface as seen from the literature review. Fig. 5, Fig. 12 and Fig. 13 do not show a clear evidence as to whether the WECs were initiated on the surface or subsurface. While the WECs are close to the surface they do not appear to be connected to the surface. Since this is a two-dimensional cross section and no serial sectioning has been done, it is not possible to state with certainty that the WECs are not connected to the surface. No inclusions are detected along the WECs but voids, which could be possible inclusion sites, are observed along some cracks. Since these cross sections are two-dimensional we cannot state with certainty that inclusions are not present in the three-dimensional crack network. Hence we cannot conclude if the WECs were initiated on the surface or subsurface. Serial sectioning needs to be performed to obtain a complete picture of the crack network and ascertain the initiation mechanism of the WECs.
5. Some WEAs show the presence of carbides but they are absent in most cases. No conclusions can be drawn relating the presence of carbides in the WEAs to the number of cycles to failure.
6. The number of cycles to failure decreases as the tensile Hoop stress is increased.
7. The incremental fatigue crack propagation region appears smaller in failed rings at 550MPa compared to that at 440MPa. This could be because a shorter critical crack length is required for sudden failure at the higher Hoop stress.

8. At lower number of cycles to failure, it becomes harder to spot WEAs in the failed material based on single cross-sections close to the fracture surface. It is suggested that with each cycle, there is an incremental increase of WEA, due to continued plastic deformation and material transfer between the crack faces.

7. Acknowledgements

The authors would like to thank Strecon A/S for providing the rings. The authors also thank Mathijs Vanhauwaert for his help with metallography. This work is supported by the Strategic Research Center "REWIND - Knowledge based engineering for improved reliability of critical wind turbine components", Danish Research Council for Strategic Research, grant no. 10-093966.

8. References

[1] Murakami Y., Naka M., Iwamoto A. Long life bearings for automotive alternator applications. SAE Technical paper 950944 (1995) 1-14.

[2] Becker P.C. Microstructural changes around non-metallic inclusions caused by rolling-contact fatigue of ball bearing steel. Metals Technol 8(6) (1981) 234-243.

[3] Harris T.A., Kotzalas M.N. Rolling bearing analysis. 5th ed. CRC Press (2007) 295-299.

[4] Shibata M., Gotoh N., Oguma N., Mikami T. A new type of microstructural change due to rolling contact fatigue on bearings for the engine auxiliary devices. Proceedings international tribology conference (ITC) (1995) 1351.

[5] Tamada K., Tanaka H. Occurrence of brittle flaking on bearings used for automotive electrical instruments and auxiliary devices. Wear 199 (1996) 245-252.

[6] Konstantarakis C. Hydrogen degradation of high strength steel weldments. Thesis document, Massachusetts Institute of Technology 1993.

[7] Ichitani K., Kanno M. Visualization of hydrogen diffusion on steels by high sensitivity hydrogen microprint technique. Science and Technology of Advanced Materials 4 (2003) 545-551.

[8] Evans M.-H. White structure flaking(WSF) in wind turbine gearbox bearings:effects of butterflies and white etching cracks (WEC), Materials Science and Technology 28 (2012) 3-22.

[9] Harada H., Mikami T., Shibata M., Sokai D., Yamamoto A., Tsubakino H. Microstructural Changes and Crack Initiation with White Etching Area Formation under Rolling / Sliding Contact in Bearing Steel. ISIJ International, 45(12) (2005) 18971902.

[10] Luyckx J. WEC failure modes in roller bearings - From observation via analysis to understanding and a solution. VDI Berichte (2147)(2011)3142.

[11] Tallian T. E. Review of IrWEA associated damage modes Part 2. Stress: The International Journal on the Biology of Stress(2011) 17.

[12] Kino N., Otani K. The influence of hydrogen on rolling contact fatigue life and its improvement. JSAE Review 24 (2003) 289-294.

[13] Fujita S., Mitamura N., Murakami Y. Research of new factors affecting rolling contact fatigue. Proceedings of WTC 2005, Washington (2005) 63400

[14] Iso K., Yokouchi A., Takemura H. Research work for clarifying the mechanism of white structure flaking and extending the life of bearings. SAE Technical Paper Series 2005-01-1868 (2005) 1-11.

[15] Mitamura N., Hidaka H., Takaki S. Microstructural development in bearing steel during rolling contact fatigue. Material Science Forum, 539-543 (2007) 4255-4260.

[16] Evans M.-H., Richardson A.D., Wang L., Wood R.J.K. Effect of hydrogen on butterfly and white etching crack (WEC) formation under rolling contact fatigue (RCF). Wear 306 (2013) 226-241.

[17] Evans M.-H., Richardson A.D., Wang L., Wood R.J.K. Serial sectioning investigation of butterfly and white etching crack (WEC) formation in wind turbine gearbox bearings. Wear 302 (2013) 1573-1562.

[18] Evans M.-H., Wang L., Jones H., Wood R.J.K. Investigation by serial sectioning, focussed ion beam and 3-D crack modelling Tribology Int. 65 (2013) 146-160.

[19] Evans M.-H., Richardson A.D., Wang L., Wood R.J.K. Confirming subsurface initiation at non-metallic inclusions as one mechanism for white etching crack (WEC) formation. Tribology Int., 75 (2014) 87-97.

[20] Kotzalas M.N., Doll G.L. Tribological advancements for reliable wind turbine performance. Philosophical transactions of the Royal Society A 368 (2010) 4829-2850.

[21] Uyama H., Yamada H., Hidaka H., Mitamura N. The effects of hydrogen on microstructural change and surface originated flaking in rolling contact fatigue. Tribology Online 6 2 (2011) 123-132.

[22] Troiano A.R. The role of hydrogen and other interstitials in the mechanical behaviour of metals. Transactions of the ASM 52 (1960) 54-80.

[23] Beachem C.D. A new model for hydrogen assisted cracking (Hydrogen "Embrittlement"). Metallurgical Transactions 3 (1972) 437-451.

[24] Oriani R.A., Josephic P.H. Equilibrium aspects of hydrogen-induced cracking of steels. Acta Metal. 22 (1974) 1065-1074.

[25] Matsui H., Kimura H. The effect of hydrogen on the mechanical properties of high purity iron. I. Softening and hardening of high purity iron by hydrogen charging during tensile deformation. Materials Science and Engineering 40 (1979) 207-216.

[26] Hirth J.P. Effects of hydrogen on the properties of iron and steel. Metallurgical Transactions 11A (1980) 861-890

[27] Birnbaum H.K., Sofronis P. Hydrogen enhanced localized plasticity - A mechanism for hydrogen related fracture. Materials Science and Engineering A176 (1994) 191-202.

[28] Lynch S.P. Environmentally assisted cracking: Overview of evidence for an adsorption-induced localized slip process. Acta Metal. 36 10 (1998) 2639-2661.

[29] Nagumo M., Ishikawa T., Endoh T., Inoue Y. Amorphization associated with crack propogation in hydrogen-charged steel. Scripta Materialia 49 (2003) 837-842.

[30] Kang J.-H., Hosseinkhani B., Williams C.A., Moody M.P., Bagot P.A.J., Rivera-Diaz-del-Castillo. Solute redistribution in the nanocrystalline structure formed in bearing steels. Scripta Materialia 69 (2013) 630-633.

[31] Evans M.-H., Walker J.C., Ma C., Wang L., Wood R.J.K. A FIB/TEM study of butterfly crack formation and white etching area (WEA) microstructural changes under rolling contact fatigue in 100Cr6 bearing steel. Materials Science and Engineering A 570 (2013) 127-134.

[32] Fujita S., Matsuoka S., Murakami Y., Marquis G. Effect of hydrogen on mode II fatigue crack behaviour of tempered bearing steel and microstructural changes. International Journal of Fatigue 32 (2010) 943-951.

[33] Murakami Y., Kanezaki T., Mine Y., Matsuoka S. Hydrogen embrittlement mechanism in fatigue of austenitic stainless steels. Metallurgical and Materials Transactions A 39 (2008) 1327-1339.

[34] Nagumo M., Nakamura N., Takai K. Hydrogen thermal desorption relevant to delayed-fracture susceptibility of high-strength steels. Metallurgical and Materials Transactions A 32 (2001) 339-347.

[35] Nagumo M. Hydrogen related failure of steels - a new aspect. Materials Science and Technology 20 (2004) 940-950.

[36] Takai K., Shoda H., Suzuki H., Nagumo M. Lattice defects dominating hydrogen- related failure of metals. Acta Materialia 56 (2008) 5158-5167.

[37] Murakami Y., Matsunaga H. The effect of hydrogen on fatigue properties of steels used for fuel cell system. International Journal of Fatigue 28 (2006) 1509-1520.

[38] Gegner J. Tribological aspects of rolling bearing failures, in: C.H. Kuo (Ed.), Tribology - Lubricants and Lubrication, InTech (2011) 33-94.

[39] Gegner J., Nierlich W. Service loading analysis of wind turbine gearbox rolling bearings based on X-ray diffraction residual stress measurements. Materials Science Forum Vol. 768-769 (2014) 723-732.

[40] Gegner J., Nierlich W., Bruckner M. Possibilities and extension of XRD material response analysis in failure research for the advanced evaluation of the damage level of Hertzian loaded components. Mat.-wiss. u.. Werkstofftech 38 No.8 (2007).

[41] Kohara M., Kawamura T., Egami M. Study on mechanism of hydrigen generation from lubricants. Tribology Transactions 49 (2006) 53-60.

[42] NSK, Long life bearings for engine accessories, Motion & Control, NSK (2004) 1-10.

[43] Hiraoka K., Fujimatsu T., Tsunekage N., Yamamoto A. Generation process observation of micro-structural change in rolling contact fatigue by hydrogen charged specimens. Japanese Journal of Tribology 52 (2007) 673-683.

[44] Vegter R.H., Slycke J.T. The role of hydrogen on rolling contact fatigue response of rolling element bearings. Journal of ASTM International 7 (2009) 1-12.

[45] Hamada H., Matsubara Y. the influence of hydrogen on tension-compression and rolling contact fatigue properties in bearing steel. NTN Technical Review, NTN (2006) 54-61.

[46] Hiraoka K., Nagao M., Isomoto T. Study on flaking process in bearings by white etching area generation, Journal of ASTM International 3 (2006) 1-7.

[47] Endo T., Dong D., Imai Y., Yamamoto Y. Study in rolling contact fatigue in hydrogen atmosphere - improvement of rolling contact fatigue life by formation of surface film, in: D.Dowson, M.Priest, G.Dalmaz, A.Lubrecht (Eds.), Life Cycle Tribology, 31st Leeds-Lyon Tribology Symposium, Elsevier, Trinity and All Saints College, Leeds, UK (2004) 343-350.

[48] Imai Y., Endo T., Dong D., Yamamoto Y. Study on rolling contact fatigue in hydrogen environment at a contact pressure below basic static load capacity. Tribology Transactions 53 (2010) 764-770.

[49] West O.H.E. Failure analysis and thermochemical surface engineering of bearings in the wind turbine drivetrain. Ph.D. thesis, Dept. of Mechanical Engineering, Technical University of Denmark (2014).

[50] Sugino K., Miyamoto K., Nagumo M., Aoki K. Structural alteration of bearing steels under rolling contact fatigue. Trans. ISIJ 10 (1970) 98-111.

[51] Osterlund R., Vingsbo O. Phase changes in fatigue ball bearings. Metallurgical and Materials Transactions A 11A (1980) 701-707.

[52] O'Brien J.L., King A.H. Electron microscopy of stress-induced structural alterations near inclusions in bearing steels. Trans. J. Fluids Eng. 88(3) (1966) 568-571.

[53] West O.H.E., Diederichs A.M., Alimadadi H., Dahl K.V., Somers M.A.J. Application of complementary techniques for advanced characterization of white etching cracks. Pract. Metallogr. 50 (2013) 6 410-431.

[54] Grabulov A., Ziese U., Zandbergen H.W. TEM/SEM investigation of microstructural changes within the white etching area under rolling contact fatigue and 3-D crack reconstruction by focused ion beam. Scripta Materialia 57 (2007) 635-638.

[55] Lund T.B. Sub-surface initiated rolling contact fatigue - influence of non-metallic inclusions, processing history and operating conditions. J. ASTM Int., 7 (2012) 1-12.

[56] Evans M.-H. White structure flaking failure in bearings under rolling contact fatigue [Ph.D.thesis]. University of Southampton (2013).

[57] Grabulov A., Petrov R.., Zandbergen H.W. EBSD investigation of the crack initiation and TEM/FIB analyses of the microstructural changes around the cracks formed under rolling contact fatigue (RCF). Int. Journal of Fatigue 32 (2010) 576-583.

[58] Osterlund R., Vingsbo O., Vincent L., Guiraldeng P. Butterflies in fatigued ball bearings - formation mechanism and structure. Scandinavian Journal of Metallurgy 11 (1982) 23-32.

[59] Voskamp A. Microstructural changes during rolling contact fatigue. Ph.D. Thesis, TU Delft, Netherlands (1996).

[60] Hamrock B. J., Jacobson B.O. Elastohydrodynamic lubrication of rectangular contacts. Technical Paper - 2111, National Aeronautics and Space Administration, USA (1983).

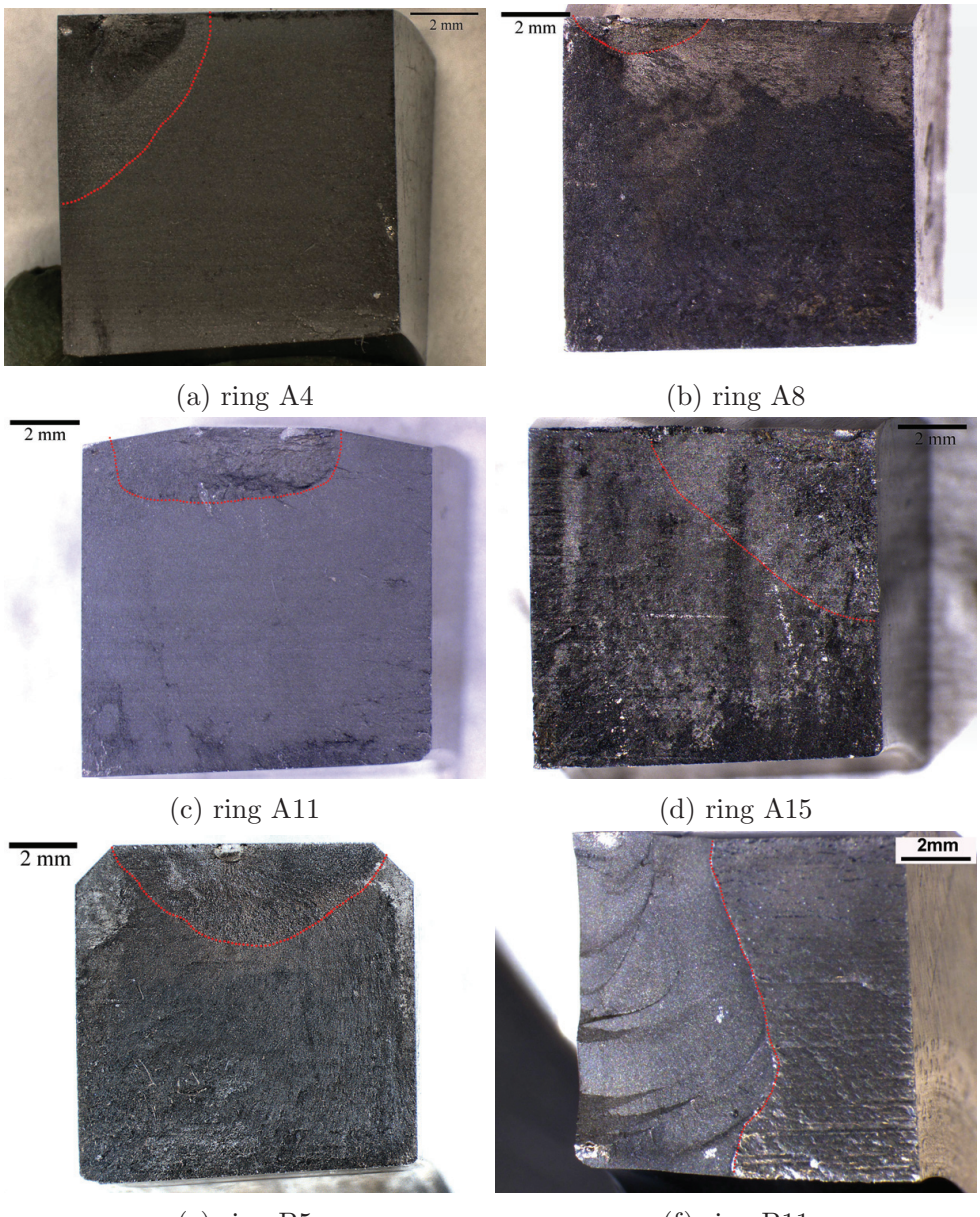

(a) ring A4 (b) ring A8

(c) ring A11 (d) ring A15

(e) ring B5 (f) ring B11

Figure 4: Fractography results of the fractured surfaces for the micro-indented rings at 350MPa Hoop stress and charged with 20 wt.% ammonium thiocyanate solution

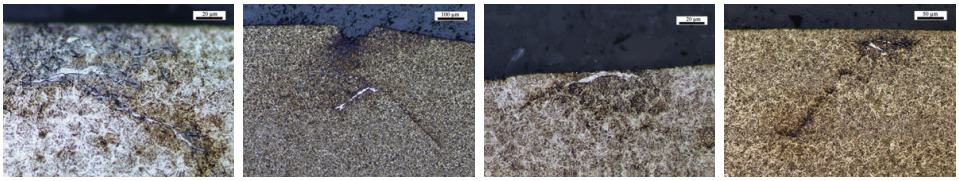

(a) ring A8 (b) ring A11 (c) ring B5 (d) ring B11

Figure 5: WEC found in the failed, poorly cleaned rings at 350MPa Hoop stress and charged with 20 wt.% ammonium thiocyanate solution

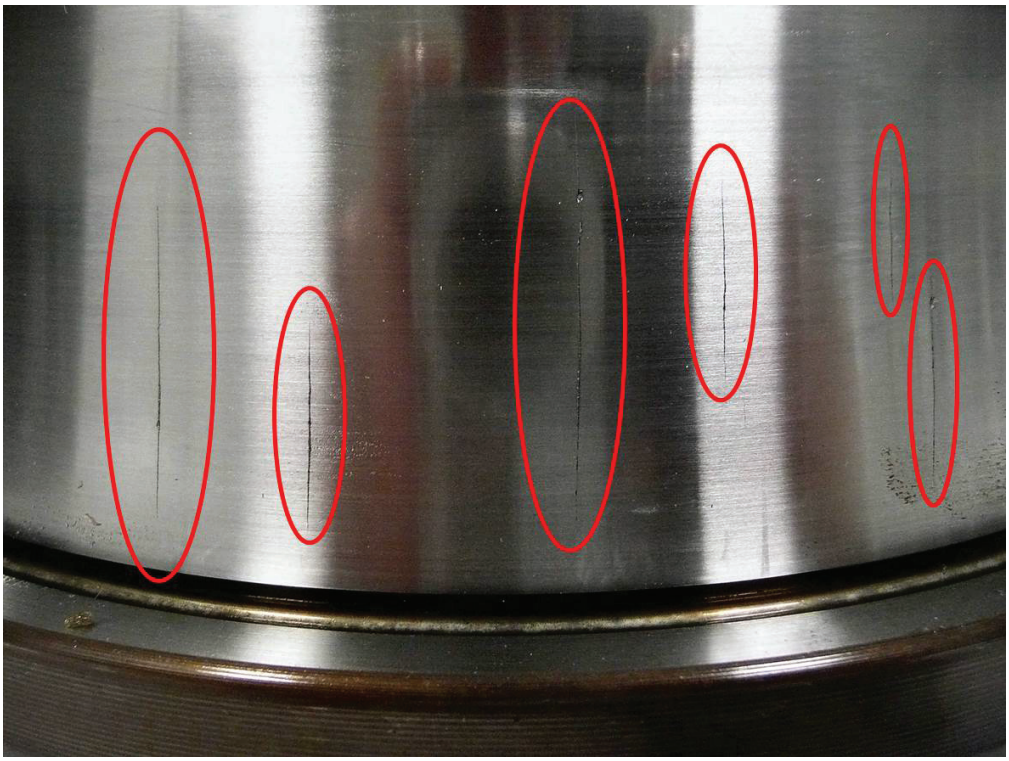

Figure 6: Axial cracks on the raceway of a inner ring of a martensitic 100Cr6 bearing from service [49]

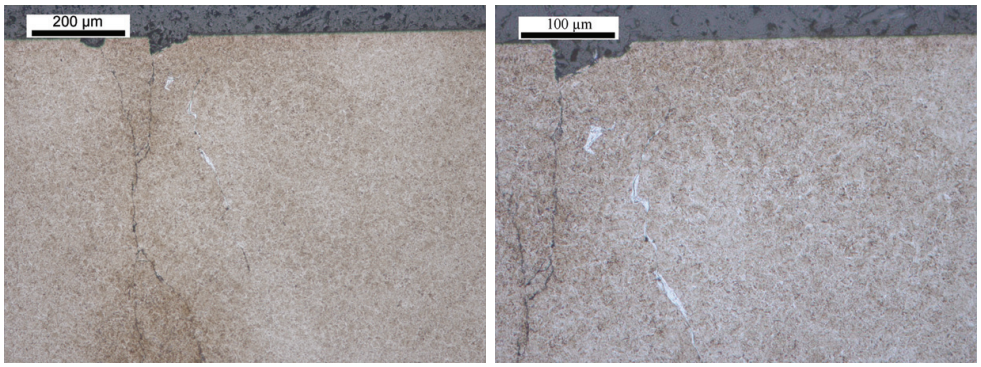

Figure 7: RLM pictures of nital etched axial cross-sections of the inner ring described in Fig. 6 showing WECs [49]

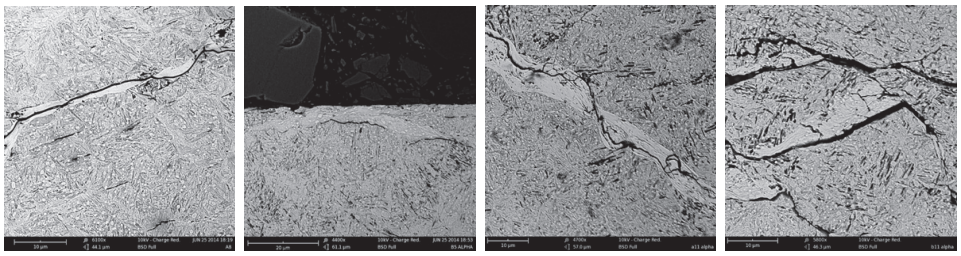

(a) ring A8 (b) ring B5 (c) ring A11 (d) ring B11

Figure 8: SEM of failed rings at 350MPa Hoop stress and charged with 20 wt.% ammonium thiocyanate solution

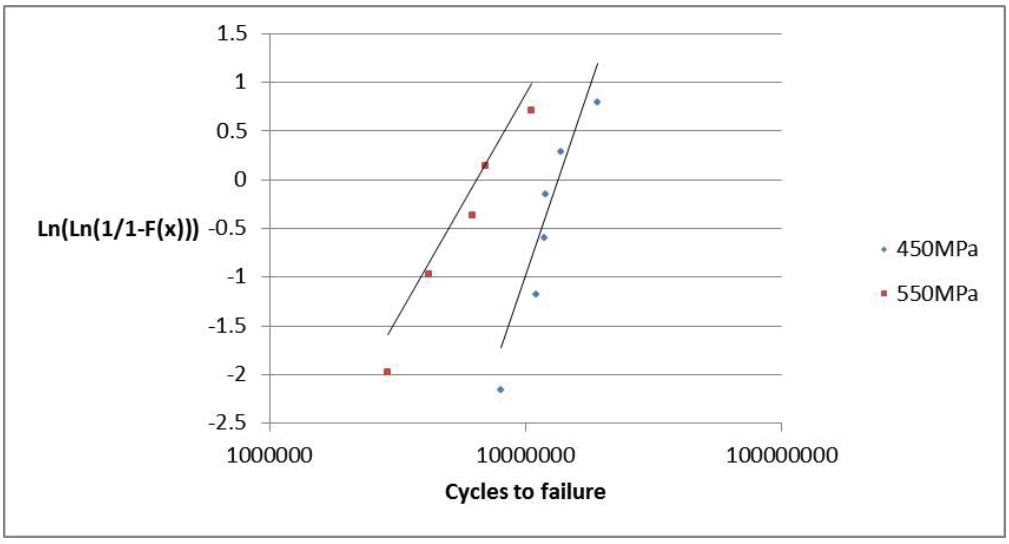

Figure 9: Weibull plots for the failed rings at 440MPa and 540MPa tensile Hoop stress respectively

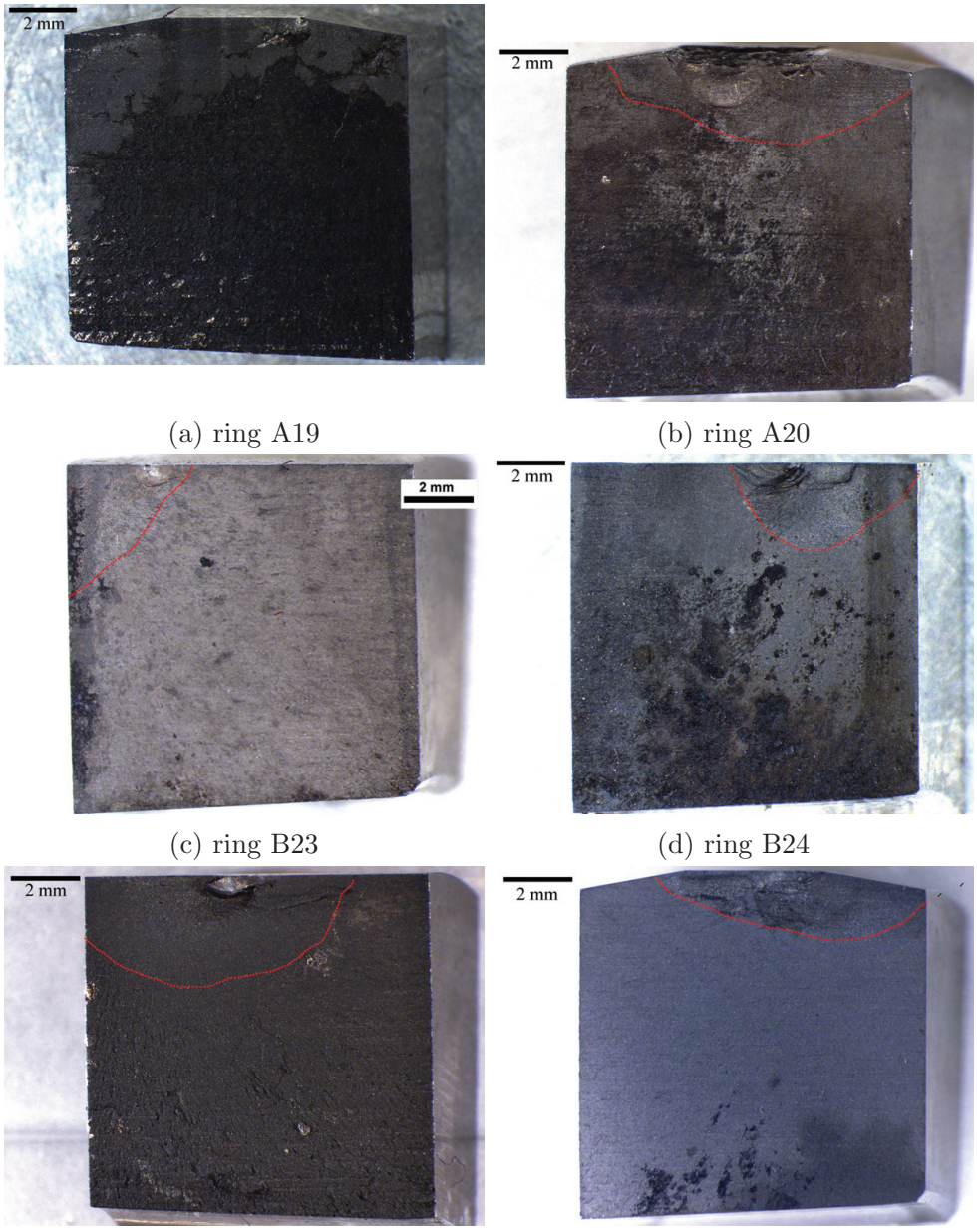

(a) ring A19 (b) ring A20

(c) ring B23 (d) ring B24

(e) ring B26 (f) ring A27

Figure 10: Fractography results of the fractured surfaces at 440MPa Hoop stress and charged with 12 wt.% ammonium thiocyanate solution

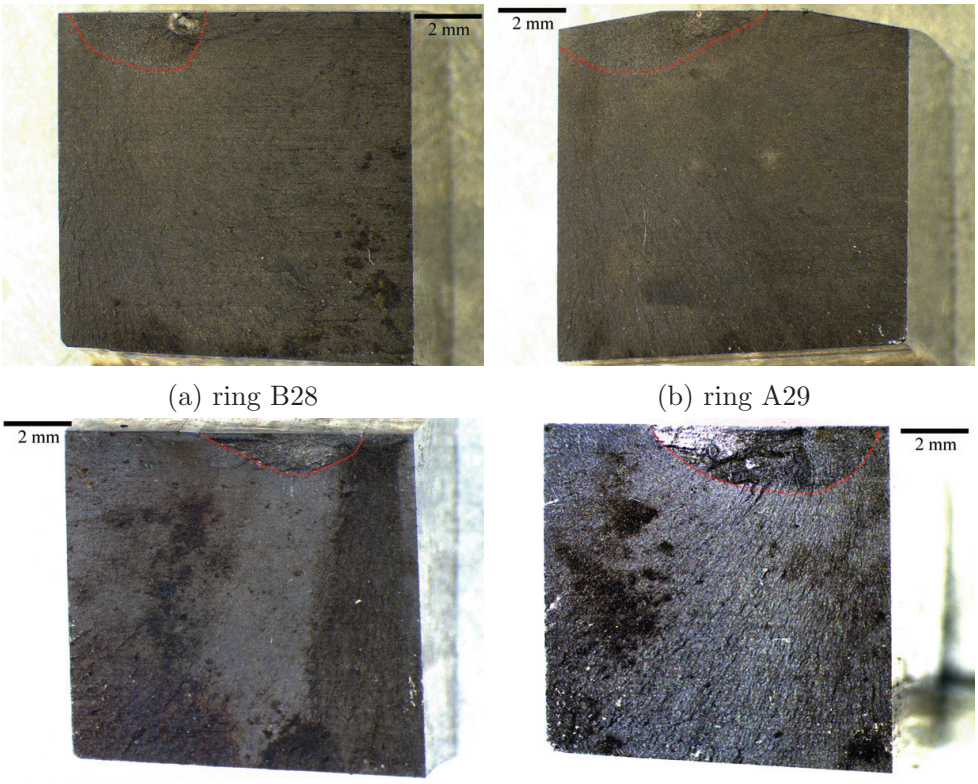

(a) ring B28 (b) ring A29

(c) ring B30 (d) ring B33

Figure 11: Fractography of the fractured surfaces at 540MPa Hoop stress and charged with 12 wt.% ammonium thiocyanate solution

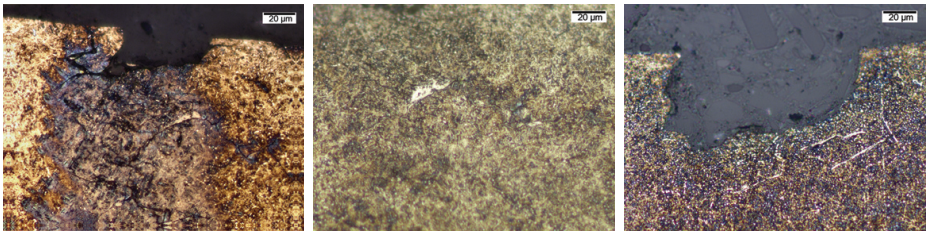

(a) ring A19 (b) ring A20 (c) ring B23

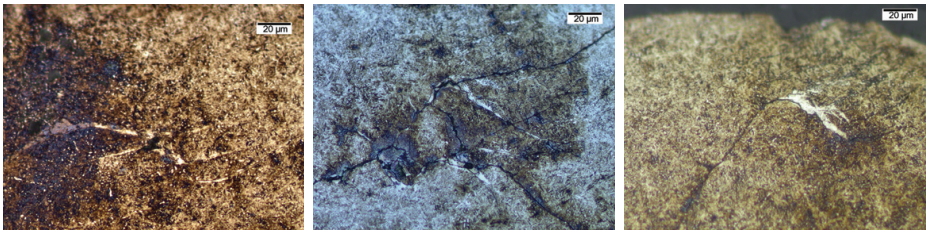

(d) ring B24 (e) ring B26 (f) ring A27

Figure 12: WEC on the fractured surfaces at 440MPa Hoop stress and charged with 12 wt.% ammonium thiocyanate solution

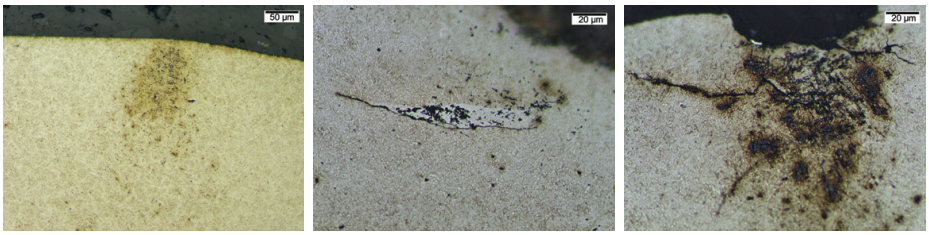

(a) ring A26 (b) ring B28 (c) ring A29

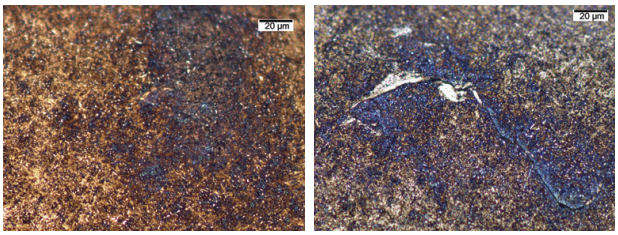

(d) ring B30 (e) ring B33

Figure 13: WEC on the fractured surfaces at 540MPa Hoop stress and charged with 12 wt.% ammonium thiocyanate solution

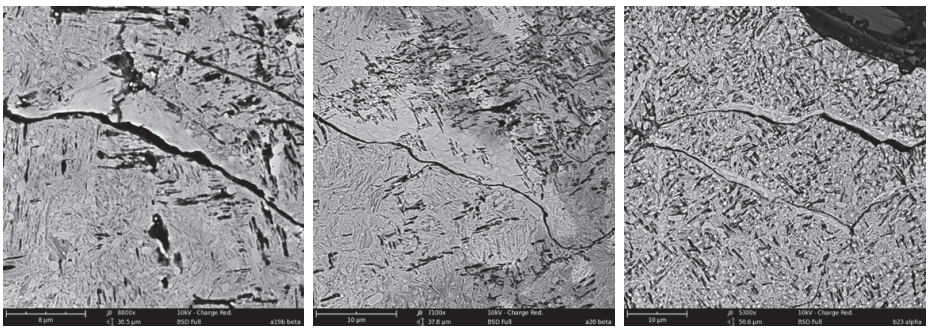

(a) ring A19 (b) ring A20 (c) ring B23

(d) ring B24 (e) ring B26 (f) ring A27

Figure 14: SEM of the WEA at 440MPa Hoop stress and charged with 12 wt.% ammonium thiocyanate solution

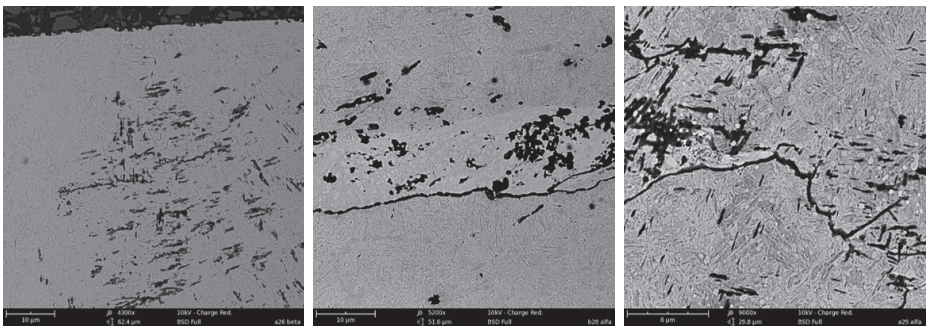

(a) ring A26 (b) ring B28 (c) ring A29

(d) ring B30 (e) ring B33

Figure 15: SEM of the fractured surfaces at 540MPa Hoop stress and charged with 12 wt.% ammonium thiocyanate solution

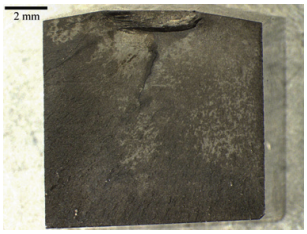

(a) Fractograph of ring A24

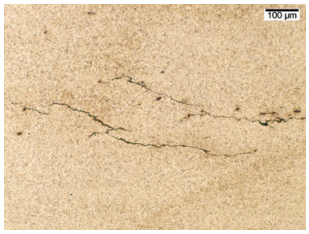

(b) RLM image of cracks on ring A24

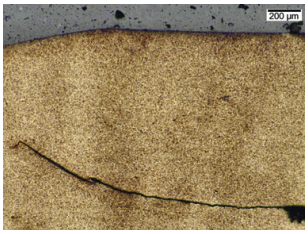

(c) RLM image of cracks on ring A24

(d) SEM image of crack on ring A24

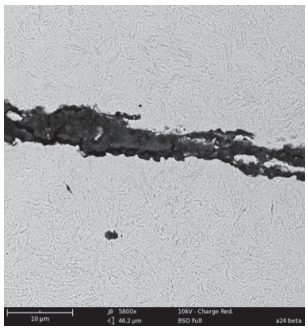

(e) SEM image of crack on ring A24

Figure 16: RLM and SEM images of ring A24 at 540MPa Hoop stress and no hydrogen charging

Publication D

Observations on the effect of grooved surfaces on the interfacial torque in highly loaded rolling and sliding tests.
Tribology International, 81, (2015),179-189.

Tribology International 81 (2015) 179–189

Contents lists available at ScienceDirect

Tribology International

journal homepage: www.elsevier.com/locate/triboint

Observations on the effects of grooved surfaces on the interfacial torque in highly loaded rolling and sliding tests

Shravan Janakiraman [a], Peder Klit [a,*], Niels S. Jensen [a], Jens Gronbaek [b]

[a] Department of Mechanical Engineering, Technical University of Denmark, Lyngby 2800, Denmark
[b] Strecon A/S, Stodagervej 5, Sonderborg 6400, Denmark

ARTICLE INFO

Article history:
Received 14 June 2014
Received in revised form
18 August 2014
Accepted 21 August 2014
Available online 1 September 2014

Keywords:
Transverse grooves
Traction
Rolling-sliding
Multigrid method

ABSTRACT

Some efforts have been undertaken to study the effects of grooved surfaces on the interfacial film thickness and torque between two contacting non-conformal surfaces under heavy loads. Transverse grooves of micrometer scale depth were engraved on polished, flat ring surfaces using established industrial methods like laser engraving and wire cutting. The grooved surfaces were then run against a polished flat surface at loads corresponding to high normal Hertzian pressures. Experiments were conducted to study the effects of the following parameters on the interfacial torque-groove depth, groove wavelength, load, inlet speed and slide-roll ratio. Experimental results were then justified, in certain cases, based on a multigrid model predicting the interfacial pressure and film thickness.

1. Introduction

Surface texturing has been used to study their effect on the tribological behaviour of sliding surfaces and journal bearings [1–3]. Ronen et al. [1] modelled the effect of micro pores on the friction losses in a reciprocating system and concluded that a friction reduction of at least 30% is possible with textured surfaces. Ramesh et al. [4] investigated lubricated sliding features having micrometer scale surface textures and reported a friction reduction of 80% for textured surfaces compared to non-textured surfaces at certain operating conditions. Surface textures increase the film thickness and reduce friction at certain operating conditions. Nanbu et al. [5] studied the effects of sliding and rolling speeds on the lubrication in concentrated conformal contacts. It was concluded that a faster moving textured surface compared to the non-textured surface, improved film thickness. Křupka et al. [6] investigated the effects of an array of micro-dents within a relatively lightly loaded (max. Hertzian pressure of 0.505 GPa) EHL contact. The authors concluded that the depth of micro-features is an important parameter in determining the tribological properties of an EHL contact. Wedeven and Cusano [7] studied the effects of parallel and perpendicular micro-grooves on the film thickness at pure rolling and sliding. It was concluded that under pure rolling conditions, both sets of grooves reduced the nominal film thickness when compared to the film thickness for smooth surfaces. Thus micro-textures are known to improve the film thickness at hydrodynamic loads. However there is no significant research conducted to study the tribological effect of these micro-textures at elastohydrodynamic (EHL) loads. The purpose of this study is to engrave micro-sized grooves on a ring surface using two well-established industrial methods and then study their tribological effects under EHL loading conditions. It is thought that if these grooves are found to be beneficial at high loads, a similar engraving process can be employed to engrave the surface of a rolling element in a rolling element bearing to improve their tribological performance. The parameter used to judge the tribological performance in this study is the interfacial torque in the conjunction.

There are multiple methods to texture grooves or dimples on metal and ceramic surfaces [8–18]. Etching grooves of sub-micrometer depth on a hardened steel ring is an extremely expensive process. This paper does not deal with sub-micrometer grooves because of this aspect. So micrometer scale grooves are engraved on the surface of a 100Cr6 bearing steel ring by two methods, laser engraving and wire cutting.

A multigrid method, using a combination of methods described by [19,20], is used to predict the film thickness and pressures generated in the lubricant, for a transverse groove of varying dimensions. These numerical method results are used to explain the experimental observations of the tests which study the effect of varying wavelength on the interfacial torque.

2. Test rig

The test rig consists primarily of two drive shafts and a hydraulic cylinder Fig. 1. One test ring is mounted on each shaft respectively. The two ring surfaces are brought into contact against each other by applying a normal load, using a hydraulic cylinder. Each ring has a conical bore, fitting on to a corresponding conical shape on the shaft.

* Corresponding author. Tel.: +45 45256267.
E-mail address: klit@mek.dtu.dk (P. Klit).

http://dx.doi.org/10.1016/j.triboint.2014.08.015
0301-679X/

Nomenclature

Symbol	Description
A	dimensionless amplitude of the groove
H_i	dimensionless film thickness at node i
H_o	dimensionless initial minimum film thickness
N	node number at the outlet
P_i	dimensionless pressure at node i
P_i^n	updated value of dimensionless pressure at node i
P_i^o	previous value of dimensionless pressure at node i
$P^{(k)}$	dimensionless pressure at grid level k
U	dimensionless speed parameter
W'	dimensionless groove wavelength
w	dimensionless load parameter
X_i	dimensionless x-coordinate at node i
X_d	dimensionless x-coordinate of the groove center
ΔX	dimensionless nodal distance
ω_{gs}	Gauss–Seidel under-relaxation factor
ω_{ja}	Jacobian under-relaxation factor
μ	dimensionless viscosity

The contact pressure between the ring and the shaft is controlled by the axial positioning of the ring on the shaft. Each drive shaft is capable of rotating at frequencies between 0 and 50 Hz. There is a provision for relative slip between the two rings when the two shafts rotate at different frequencies respectively. Hence it is possible to create conditions of rolling and sliding. Drive shaft 2 is connected to the Master motor and Drive shaft 1 is connected to the slave motor.

An inlet resting above the contact between the two rings allows for the lubricant to flow into the contact. The lubricant used is Mobil Delvac synthetic gear oil 75W-140, which is a fully synthetic, heavy duty drivetrain lubricant. This lubricant has a viscosity 182 cSt at 40 °C and 25 cSt at 100 °C [22]. The lubrication is not pressurised and the lubricant is allowed to fall freely, from a distance of approximately 2 cm, into the conjunction between the two rings. The inlet oil temperature is always maintained between 35 and 36 °C. A torque transducer is attached to drive shaft 2, so the interfacial torque generated between the two surfaces during slip can be measured.

Fig. 2 shows the schematic of the two rings in contact with each other. Each ring has an outer diameter of 70 mm. One ring has a chamfered surface with an axial width of 4 mm. The angle of chamfer is 10°. The opposing ring is unchamfered and has an axial width of 10 mm. The chamfered ring is then engraved by either laser engraving or wire cutting.

3. Experimental method

Two sets of tests are conducted. Test A studies the effect of varying groove depth on the interfacial torque. Test B studies the effect of varying wavelength on the interfacial torque.

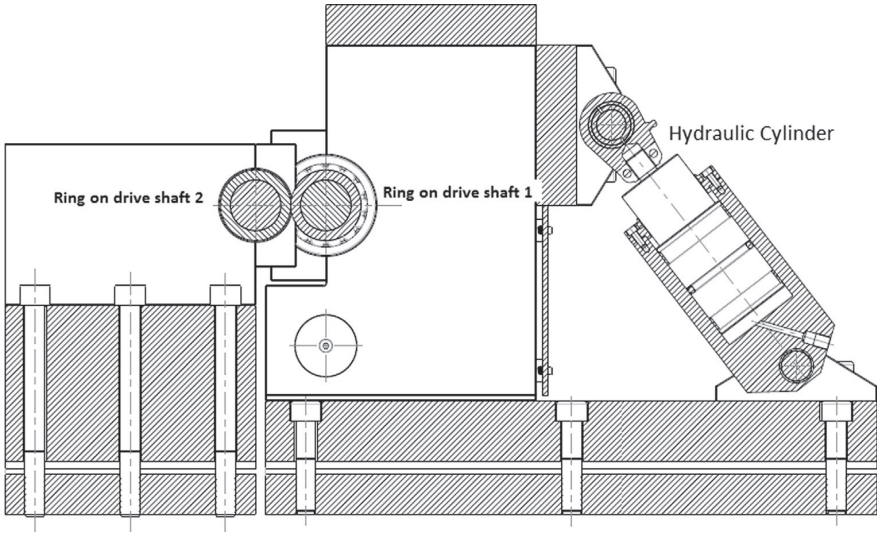

Fig. 1. Schematic of the rolling contact test rig.

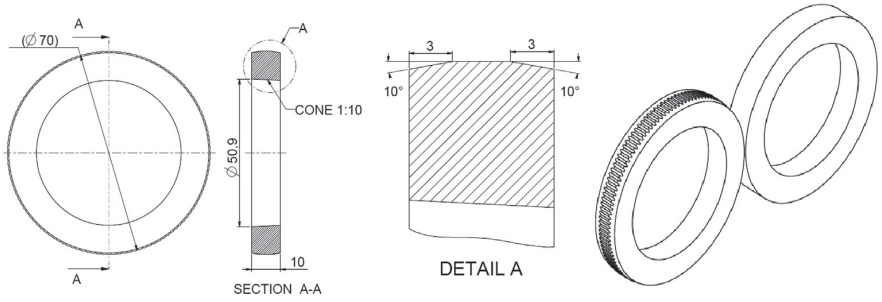

Fig. 2. Schematic of contact between grooved and smooth ring.

Each shaft, mounted with a ring, has two bearings supporting it. The spherical rolling bearings on each shaft experience a frictional moment due to the radial load and the rotational speed. The formula to calculate the frictional moment in bearings can be found in respectable bearing design books [23]. The total frictional moment experienced by each bearing is given by Eq. (1) where M_{load} is the load dependent frictional moment and $M_{velocity}$ is the velocity dependent frictional moment.

$$M_{total} = M_{load} + M_{velocity} \quad (1)$$

$$M_{load} = f_1 P_1 d_m (\text{N mm}) \quad (2)$$

where f_1 is an index based on the load and the bearing type; P_1 is the modified radial load (N); d_m is the pitch circle diameter of the bearing (mm)

$$M_{velocity} = 10^{-7}[f_0(\nu n)^{2/3} d_m^3](\text{N mm}) \quad (3)$$

where f_0 is an index based on the bearing type; ν is the operating viscosity of the lubricant (mm^2/s); n is the bearing speed (rpm); d_m is the pitch circle diameter of the bearing (mm).

The velocity dependent moment is about 4 times the magnitude of the load dependent moment at input parameter values used in this study. The total frictional moment in the bearings contributes to about 30% of the total torque value measured by the torque transducer. Hence the frictional moment at each combination of radial load and shaft speed is calculated and deducted from the measured value of the torque. This deducted value of torque is then plotted as the torque in the results of all the experiments conducted.

The two test schemes are described below.

4. Test A

Grooves of depth 13 μm are engraved on the surface of the chamfered ring by laser engraving. The ring is initially polished to a roughness R_a of 0.017 μm before engraving. The width of each groove is 210 μm and the width of the plateau between each groove equals the width of a single groove. A groove width of 210 μm is the smallest possible width that could be engraved using the laser method. The engraved ring with an original groove depth of 13 μm is then ground with a 1200 grit sand paper to reduce the depth of the grooves by 2 μm. Since the width of the plateau is small (210 μm) to conduct roughness tests with a stylus, the roughness is measured on a separate ring with no grooves. A non-engraved, polished ring with a surface roughness of 0.017 μm is ground with a 1200 sandpaper to reduce the diameter uniformly by 4 μm. The roughness, R_a, of this measured to be 0.10 μm. It is then assumed that the plateau regions of the engraved ring has a similar surface roughness.

The purpose of Test A is to study the effect of varying groove depth on the interfacial torque. The grooved ring with a groove depth of 11 μm is run against the opposing ring with no grooves. For an applied load the slide-roll ratio is varied. High slide-roll ratios (SRR) are not run because of metal on metal contact at high SRR. The values of the SRR are varied by changing the difference in the input frequencies of the 2 shafts. The master motor is run at a constant frequency of 20 Hz. The frequency of the slave motor is varied. The frequency of 20 Hz corresponds to an inlet speed of 8.792 m/s. The SRR is defined as

$$SRR = 2\left(\frac{f2 - f1}{f2 + f1}\right) \quad (4)$$

where $f1$ is the frequency of slave motor, and $f2$ is the frequency of master motor.

Each time the load is changed, the rings are run against each other for at least 30 min before results are recorded. This is done to allow the rings to run-in at the new load. After run-in, at a particular load, the SRR is controlled by appropriately varying the frequency of the slave motor. Once the SRR has been set, the test is run for 140 s and the values of torque are averaged over the final 120 s. Then the frequency of the slave motor is reset to correspond to a new value of SRR and the averaged torque values for the final 120 s of the new run are recorded. The steps are repeated until the necessary slide-roll ratios have been run. The values of torque are quite stable over the final 120 s. Dirty tests were conducted before the start of actual testing to observe the temperature increase of the lubricant with an increase in SRR. It was observed that the temperature of the lubricant at the inlet does not significantly increase (less than 2 °C after 3 h) at the highest run SRR compared to the lowest SRR, for the same load. There is however, no facility to check for the temperatures at the rolling contact conjunction with the current set-up.

When the 4 load conditions have been tested, the grooved ring is removed and the grooves are ground using a 1200 grit sandpaper. The groove depth is reduced by 2–9 μm. The grooved ring is then mounted on the shaft again and the tests are run again for the same values of load and SRR as mentioned above. At the conclusion of each set of tests, the grooved ring is dismounted and the groove depth was further decreased by 2 μm. In totality the tests are conducted on groove depths of 11 μm, 9 μm, 7 μm, 5 μm, 3 μm and 1 μm. The ring on the opposing shaft is kept unchanged through all the tests.

Pan and Hamrock [25] deduced a well established formula for calculating the central film thickness in EHL contacts between two smooth surfaces. Table 1 shows the analytical central film thickness for the input parameters used in Test A: inlet speed = 8.792 m/s, effective elastic modulus = 2.1×10^{11} Pa, effective radius = 1.75×10^{-2} m.

5. Test B

Grooves of depth 3 μm and varying wavelengths engraved on the surfaces of chamfered rings using a wire Electric Discharge Machining (EDM) process. The different wavelengths engraved measure 200 μm, 300 μm, 400 μm and 500 μm. The chamfered ring is mounted onto a fixture of a wire EDM machine. An ultra-high precision centring mechanism of the EDM machine is used to align the ring. A multilayer brass wire with a diameter of 70 μm is used to cut the surface of the bearing steel. The cut is made by the small sparks created when the wire contacts the ring. The heat from the sparks melts the metal forming a groove. To achieve a groove depth less than 10% the diameter of the wire, the cutting time is set so low so that the heat generated by the spark is just enough to engrave the required depth. The cutting time for a groove of depth 5 μm is approximately 1 s. The quantity of debris accumulated at the edge of the grooves, due to re-solidification of the melted metal, is removed by very light polishing. The plateaus between the grooves are then fine polished using a rotary polisher.

The grooved ring is run against a non-grooved ring. The non-grooved ring has a surface roughness, R_a value of 0.017 μm. The variables in Test B are load, inlet speed and groove wavelength. Tests are run where 2 of the 3 variables are kept constant, the third

Table 1
Theoretical minimum film thickness at various loads.

Max. Hertzian pressure (GPa)	Central film thickness (μm)
0.95	1.18
1.07	1.13
1.11	1.12
1.20	1.09

variable is varied and its effect on the interfacial torque is studied. High slide-roll ratios (SRR) are again not run because of metal on metal contact. The readings are taken exactly as described in Test A. The groove profile with a wavelength of 300 μm looks as shown in Fig. 3. The width of each groove is 50 μm. This is the smallest possible groove width that can be obtained using the wire EDM process for a cut groove depth of 3 μm. This groove width is chosen to be constant across all ring samples, so as to introduce no variation in this parameter while comparing the effect of other parameters.

6. Results and discussion of test A

Test A is conducted on a grooved ring–non-grooved ring pair. The grooves on the grooved ring are engraved using a laser engraving process. Fig. 4 shows the effect of varying groove depth on the interfacial torque between the two rings. The results show that the interfacial torque decreases as the groove depth is decreased for each load case. The Newtonian and non-Newtonian regions in each of these curves vary. The Newtonian region in each curve is that part of the curve where the torque values increase linearly with increasing SRR. The non-Newtonian region refers to that region of a curve, where there is no linear increase in the interfacial torque with SRR.

The results can be explained with the help of the finite difference multigridmodel describing the interfacial pressure, Fig. 5a, and film thickness values, Fig. 5b, for a non-conformal contact with a groove on one of the contact surfaces. The pressure and film thickness curves are calculated for pure rolling conditions. Jacobson and Hamrock [24] showed that there is no significant change in the EHL pressure curves at low SRR values. In this study, the authors assume that low SRR values refer to the Newtonian regions and the initial parts of the non-Newtonian region of the curves in Fig. 4. While the Newtonian region in each curve varies, the authors assume that an SRR of approximately 0.005 and lower corresponds to low SRR values.

The geometry of the problem is a cylindrical roller loaded against a half plane. EHL line contact conditions are implemented, so the geometry is planar. The multigrid method uses a 4 level W (1,2) cycle to solve the equations described in Appendix A. The number of nodes on the finest level is 1921 and the number of

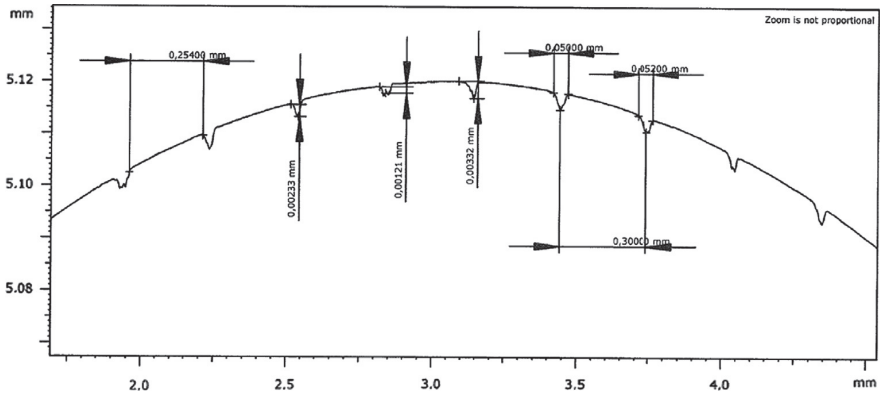

Fig. 3. Groove profiles with a wavelength of 0.3 mm engraved using the wire EDM method.

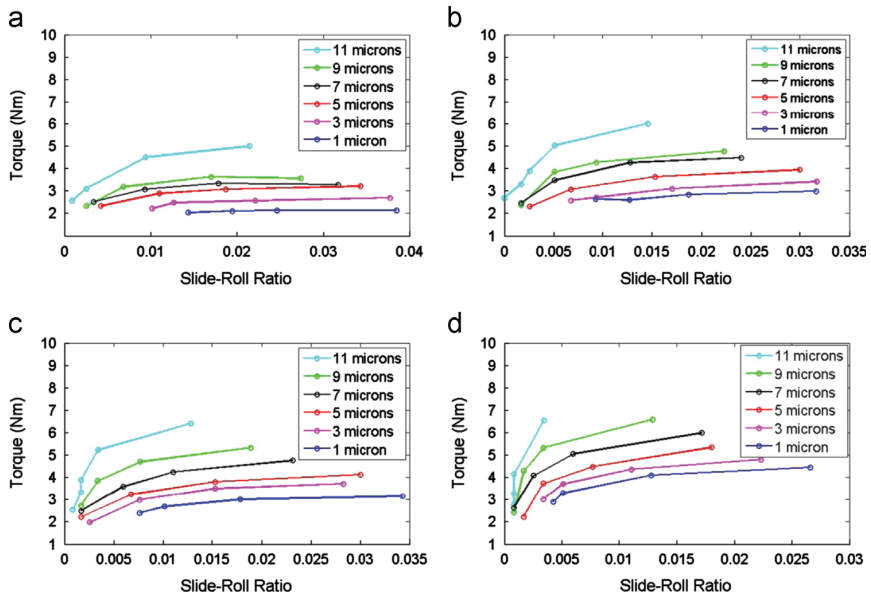

Fig. 4. Effect of varying groove depths on the interfacial torque on a grooved ring with an inlet speed of 8.792 m/s, at a given load and positive SRR. (a) Max. Hertzian pressure 0.95 GPa. (b) Max. Hertzian pressure 1.07 GPa. (c) Max. Hertzian pressure 1.11 GPa. (d) Max. Hertzian pressure 1.20 GPa.

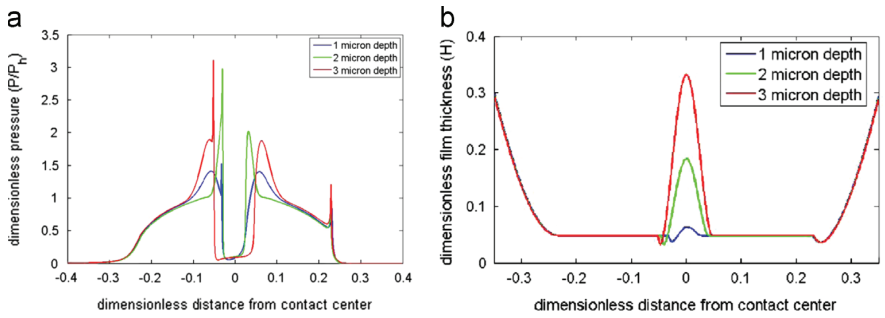

Fig. 5. Effect of varying groove depths on the pressures and film thickness values for a maximum Hertzian contact pressure of 1 GPa. The lubricant has a viscosity of 0.03 Pa s at zero pressure. The effective elastic modulus of the material is 2.1×10^{11} Pa. The inlet velocity of the lubricant is 1 m/s. The dimensionless load is $w = 1.42 \times 10^{-4}$. The wavelength of each groove is equal to the Hertzian contact half-width. (a) The pressure curves for varying groove depths. (b) The film thickness curves for varying groove depths.

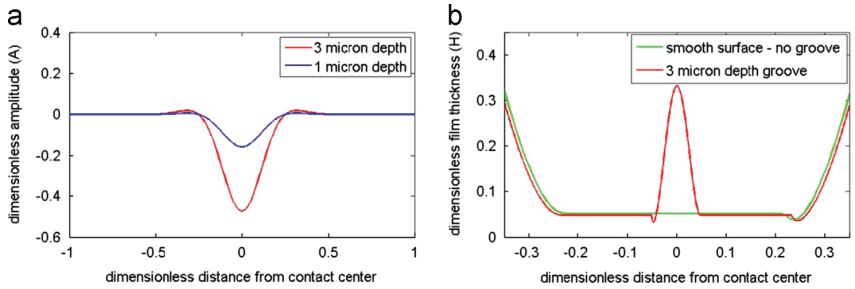

Fig. 6. Groove texture and film thickness. The lubricant has a viscosity of 0.03 Pa s at zero pressure. The effective elastic modulus of the material is 2.1×10^{11} Pa. The inlet velocity of the lubricant is 1 m/s. The dimensionless load is $w = 1.42 \times 10^{-4}$. The wavelength of each groove is equal to the Hertzian contact half-width. (a) Groove texture. (b) Film thickness curve for a smooth vs grooved surface.

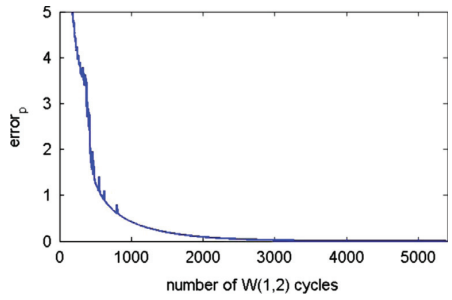

Fig. 7. Convergence curve for the groove of depth of 1 μm.

nodes on the coarsest level is 241. The system of equations is not time dependent.Fig. 5 shows the converged pressure and the film thickness curves for a contact between a smooth surface and a grooved surface. Fig. 7 shows the convergence curve for a groove of depth 1 μm. Convergence is reached when $error_p < 0.001$. $error_p$ has been defined in Appendix A.

The groove is depicted as shown in Fig. 6a. These curves can be used to explain the observable differences in the low SRR region of the curves in Fig. 4. Fig. 5b shows that the central film thickness remains the same across the conjunction, even with varying groove depth. At low SRRs, the central film thickness does not change significantly with groove depth as shown in Fig. 6b. Thus the central film thickness for EHL line contact between smooth surfaces with no grooves and a grooved surface is approximately the same but the pressure values and the pressure gradients are largely increased at the entrance and exit of these grooves 5a compared to a non-grooved surface. The reason for the increased torque values can be explained by the shear stress equations generated for the Newtonian and non-Newtonian regions in a EHL contact, described by [24]. In the Newtonian region, the shear stress at the top surface of two contacting surfaces is given by

$$\tau_a = \frac{h}{2}\frac{dp}{dx} + \frac{(u_a - u_b)\eta}{h} \tag{5}$$

where τ_a is the shear stress at the top surface; h is the film thickness; p is the pressure; dp/dx is the pressure gradient; u_a is the speed at the top surface; u_b is the speed at the bottom surface; η is the viscosity.

Eq. (5) shows that the shear stress increases with increasing pressure gradient in the lubricant. In the non-Newtonian zone where the shear stress at a surface is considered to be equal to a limiting shear strength by [24], the limiting shear strength is given by

$$\overline{\tau}_L = \overline{\tau}_0 + \gamma P \tag{6}$$

where $\overline{\tau}_L$ is the dimensionless limiting shear strength; $\overline{\tau}_0$ is the dimensionless initial shear strength; γ is the limiting shear strength proportionality constant; P is the dimensionless pressure.

Eq. (6) shows that an increased pressure causes an increase in the limiting shear strength of the material. Thus an increase in pressure around the edges of the groove and its gradient contribute to an increase in interfacial torque values.

Fig. 8 shows the surface of the 11 μm deep laser engraved after it has been tested under EHL conditions. The surface of the ring does not show excessive damage. There are a few marks seen on the plateaus but the grooves maintain their shape and there is no significant damage to the groove edges. There is a slight wear track observed close to the edges of the chamfer. The ring surface looks similar to Fig. 8 after tests have been conducted at lower groove depths.

7. Results and discussion of test B

Test B is conducted on a grooved and smooth (non-grooved) ring pair. Fig. 9 presents the results for the interfacial torque at varying wavelengths at a given load and high inlet speed. The tests are run for positive SRR values. The groove depth in each case is the same. The full Hertzian contact width for the loads applied is between 0.66 mm and 0.96 mm. The wavelengths are chosen to include cases of both multiple grooves in the contacts (wavelength of 0.2 mm and 0.3 mm) and cases where there are no more than 2 grooves in the contact (0.4 mm and 0.5 mm). The results suggest that there is no significant effect of the wavelength on the interfacial torque. The interfacial torque between two rings with no grooves is lower than the torque between a polished ring and a grooved ring. The rings without any grooves have a surface roughness R_a of 0.12 μm.

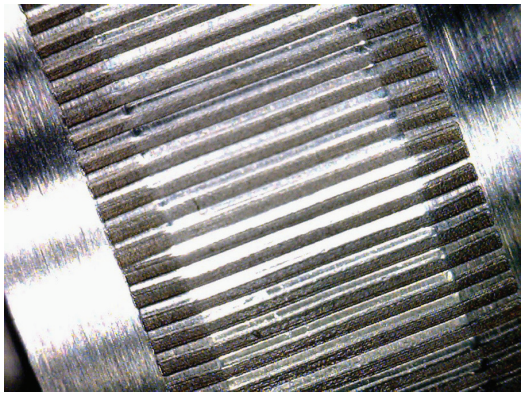

Fig. 8. The surface of the 11 μm micron deep grooved ring, after EHL testing at varying SRR and loads.

Table 2 shows the minimum number of grooves within the contact region at a certain load. Fig. 6b shows that there is no significant change in the Hertzian contact width on a ring with a groove. Based on those results it is assumed that the contact width for the tests performed with grooved rings is approximately the same as the width for two smooth surfaces. While this assumption may not be very accurate it still provides us with a comparative idea of the number of grooves within a contact region at different wavelengths and loads. Since there is no significant change in the torque values due to varying wavelength at a given load, it is interesting to note that the number of grooves within the contact make no apparent difference to the torque values. For example, at 1.2 GPa maximum Hertzian pressure, the 0.5 mm wavelength grooved ring has 1 or 2 grooves within the contact region while the 0.2 mm wavelength grooved ring has 4 grooves. So a significant increase in the number of grooves within the contact region makes no difference to the torque values at a given load and inlet speed.

Fig. 10 presents the results of the torque tests conducted on 4 rings with different wavelengths. The loads are varied for each ring and their effects studied. These results are along predictable lines as the increased loads lead to increased pressure and reduced film thickness values thus causing an increase in the interfacial torque. Differences in the torque values are observed in both the Newtonian and non-Newtonian parts of the curve.

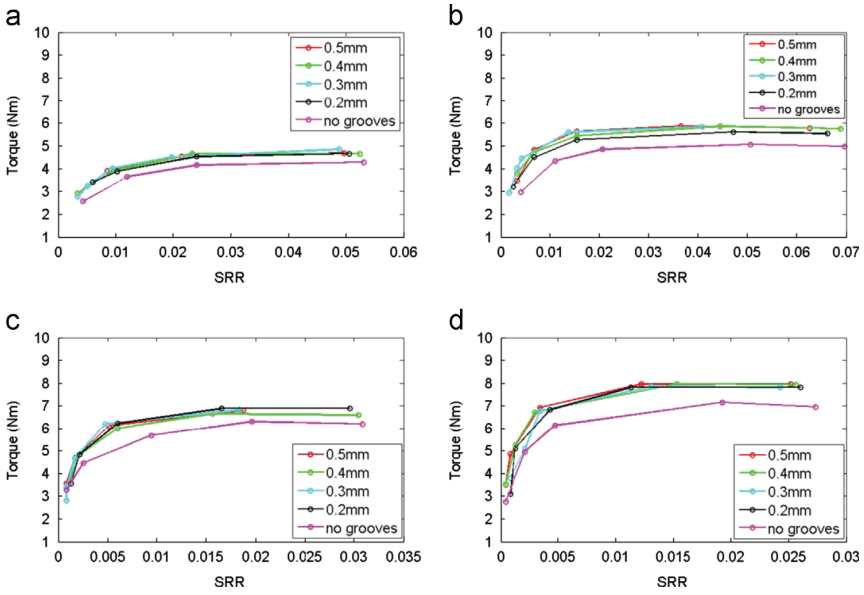

Fig. 9. Effect of varying wavelengths on the interfacial torque on a grooved ring with an inlet speed of 8.792 m/s, at a given load and positive SRR. (a) Max. Hertzian pressure 1.1 GPa. (b) Max. Hertzian pressure 1.2 GPa. (c) Max. Hertzian pressure 1.4 GPa. (d) Max. Hertzian pressure 1.45 GPa.

Table 2
Minimum number of grooves within a contact region.

Max. Hertzian pressure (GPa)	Corresponding contact width (mm)	Wavelength, 0.2 mm	Wavelength, 0.3 mm	Wavelength, 0.4 mm	Wavelength, 0.5 mm
1.1	0.66	3	2	1	1
1.2	0.79	4	2	2	1
1.4	0.93	4	3	2	2
1.45	0.96	4	3	2	2

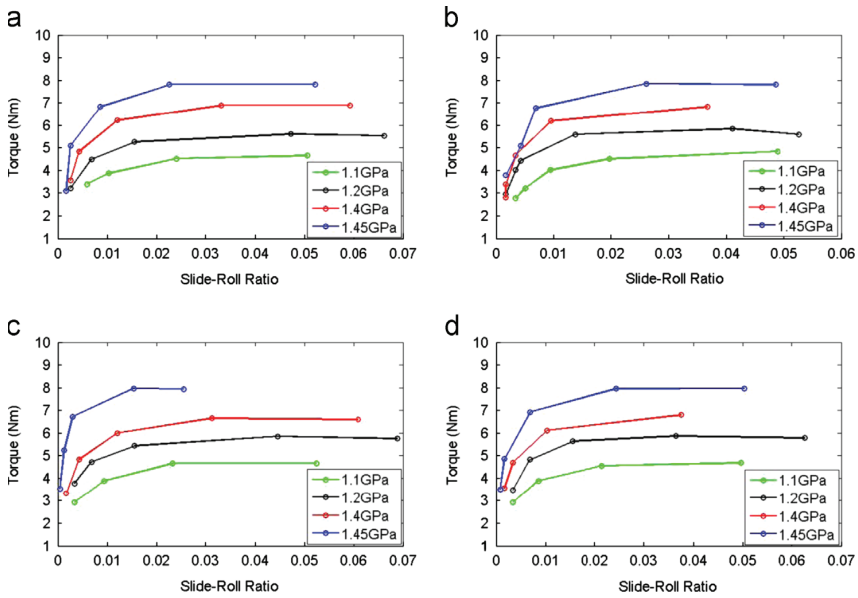

Fig. 10. Effect of varying loads on the interfacial torque on a grooved ring with an inlet speed of 8.792 m/s, at a given wavelength and positive SRR. (a) Wavelength of 0.2 mm. (b) Wavelength of 0.3 mm. (c) Wavelength of 0.4 mm. (d) Wavelength of 0.5 mm.

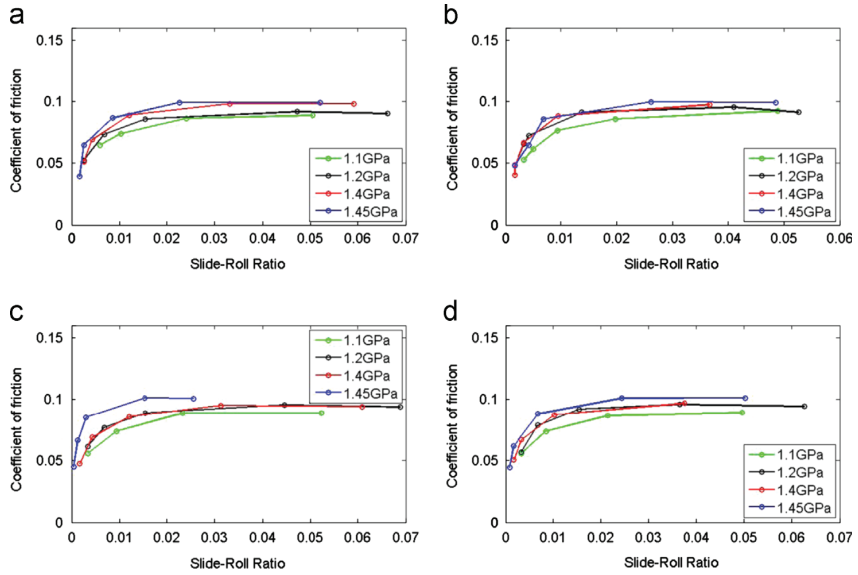

Fig. 11. Effect of varying loads on the coefficient of friction on a grooved ring with an inlet speed of 8.792 m/s, at a given wavelength and positive SRR. (a) Wavelength of 0.2 mm. (b) Wavelength of 0.3 mm. (c) Wavelength of 0.4 mm. (d) Wavelength of 0.5 mm.

Fig. 11 shows the coefficient of friction curves at varying loads for the four different wavelengths.

Tests corresponding to Fig. 12 are performed on a grooved ring with a wavelength of 0.25 mm. Four different inlet speeds are studied. The tests are performed to study if the interfacial torque values behave differently with varying loads at a given inlet speed. However Fig. 12 shows that the torque increases with increasing loads at all speeds.

Tests corresponding to Fig. 13 study the effect of the same parameters as in Fig. 12, but with a negative SRR. Ramesh et al. [4] suggested improved performance at negative SRR values and EHL conditions. The results of Fig. 13 show that the torque increases with load at all values of load and inlet speed. The curves at both positive and negative SRR show that the torque values increase with load. Comparing Figs. 12 and 13, there is no significant difference between the torque values at positive and negative SRR. The torque values are compared with SRR values up to 0.05. This is because higher SRR value tests are not conducted for positive SRRs.

Figs. 14 and 15 study the effects of varying inlet speed on the torque at different loads. Fig. 14 refers to the tests conducted with a negative SRR and Fig. 15 refers to the tests conducted with a positive SRR. Theoretically it should be expected that a relatively larger inlet speed increases the film thickness leading to lower

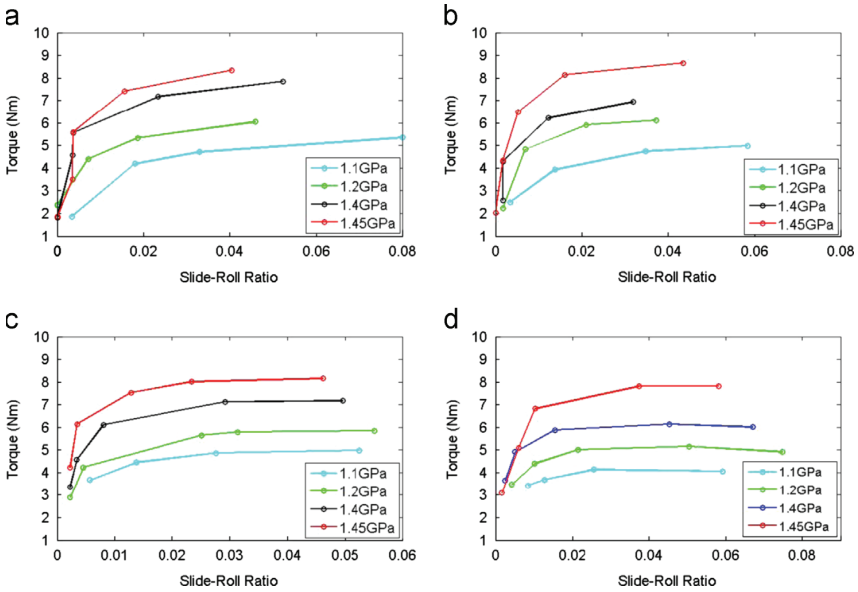

Fig. 12. Effect of varying loads on the interfacial torque on a grooved ring with wavelength 0.25 mm at a given inlet speed and positive SRR. (a) Inlet speed of 2.198 m/s. (b) Inlet speed of 4.396 m/s. (c) Inlet speed of 6.594 m/s. (d) Inlet speed of 8.792 m/s.

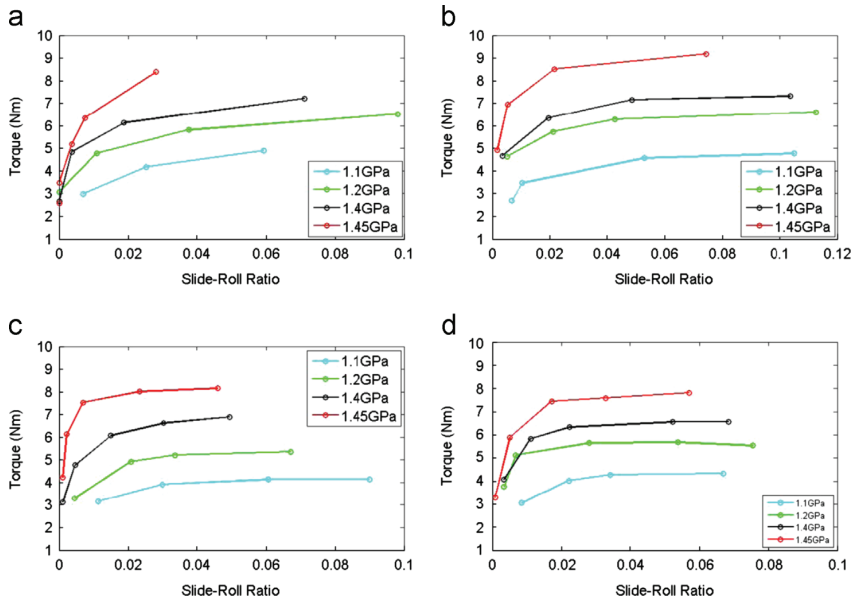

Fig. 13. Effect of varying loads on the interfacial torque on a grooved ring with wavelength 0.25 mm at a given inlet speed and negative SRR. (a) Inlet speed of 2.198 m/s. (b) Inlet speed of 4.396 m/s. (c) Inlet speed of 6.594 m/s. (d) Inlet speed of 8.792 m/s.

torque values at the same applied load. At a positive SRR, the curves corresponding to the highest inlet speed (8.792 m/s) behave as expected at all loads exhibiting the lowest torque. The curve corresponding to 6.594 m/s would be expected to have torque values in between the 8.792 m/s and the 2.198 and 4.396 m/s values. However this is not observed and the 2.198 m/s, 4.396 m/s and 6.594 m/s curves are bunched together showing very little difference between the torque measured at those values. The reason for this discrepancy is not understood.

At negative SRR values, Fig. 14, the highest inlet velocity curves do not lead to the lowest torque values at any load. In Fig. 14a and c, the torque does not appear to be dependent on the inlet speed. In Fig. 14b there is a difference between the torque values at 6.594 m/s and 4.396 m/s inlet speeds. In Fig. 14d there is a difference between the torque values of curves at 8.792 m/s and 4.396 m/s. This difference in torque values exists in both the Newtonian region of the curve (approx. between 0 and 0.02 SRR) and the non-Newtonian region of the curve (greater than 0.02 SRR). These results suggest that there are no tendencies in relation to the effect of inlet velocities on the torque at negative SRRs that can be observed. Since it is expected that a higher inlet speed will lead to a higher film thickness, it is interesting to note that at

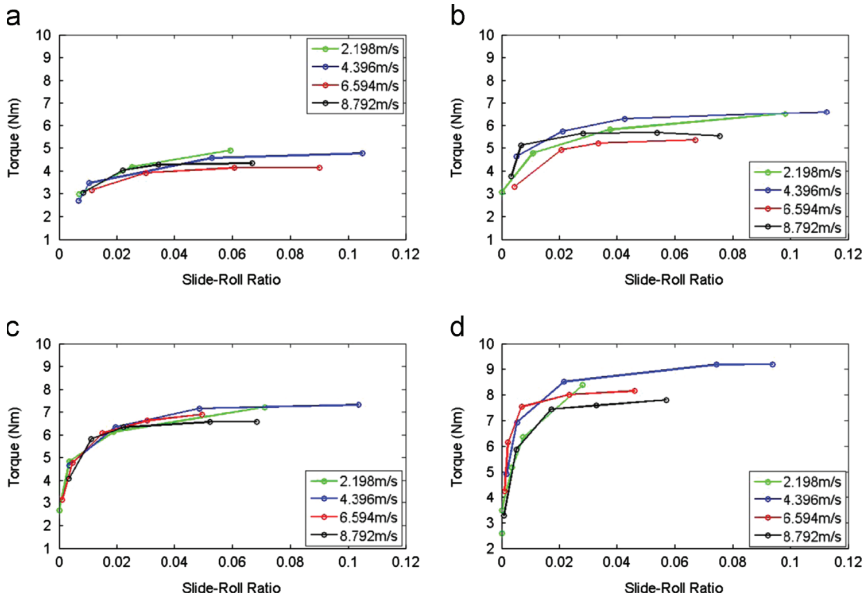

Fig. 14. Effect of varying inlet speeds on the interfacial torque on a grooved ring with wavelength 0.25 mm at a given load and negative SRR. (a) Max. Hertzian pressure 1.1 GPa. (b) Max. Hertzian pressure 1.2 GPa. (c) Max. Hertzian pressure 1.4 GPa. (d) Max. Hertzian pressure 1.45 GPa.

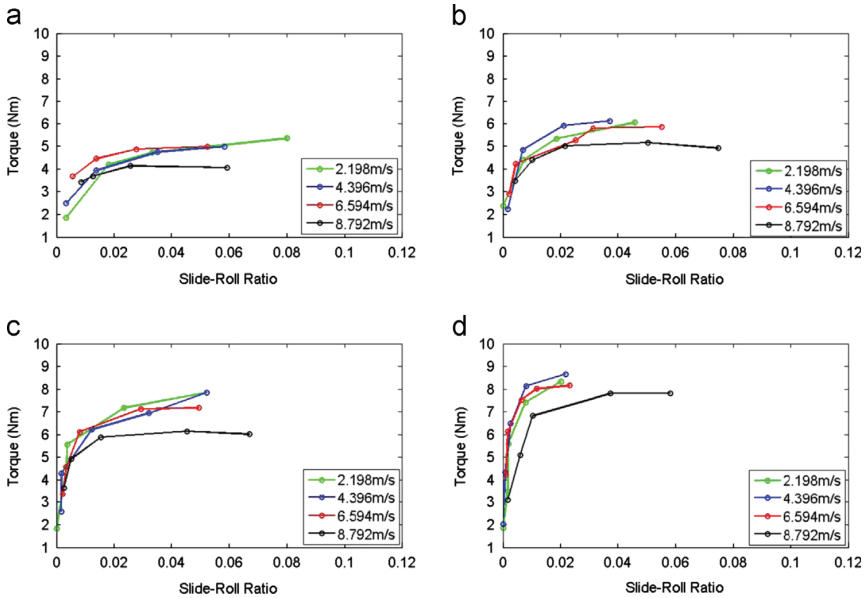

Fig. 15. Effect of varying inlet speeds on the interfacial torque on a grooved ring with wavelength 0.25 mm at a given load and positive SRR. (a) Max. Hertzian pressure 1.1 GPa. (b) Max. Hertzian pressure 1.2 GPa. (c) Max. Hertzian pressure 1.4 GPa. (d) Max. Hertzian pressure 1.45 GPa.

negative SRRs, the highest inlet velocity does not correspond to the lowest torque value at any of the four loads.

There is no significant difference between the torque values at positive and negative SRR for varying inlet speeds (Figs. 14 and 15), except for the values of torque at speeds corresponding to 6.594 m/s at a maximum Hertzian stress of 1.1 GPa. The torque values for a negative SRR are significantly lesser than their counterparts at a positive SRR. It has been well documented that grooves exhibit improved performance at optimum operating conditions. This results appears to indicate that the torque values at an inlet speed of 6.594 m/s, maximum Hertzian pressure of 1.1 GPa, wavelength of 0.25 mm and negative SRR shows a markedly improved performance than the torque values for a positive SRR and similar operating conditions.

8. Conclusions

Rolling contact tests have been performed on micrometer sized grooved rings to study if they exhibit a positive influence on the interfacial torque at EHL operating conditions. The following conclusions can be drawn based on the experimental observations.

(a) The interfacial torque decreases as the groove depth is decreased at a given load, inlet speed and wavelength. This is because the pressure at the entrance and exit of the groove decreases with decreasing groove depth. This decrease in pressure at the edges of the grooves leads to a decrease in the interfacial torque.
(b) At a given load, inlet speed and positive SRR, there is no significant change in the torque with varying wavelengths.
(c) At negative SRR values, the torque does not show a significant increase with decreasing inlet speeds. Decreasing inlet speeds are expected to decrease the film thickness due to rolling and hence increase the torque values. It appears as if the inlet speeds have no major influence on the interfacial torque values. The reason for this counter-intuitive result needs to be further examined. At positive SRR values, the curves corresponding to the highest inlet speed exhibit the lowest torque as expected. However at lower speed values, there appears to be no influence of the inlet speed on the torque.
(d) The grooves appear beneficial at certain optimum operating conditions. For example, at a load corresponding to a maximum Hertzian stress of 1.1 GPa, an inlet speed of 6.594 m/s and a wavelength of 0.25 mm, the torque at a negative SRR is significantly lower than the values at a positive SRR. However, such results are too uncommon to make a precise judgement on any positive tendency the grooves might have on the interfacial torque.

The tests have shown that it is possible to manufacture transverse, micrometer sized grooves all round the surface of hardened steel rings using well established methods like laser engraving and wire cutting. However, there is no significant evidence to prove that these grooves have a beneficial effect on the interfacial shear stress under rolling and sliding conditions and high loads.

Acknowledgements

The authors would like to thank Strecon A/S for providing them with the rings.

This work is supported by the Strategic Research Center "REWIND - Knowledge based engineering for improved reliability of critical wind turbine components", Danish Research Council for Strategic Research, Grant no. 10-093966.

Appendix A. Multigrid equations

The following equations to solve the multigrid problem for determining the pressures and film thickness in an EHL single-grooved contact have been formed by a combination of methods from three separate sources [19–21] who first used the following techniques to solve the smooth surface EHL problem. The study of multigrid methods to solve grooved EHL problems by [19] has been extremely influential in formulating the solver described in this section. Venner [19] can be referred to for the non-dimensionalization of the variables. Venner [19] treated the film thickness term as an independent variable and used the FAS RHS equations to solve the film thickness equations for smooth surface EHL problems. However Wang et al. [20] treated the nodal film thickness term as a variable dependent on the nodal pressure and no separate FAS RHS was used to solve the film thickness equation. Venner [19] used a combination of the Jacobi relaxation scheme in the high pressure regions and the Gauss–Seidel scheme in the low pressure regions to solve Reynolds equation. Wang et al. [20] used just the Gauss–Seidel relaxation scheme throughout the EHL conjunction.

The equations described in this section use a mixed relaxation scheme as described by [19], while treating the film thickness term as a variable dependent on the pressure term like [20].

The Reynolds equation for a line contact problem can be written as [19]

$$L_i=\frac{1}{(\Delta X)^2}[\epsilon_{(i-1)/2}P_{i-1}-(\epsilon_{(i-1)/2}+\epsilon_{(i-1)/2})P_i+\epsilon_{(i+1)/2}P_{i+1}]-\frac{1}{(\Delta X)}[H_i-H_{i-1}] \tag{A.1}$$

where $\epsilon=H^3/\mu\gamma$, $\gamma=3\pi^2U/(4w^2)$, $i=2\ldots N$.

The film thickness formed by a combination of [21,19] is given by

$$H_i=H_0+\frac{X_i^2}{2}+\sum_{i=1}^{n}D_{ij}P_j-R(X_i) \tag{A.2}$$

$$R(X_i)=A10^{-10((X_i-X_d)/W')^2}\cos\left(2\pi\frac{X_i-X_d}{W'}\right) \tag{A.3}$$

The FAS RHS vector is defined as

$$F^k=L^k\left(I_{k+1}^kP^{n(k+1)}\right)+I_{k+1}^k\left(F^{k+1}-L^{k+1}P^{n(k+1)}\right) \tag{A.4}$$

On the finest level $F^k=0$

$$I_{k+1}^k=\tfrac{1}{4}[1\ 2\ 1] \tag{A.5}$$

$$P^{o(k)}=I_{k+1}^kP^{n(k+1)} \tag{A.6}$$

$$P^{o(k+1)}=P^{n(k+1)}+I_k^{k+1}\left(P^{n(k)}-I_{k+1}^kP^{n(k+1)}\right) \tag{A.7}$$

The updated nodal pressure values are given by

$$P_i^n=P_i^o+\omega_{gs}\delta_i \tag{A.8}$$

$$\delta_i=\left(\frac{\partial L_i}{\partial P_i}\right)^{-1}r_i \tag{A.9}$$

in the Gauss–Seidel region and

$$P_i^n=P_i^o+\omega_{ja}(\delta_i-\delta_{(i-1)}) \tag{A.10}$$

$$\delta_i=\left(\frac{\partial L_i}{\partial P_i}-\frac{\partial L_i}{\partial P_{i-1}}\right)^{-1}r_i \tag{A.11}$$

in the Jacobi region

$$\left(\frac{\partial L_i}{\partial P_i}\right)=-\frac{1}{(\Delta X)^2}[(\epsilon_{(i-1)/2}+\epsilon_{(i+1)/2})]-\frac{1}{(\Delta X)}[D_{ii}-D_{(i-1)i}] \tag{A.12}$$

$$\frac{\partial L_i}{\partial P_i}-\frac{\partial L_i}{\partial P_{i-1}}=-\frac{1}{(\Delta X)^2}[(2\epsilon_{(i-1)/2}+\epsilon_{(i+1)/2})]-\frac{1}{(\Delta X)}[D_{ii}-D_{(i-1)i}-D_{i(i-1)}+D_{(i-1)(i-1)}] \tag{A.13}$$

The residual is given by

$$r_i=F_i^k-\frac{1}{(\Delta X)^2}[\epsilon_{(i-1)/2}P_{i-1}^n-(\epsilon_{(i-1)/2}+\epsilon_{(i-1)/2})P_i^o+\epsilon_{(i+1)/2}P_{i+1}^o]+\frac{1}{(\Delta X)}[H_i-H_{i-1}] \tag{A.14}$$

in the Gauss–Seidel region and

$$r_i=F_i^k-\frac{1}{(\Delta X)^2}[\epsilon_{(i-1)/2}P_{i-1}^o-(\epsilon_{(i-1)/2}+\epsilon_{(i-1)/2})P_i^o+\epsilon_{(i+1)/2}P_{i+1}^o]+\frac{1}{(\Delta X)}[H_i-H_{i-1}] \tag{A.15}$$

in the Jacobi region.

A node is said to be within the Gauss–Seidel region if

$$\frac{\epsilon_i}{(\Delta X)^2}>1 \tag{A.16}$$

If a node is not a Gauss–Seidel node, then it is a Jacobi node.

At the end of each W(1,2) cycle, H_0 is adjusted using an under-relaxation factor of 0.001. The flowchart for a W cycle is described in [20].

The force-balance equation on the finest level is

$$\frac{1}{2}\Delta X \sum_{j=1}^{N} (P_j + P_{j+1}) = \frac{\pi}{2} \tag{A.17}$$

The pressure convergence criterion is

$$err_p = \left(\frac{\sum_{j=1}^{N} |P_i^n - P_i^o|}{\sum_{j=1}^{N} P_i^o} \right) < 0.001 \tag{A.18}$$

Once this condition is reached the iterations are stopped.

References

[1] Ronen A, Etsion I, Kligerman Y. Friction-reducing surface-texturing in reciprocating automotive components. Tribol Trans 2001;44(3):359–66.
[2] Brizmer V, Kligerman Y, Etsion I. A laser surface textured parallel thrust bearing. Tribol Trans 2003;46:397–403.
[3] Kligerman Y, Etsion I, Shinkarenko A. Improving tribological performance of piston rings by partial surface texturing. J Tribol Trans ASME 2005;127:632–8.
[4] Ramesh A, Akram W, Mishra SP, Cannon AH, Polycarpou AA, King WP. Friction characteristics of microtextured surfaces under mixed and hydrodynamic lubrication. Tribol Int 2013:170–6.
[5] Nanbu T, Ren N, Yasuda Y, Zhu D, Wang J. Micro-textures in concentrated conformal-contact lubrication: effects of texture bottom shape and surface relative motion. Tribol Lett 2008;29:241–52.
[6] Křupka I, Hartl M. The effect of surface texturing on thin EHD lubrication films. Tribol Int 2007;40:1100–10.
[7] Wedeven LD, Cusano C. Elastohydrodynamic film thickness measurements of artificially produced surface dents and grooves. ASLE Trans 1978;21:41–52.
[8] Michelis K, Höhn BR, Kriel O. Influence of surface roughness on pressure distribution and film thickness in EHL contacts. Tribol Int 2006;39.
[9] Nakano M, Miyake K, Korenaga A, Sasaki S, Ando Y. Tribological properties of patterned NiFe-covered Si surfaces. Tribol Lett 2009;35:133–9.
[10] Siripuram RB, Stephens LS. Effects of deterministic asperity geometry on hydrodynamic lubrication. J Tribol Trans ASME 2004;126:527–34.
[11] Geiger M, Roth S, Becker W. Influence of laser-produced microstructures on the tribological behaviour of ceramics. Surf Coat Technol 1998;100:17–22.
[12] Wang XL, Kato K, Adachi K, Aizawa K. The effect of laser texturing of SiC surface on the critical load for transition of water lubrication mode from hydrodynamic to mixed. Tribol Int 2001;34:703–11.
[13] Pettersson U, Jacobson S. Friction and wear properties of micro textured DLC coated surfaces in boundary lubricated sliding. Tribol Lett 2004;17:553–9.
[14] Suh AY, Lee SC, Polycarpou AA. Adhesion and friction evaluation of textured slider surfaces in ultra-low flying head-disk interfaces. Tribol Lett 2004;17:739–49.
[15] Costa HL, Hutchings IM. Hydrodynamic lubrication of textured steel surfaces under reciprocating sliding conditions. Tribol Int 2007;40:1227–38.
[16] Dumitru G, Romano V, Weber HP, Haefke H, Gerbig Y, Pfliger E. Laser microstructuring of steel surfaces for tribological applications. Appl Phys A Mater Sci Process 2000;70:485–7.
[17] Andersson P, Koskinen J, Varjus S, Gerbig Y, Haefke H, Georgiou S, et al. Microlubrication effect by laser textured steel surfaces. Wear 2007;262:369–79.
[18] Nakano M, Korenaga A, Miyake K, Murakami T, Ando Y, et al. Applying micro-texture to cast iron surfaces to reduce the friction coefficient under lubricated conditions. Tribol Lett 2007;28:131–7.
[19] Venner CH. Multilevel solution of the EHL line and point contact problems. Enschede [Ph.D. thesis]. University of Twente, Netherlands, 1991.
[20] Wang J, Qu S, Yang P. Simplified multigrid technique for the numerical solution to the steady-state and transient EHL line contacts and the arbitrary entrainment EHL point contacts. Tribol Int 2001;34:191–202.
[21] Houpert LG, Hamrock BJ. Fast approach for calculating film thicknesses and pressures in elastohydrodynamically lubricated contacts at high loads. J Tribol 1986;108:411–20.
[22] Internet description of the lubricant properties on the Mobil website.
[23] Brandlein J, Eschmann P, Hasbargen L, Weigand K. Ball and roller bearings: theory design and application. 3rd ed. West Sussex, England: John Wiley and Sons; 1999 p. 221–3.
[24] Jacobson BO, Hamrock BJ. Non-Newtonian fluid model incorporated into elastohydrodynamic lubrication of rectangular contacts. NASA TM 83318; 1983.
[25] Pan P, Hamrock BJ. Simple formulae for performance parameters used in elastohydrodynamically lubricated line contacts. J Tribol 1989;111:246–51.

Bibliography

[1] Thomsen K. Modeling of dynamically loaded hydrodynamic bearings at low sommerfeld numbers. *Ph.D Thesis. Technical University of Denmark*, 2012.

[2] Hamrock B.J. *Fundamentals of Fluid Film Lubrication.* NASA RP - 1255, USA, 1991.

[3] Barus C. Isothermal, isopiestics, and isometrics relative to viscosity. *Am. J. Sci.*, 45, 1893.

[4] Roelands C.J.A. Correctional aspects of the viscosity-temperature-pressure relationship of lubricating oils. *Druk, V.R.B., Groningen, Netherlands*, 1966.

[5] Ertel A.M. Hydrodynamic lubrication based on new principles. *Akad. Nauk SSSR Prikadnaya Mathematica i Mekhanika, 3, 2, 41-52*, 1939.

[6] Grubin A.N. Fundamentals of the hydrodynamic theory of lubrication of heavily loaded cylindrical surfaces. *Central Scientific Research Institute for Technology and Mechanical Engineering, Book no. 30, Moscow, D.S.I.R. translations 115-166.*, 1949.

[7] Petrusevic A.I. Fundamental conclusions from the contact hydrodynamic theory of lubrication. *Izv. Akad. Nauk SSR (OTN), 3, 209-223*, 1951.

[8] Dowson D. and Higginson G.R. Elastohydrodunamic lubrication, the fundamentals of roller and gear lubrication. *Pergamon Press, Oxford, Great Britain.*, 1966.

[9] Hamrock B.J. and Dowson D. Isothermal elastohydrodynamic lubrication of point contacts, part I, theoretical formulation. *ASME J. of Lub. Tech., 98, 223-229*, 1976.

[10] Lubrecht A.A. Numerical solution of the ehl line and point contact problem using multigrid techniques. *Ph.D. thesis, University of Twente, Enschede, The Netherlands*, 1987.

[11] Venner C.H. and Lubrecht A.A. *Multilevel methods in lubrication.* Tribology series, 37, Elsevier, 2000.

[12] Wang J., Qu S., and Yang P. Simplified multigrid technique for the numerical solution to the steady-state and transient ehl line contacts and the arbitrary entrainment ehl point contacts. *Tribology International 34, 191-202*, 2001.

[13] Venner C.H. Multilevel solution of the ehl line and point contact problems. *Ph.D. thesis, University of Twente, Enschede, The Netherlands*, 1991.

[14] Houpert L. G. and Hamrock B. J. Fast approach for calculating film thicknesses and pressures in elastohydrodynamically lubricated contacts at high loads. *J. Tribology, vol. 108, no. 3*, 1986.

[15] Hamrock B. J. and Jacobson B. O. Elastohydrodynamic Lubrication of Line Contacts. *ASLE Trans., vol. 27, no. 4, pp 275-287*, 1984.

[16] Jolkin A. and Larsson R. Film thickness, pressure distribution and traction in sliding ehl conjunctions. *Lubrication at the frontier/D.Dowson et al.(Editors), Elsevier Science B.V.*, 1999.

[17] Jacobson B.O. and Hamrock B.J. Non-newtontian fluid model incorporated into elastohydrodynamic lubrication of rectangular contacts. *NASA TM 83318*, 1983.

[18] Evans M.-H. White structure flaking (wsf) in wind turbine gearbox bearings:effects of 'butterflies' and white etching cracks (wec). *Material Science and Technology 28, 3-22*, 2012.

[19] Tamada K. and Tanaka H. Occurence of brittle flaking on bearings used for automotive electrical instruments and auxiliary devices. *Wear 199, 245-252*, 1996.

[20] Kotzalas M.N and Doll G.L. Tribological advancements for reliable wind turbine performance. *Philosophical Transactions of the Royal Society A 368, 4829-4850*, 2010.

[21] Tamada K. and Nanbu T. Reproducing the brittle flaking of bearings by acceleration-deceleration test condition. *Proc. of The Society of Materials Science, Japan Meeting, Tokyo, 121-122*, 1994.

[22] Ciruna J.A. and Szieleit H.J. The effect of hydrogen on the rolling contact fatigue life of aisi 52100 and 440c steel balls. *Wear, 24, 107-118*, 1973.

[23] Ray D., Vincent L., Coquillet B., and Guirandenq P. Hydrogen embrittlement of a stainless ball bearing steel. *Wear, 65, 103-111*, 1980.

[24] Mizuhara K., Taki T., and Yamanaka K. Anomalous cracking of bearing balls under a liquid-butane environment. *Tribology International, 26, 2, 135-142*, 1993.

[25] Newlands C., Olver A., and Brandon N. Gaseous evolution of hydrogen from hydrocarbon oil and grease lubricated contacts. *Tribology and Interface Engineering Series, 41, 719-726*, 2003.

[26] Imran T., Jacobson B., and Shariff A. Quantifying diffused hydrogen in aisi-52100 bearing steel and silver steel under tribo-mechanical action: pure-rotating bending, sliding-rotating bending, rolling-rotating bending and uni-axial tensile loading. *Wear, 261, 86-95*, 2006.

[27] Kohara M., Kawamura T., and Egami M. Study on mechanism of hydrogen generation from lubricants. *Tribology Transactions 49, 53-60*, 2006.

[28] Kino N. and Otani K. The influence of hydrogen on rolling contact fatigue life and it's improvement. *JSAE Review, 24, 289-294*, 2003.

[29] Fujita S., Matsuoka S., Murakami Y., and Marquis G. Effect of hydrogen on mode ii fatigue crack behavior of tempered bearing steel and microstructural changes. *International Journal of Fatigue 32, 943-951*, 2010.

[30] Iso K., Yokouchi A., and Takemura H. Research work for clarifying the mechanism of white structure flaking and extending the life of bearings. *SAE Technical Paper Series 2005-01-1868, 1-11*, 2005.

[31] Cwiek J. Hydrogen degradation of high strength steels. *J. Achiev. Mater. Manuf. Eng., 37, 193-212*, 2009.

[32] Nagumo M., Takai K., and Okuda N. Nature of hydrogen trapping sites in steels induced by plastic deformation. *J. Alloys Compd, 293-295, 310-316*, 1999.

[33] Beachem C.D. A new model for hydrogen-assisted cracking (hydrogen 'embrittlement'). *Metall. Trans. B, 3B, (2), 437-451*, 1972.

[34] Otsuka T., Hanada H., Nakashima H., Sakamoto K., Hayakawa M., Hashizume K., and Sugisaki M. Observation of hydrogen distribution around non-metallic inclusions in steels with tritium microautoradiography. *Fusion Sci. Technol., 48 (1), 708-711*, 2005.

[35] Matsubara Y. and Hamada H. A novel method to evaluate the influence of hydrogen on the fatigue properties of high strength steels. *J. ASTM Int., 3 (2), 1-14*, 2006.

[36] Evans M.-H. White structure flaking (wsf) in wind turbine gerabox bearings: effects of 'butterflies' and white etching cracks (wecs). *Materials Science and Technology, vol. 28, No. 1*, 2012.

[37] Vegter R.H. and Slycke J.T. The role of hydrogen on rolling contact fatigue response of rolling element bearings. *Journal of ASTM International, Vol. 7, No. 2*, 2010.

[38] Becquart C.S., Domain C., and Foct J. Ab initio calculations of some atomic and point defect interactions involving c and n in fe. *Philos. Mag., Vol. 85, No. 4-7, 533-540*, 2005.

[39] Forst C.J., Slycke J., van Vliet K.J., and Yip S. Point defect concentrations in metastable fe-c alloys. *Phys. Rev. Lett., Vol. 96*, 2006.

[40] Gavriljuk V.G, Bugaev V.N., Petrov, Yu N., Tarasenko A.V., and Yanchitski B.Z. Hydrogen-induced equilibrium vacancies in fcc iron-base alloys. *Scr. Mater., Vol. 34, No. 6, 903-907*, 1997.

[41] McLellan R.B. and Xu Z.R. Hydrogen-induced vacancies in the iron lattice. *Scr. Mater., Vol. 36, No. 10, 1201-1205*, 1996.

[42] Slycke J. On the nature of the rolling contact fatigue damage mechanism. *unpublished*, 0000.

[43] Murakami Y. and Takahashi K. Torsional fatigue of a medium carbon steel containing an initial small surface crack introduced by tension-compression fatigue: crack branching, non-propagating and fatigue limit. *Fatigue Fract Eng Mater Struct, 21(2), 1473-1484*, 1998.

[44] Takahashi K. and Murakami Y. Torsional fatigue of specimens containing an initial small crack introduced by tension-compression fatigue: effects of shear mean stress and tensile or compressive mean stress. *Trans Jpn Soc. Mech Eng, A68(668), 645-652*, 2002.

[45] Zhang A. and Akid R. Mechanisms and fatigue performance of two steels in cyclic torsion with axial static/compression. *Fatigue Fract Eng Mater Struct, 20(4), 547-557*, 1997.

[46] Uyama H., Mine Y., Murakami Y., Nakashima M., and Morishige K. Effects of hydrogen charge on microscopic fatigue behavior of annealed carbon steels. *Fatigue Fract Eng Mater Struct, 29(12), 1061-1074*, 2006.

[47] Murakami Y. and Matsunaga H. The effect of hydrogen on the fatigue properties of steels used for fuel cell system. *Int J Fatigue, 28, 1509-1520*, 2006.

[48] Uyama H., Yamada H., Hidaka H., and Mitamura N. The effects of hydrogen on microstructural change and surface originated flaking in rolling contact fatigue. *Tribology Online, 6, 2, 123-132*, 2011.

[49] Grabulov A., Petrov R., and Zandbergen H.W. EBSD investigation of the crack initiation and tem/fib analyses of the microstructural changes around the cracks formed under rolling contact fatigue (rcf). *Int. J. Fatigue, 32(3), 576-583*, 2010.

[50] Sugino K., Miyamoto K., Nagumo M., and Aoki K. Structural alterations of bearing steels under rolling contact fatigue. *ISIJ Int., 10, 98-111*, 1970.

[51] Harada H., Mikami T., Shibata M., Sokai D., Yamamoto A., and Tsubakino H. Microstructural changes and crack intiation with white etching area formation under rolling/sliding contact in bearing steel. *ISIJ Int., 45(12), 1897-1902*, 2005.

[52] Osterlund R., Vingsbo O., Vincent L., and Guiraldenq P. Butterflies in fatigued ball bearings - formation mechanism and structure. *Scand. J. Metall., 11, 23-32*, 1982.

[53] Lund T.B. Subsurface initiated rolling contact fatigue - influence of nonmetallic inclusions, processing conditions and operating conditions. *J. ASTM Int., 7(5), 1-12*, 2010.

[54] Becker P.C. Microstructural changes around non-metallic inclusions caused by rolling contact fatigue of ball-bearing steels. *Met. Technol., 8, 234-243*, 1981.

[55] Hiraoka K., Nagao M., and Isomoto T. Study on flaking process in bearings by white etching area generation. *J. ASTM Int., 3(5), 1-7*, 2006.

[56] Kligerman Y., Etsion I., and Shinkarenko A. Improving tribological performance of piston rings by partial surface texturing. *ASME J. Tribol., 127, 632-638*, 2005.

[57] Etsion I., Kligerman Y., and Halperin G. Analytical and experimental investigation of laser-textured mechanical seal faces. *Tribology Transactions, 42, 511-6*, 1999.

[58] Erdemir A. Review of engineered tribological interfaces for improved boundary lubrication. *Tribology International, 38, 249-256*, 2005.

[59] Krupka I. and Hartl M. The effect of surface teturing on thin ehd lubrication films. *Tribology International 40, 1100-1110*, 2007.

[60] Mourier L., Mazuyer D., Lubrecht A.A., and Donnet C. Transient increase of film thickness in micro-textured ehl contacts. *Tribology International 39, 1745-1756*, 2006.

[61] Wedeven L.D. and Cusano C. Elastohydrodynamic film thickness measurements of artifically produced surface dents and grooves. *ASLE Trans., 22, 369-381*, 1979.

DTU Mechanical Engineering
Section of Solid Mechanics
Technical University of Denmark

Nils Koppels Allé, Bld. 404
DK- 2800 Kgs. Lyngby
Denmark
Phone (+45) 4525 4250
Fax (+45) 4593 1475
www.mek.dtu.dk
ISBN: 978-87-7475-409-1

DCAMM
Danish Center for Applied Mathematics and Mechanics

Nils Koppels Allé, Bld. 404
DK-2800 Kgs. Lyngby
Denmark
Phone (+45) 4525 4250
Fax (+45) 4593 1475
www.dcamm.dk
ISSN: 0903-1685